NANYANG TECHNOLOGICAL UNIVERSITY

DEVELOPMENT AND CHARACTERIZATION OF SHAPE MEMORY CERAMICS AT MICRO/NANOSCALE

ZENG XIAOMEI

SCHOOL OF MATERIALS SCIENCE AND ENGINEERING

2017

DEVELOPMENT AND CHARACTERIZATION OF SHAPE MEMORY CERAMICS AT MICRO/NANOSCALE

ZENG XIAOMEI

SCHOOL OF MATERIALS SCIENCE AND ENGINEERING

A thesis submitted to the Nanyang Technological University
in partial fulfilment of the requirement for the degree of
Doctor of Philosophy

2017

Statement of Originality

I hereby certify that the work embodied in this thesis is the result of original research and has not been submitted for a higher degree to any other University or Institution.

20/07/2016	ZENG XIAOMEI
. . . . .	. . . . .
Date	Student Name

Abstract

Pioneer work has found some signatures of shape memory effect in zirconia based ceramics a few decades ago. However, little work has been carried on since then due to the brittleness and microcracks in the ceramics. This makes it impossible to observe full cycle of shape change and recovery (i.e. shape memory effect). The small magnitude of recoverable strain also limits potential engineering application.

Inspired by the work on shape memory alloys, we propose that when the brittle yttria stabilized zirconia (YSZ) are in small volume with high surface area-to-volume ratio, the surface can relieve much of the stress concentrated at grain boundaries, enabling the occurrence martensitic phase transformation and laying a solid foundation for the potential shape memory effect. To prove the hypothesis, we have prepared small volume YSZ ceramics with desired crystal phase, signatures of martensitic transformation were observed without fracture and the hypothesis was proven. However, a large behavior variation was observed in terms of characteristic shape deformation properties like transformation stress and recoverable strain, mainly due to the existence of grain boundaries in YSZ ceramics with nanoscale grains.

Our strategy to tackle this challenge was to increase the grain size of the YSZ ceramics to enable single crystal ceramic pillars, by introducing extra dopant of titania. With the introduction of titania, we managed to develop the yttria-titania doped zirconia (YTDZ) ceramics with microscale grains. Characterization of the YTDZ ceramics at grain-scale confirmed the tetragonal phase is present, which is desirable for stress-induced martensitic transformation.

The study of martensitic transformation temperatures of YTDZ ceramics guides us to select suitable compositions for potential shape memory effect. The established relationship between martensitic transformation and testing temperatures could be very useful when high temperature applications are desired.

The single crystal YTDZ pillars at microscale demonstrated tremendous improvement in fracture strength, enabling robust and reliable shape memory effect, with transformation stress as high as 2.6 GPa and transformation strain of 2.6%. More importantly, the single crystal structure eliminates the effect of grain boundaries, and

therefore allows us to quantitatively study the characteristic shape memory properties by decoupling the controlling parameters.

A systematic study on the single crystal YTDZ pillars revealed that the featuring shape memory properties are determined by the thermodynamics of stress-induced martensitic transformation. A few controlling parameters such as crystal orientation, testing temperature, ceramic dimension and ceramic composition were explored.

Maps for the featuring shape memory properties were constructed over the crystal orientation variation. Such maps suggest that the preferred orientations are different for high martensitic transformation stress, high transformation strain or large energy dissipation. Therefore, depending on the applications, we are able to use ceramics with orientations that maximize the desired properties.

In addition to crystal orientation, it was discovered that more doping oxides, larger ceramic dimensions and higher test temperatures all can increase the critical stress for martensitic transformation of zirconia ceramics, and therefore enhance the energy dissipation capacity.

The shape memory ceramics made at micro- and nanoscale could have tremendous value for potential applications like sensing, actuation, energy harvesting and conversion, and mechanical damping. The scientific understanding of structure-property relationship may also serve as a possible solution for similar scaling down effect in other systems and as a guide for material selection for various applications in future.

Acknowledgements

First and foremost I want to thank my supervisor Associate Professor Gan Chee Lip for his support, encouragement and patience throughout my time as his student. I have been extremely lucky to have a supervisor who not only inspires me about my thesis work but also teaches me proper skills to be a good scientist. Without his guidance as a great mentor, this work would not have been possible.

I would like to express my sincerest appreciation to my co-supervisor Dr Du Zehui. To her I owe a great debt of gratitude for her patience, inspiration and friendship. I appreciate in particular her invaluable sharing of research experience and the joy of discovery which is the very heart of research. Under her mentorship, I have attained skills to conduct proper research and data analysis. She has been an unfailing source of encouragement and support during difficult times.

Secondly, my special gratitude goes to my previous supervisor, the late Professor Ma Jan. The joy and enthusiasm he had for his research was contagious and motivational for me and his utmost encouragement and teaching has been an invaluable precious for me. It was a great honor to work with him and his death is a great loss to all.

I am very grateful for the support and inspiration from Prof. Christopher A Schuh. With his enthusiasm for research and interdisciplinary research experience, his invaluable advice has helped me develop serious scientific approaches to analysis results in research. I must also express my gratitude to our collaborator Mr. Alan Lai for a total of three productive months in MIT. The discussion with him has always been inspiring and joyful. I am very much appreciated his enthusiasm, intensity, willingness to work on the shape memory ceramics and it is my pleasure to work with him.

I am also very grateful for Mr. Shahrouz Amni and Asst Prof Ali Gilles Tchenguise Miserez, for their kind help with nanoindentation testing and inspiring discussion on ceramic mechanical property. My sincere thanks also goes to Dr. Nobumichi Tamura for his kind help in μXRD experiments and discussion on data analysis.

I am also greatly indebted to companionship of my fellow lab mates, Dr Liu Qing for his training and help with FIB, Dr. Wahyuaji Narottama Putra for his training and

help with EBSD, Mr Luodewei, Mr Yang hao and Dr Lin hui for the discussion and advice on ceramic processing.

I would like to acknowledge the fine work of staffs in FACTS lab for all the technical support. Jason Scott Herrin has generously donated his time and expertise to help me analyze EMPA results. Zviad Tsakadze and Stevin Snellius Pramana have offered great help with XRD testing. Ang Derrick has provided training, offered advice and shared tip about FESEM.

Without the love and support of my family, this would have been a very hard journey. I thank my husband Zhonghan for his unconditional support on pursuing my Ph. D study. I thank my father for teaching me good values such as hard work and appreciation for the gift of life and my mother without whom I would not be the person that I am today. My love for them is eternal.

Table of Contents

Table Captions

Figure Captions

Abbreviations

DSC	Differential Scanning Calorimetry
EBSD	Electron Backscattered Diffraction
EPMA	Electron Probe Microanalysis
FESEM	Field Emission Scanning Electron Microscopy
μXRD	Micro x-ray Diffraction
SAED	Selected Area Electron Diffraction
SMA	Shape Memory Alloys
SMC	Shape Memory Ceramics
SMM	Shape Memory Materials
TEM	Transmission Electron Microscopy
XRD	X-ray Diffraction
YSZ	Yttria Stabilized Zirconia
YTDZ	Yttria-titania doped zirconia

Chapter 1
Introduction

Shape memory material (SMM) is a type of smart material called stimulus-responsive material[1], which includes the well-known shape memory alloys (SMAs)[2,3], shape memory polymers[4-7], shape memory ceramics (SMCs)[8] and the newly emerging shape memory hybrid and composite[9,10]. It has received increasing attention due to its unusual properties of shape memory effect, with large recoverable strain and high damping energy[11]. One well-known group of SMMs is martensitic shape memory materials[12]. This type of material can undergo reversible martensitic transformation between two distinct phases in response to changes in temperature and/or load excursions[13]. Such transformation results in large recoverable shape change and the material exhibits special properties of shape memory effect[14]. The coupling of shape change in response to temperature and load induced by crystallographically reversible martensitic phase transformation is the essential feature enabling the exploration of martensitic transformations for shape memory properties[15].

1.1 Hypothesis

Since most martensitic SMMs that go through reversible martensitic phase transformation are polycrystals, the bulk material is brittle and prone to intergranular fracture during transformation[16,17]. It has been discovered that by producing the SMA material in microscale and nanoscale, the normally brittle materials can be more ductile and can potentially exhibit large reversible shape memory strains[18-20]. Considerable researches have revealed that scaling down the material size could dramatically enhance the shape memory effect of martensitic shape memory material such as Cu-Al-Ni alloy[21] and single crystal Ti alloys[22]. It has been reported that the reversible martensitic phase transformation can occur in nanoscale volume for the well-studied SMA system such as NiTi-based alloy[23-25] and Cu-based alloy[26].

Although the martensitic transformation in zirconia based ceramics has been well known as the foundation of so-called "transformation toughening"[27,28], pioneer work have shown that the essential features of shape memory effect were observed in martensitic-forming bulk ceramics such as ceria-doped zirconia[29-32]. However, the transformation of ceramics often lead to microcracking due to high stresses concentrated at grain boundaries, making it almost impossible to observe the full shape memory effect and multiple cycling of shape recovery due to quick declination[33,34]. The small magnitude of only 0.42% recoverable strain of SMC also limited the technological application[35].

We herein propose that *when normally brittle yttria stabilized zirconia (YSZ) ceramics are produced in small dimensions with high surface area-to-volume ratio, the surface can relieve much of the stress associated with the martensitic phase transformation, enabling the possibility of full shape memory effect without experiencing cracking*[36]. In addition, composition modification could help eliminate the grain boundaries where stress is concentrated, and single crystal YSZ ceramics at small volume could be achieved. Therefore, brittle fracture can be suppressed and shape memory strain can be enhanced, improving the shape memory performance of ceramics. The advantages of high hardness grant YSZ ceramics the possibility to sustain much larger stress compared to SMAs, serving as candidates for various possible new applications when high load is preferred. The single crystal YSZ ceramics also makes it possible to

systematically investigate the martensitic transformation related factors that affect the performance of shape memory ceramics, offering a reliable and fast assessment on the property-structure relationship of YSZ ceramics. The SMCs made by micro- and nanoscale ceramics can have tremendous value for potential applications like sensing, actuation, energy harvesting and conversion, and mechanical damping.

1.2 Objectives and Scope

This thesis aims to develop robust shape memory ceramics with fine scale zirconia to exhibit properties of high strength and large recoverable strain. The objective can be accomplished by firstly proving the hypothesis that reducing the YSZ ceramics size to microscale could enable the occurrence of martensitic transformation without experiencing fracture. With the hypothesis proven, the YSZ ceramics will be modified to enable single crystal structure at small volume, so as to develop reliable shape memory ceramics with high strength and ductility. By studying the relationship between structural parameters and mechanical properties of zirconia ceramics, we aim to develop a thorough understanding of how the ceramic structure is related to shape memory effect. A systematic investigation will be conducted regarding the effects of parameters such as zirconia diameter and height, grain size, crystal orientation and ceramic composition on the properties of recoverable strain and critical stress to trigger transformation. The scientific understanding of structure-property relationship may also serve as a possible solution for similar scaling down effect in other systems and as a guide for material selection for various applications in future.

1.3 Dissertation Overview

The thesis addresses:

Chapter 1 presents the basic concepts of shape memory ceramics and the challenges currently face by the researcher. The hypothesis has been proposed, and our project goal and scope has been outlined.

Chapter 2 reviews the literature concerning shape memory ceramics. The

fundamentals of shape memory effect and its underlining mechanism of martensitic transformation are discussed. This chapter also reviews the studies on size effect and crystal orientation dependence of shape memory alloys and ceramics.

Chapter 3 discusses the underlying principles of the synthesis and characterization techniques for the study of small volume ceramics. It provides detailed description of experimental methodology, including the fabrication of bulk yttria stabilized zirconia (YSZ) and yttria-titania doped zirconia (YTDZ) ceramics, micro-machining of small volume ceramics and mechanical test conducted to explore the shape memory effect.

Chapter 4 presents a systematic characterization and comparison between YSZ and YTDZ ceramics, including the studies of their microstructure, grain size and composition phase. The localized grain-scale characterization of phase and chemical composition will be elaborated in preparation for small volume ceramics.

Chapter 5 investigates and compares the shape memory effect in small volume YSZ and YTDZ ceramics. It explores signatures of martensitic transformation during compressive loading, from both the load-displacement curve and ceramic morphology. This chapter also provides direct assessment of the phase transformation during compression with transmission electron microscopy (TEM).

Chapter 6 addresses the question of characteristic temperatures for martensitic transformation, a key property to assess whether a ceramic can have shape memory effect.

Chapter 7 systematically studies the controlling factors of martensitic transformation and the resultant shape memory properties, including the crystal orientation, test temperature, ceramic dimension and ceramic composition. It provides a general assessment on the structure-property relationship in small volume YTDZ ceramics.

Chapter 8 concludes the thesis and addresses the extent to which the hypothesis is proven. It also includes some reconnaissance studies on the exploration of dopant for YSZ ceramics and potential superelasticity properties. The opportunities and strategies for future work are also discussed.

1.4 Findings and Outcomes

This research has led to several novel outcomes by:

1. Establishing a novel methodology for the development of single crystal shape memory zirconia ceramics at micro/nanoscale.
2. Obtaining scientific understanding on the effects of dopant on the morphology and phase composition of zirconia ceramics.
3. Studying the characteristic temperatures for martensitic transformation to assess the suitability of ceramics for shape memory effect.
4. Developing systematic understanding on the controlling effects of shape memory effect, including the orientation dependence, size effect, composition dependence and testing temperature effect.

References:

[1] D. Roy, J. N. Cambre & B. S. Sumerlin. *Prog Polym Sci.* **2010**, 35, 278-301.
[2] K. Otsuka & X. B. Ren. *Intermetallics.* **1999**, 7, 511-528.
[3] J. Ma, I. Karaman & R. D. Noebe. *Int Mater Rev.* **2010**, 55, 257-315.
[4] C. Liu, H. Qin & P. T. Mather. *J Mater Chem.* **2007**, 17, 1543-1558.
[5] M. Behl & A. Lendlein. *Mater Today.* **2007**, 10, 20-28.
[6] A. Lendlein & S. Kelch. *Angew Chem Int Edit.* **2002**, 41, 2034-2057.
[7] M. Behl, M. Y. Razzaq & A. Lendlein. *Adv Mater.* **2010**, 22, 3388-3410.
[8] F. El Feninat, G. Laroche, M. Fiset & D. Mantovani. *Adv Eng Mater.* **2002**, 4, 91-104.
[9] Z. G. Wei, R. Sandstrom & S. Miyazaki. *J Mater Sci.* **1998**, 33, 3763-3783.
[10] S. A. Madbouly & A. Lendlein. *Adv Polym Sci.* **2010**, 226, 41-95.
[11] I. S. Gunes & S. C. Jana. *J Nanosci Nanotechno.* **2008**, 8, 1616-1637.
[12] R. D. James & K. F. Hane. *Acta Mater.* **2000**, 48, 197-222.
[13] K. Otsuka & X. Ren. *Prog Mater Sci.* **2005**, 50, 511-678.
[14] J. Van Humbeeck. *Adv Eng Mater.* **2001**, 3, 837-850.
[15] S. A. Shabalovskaya. *Bio-Med Mater Eng.* **1996**, 6, 267-289.
[16] Y. M. Jin & G. J. Weng. *Thin Solid Films.* **2000**, 376, 198-207.
[17] H. Yoshida, K. Matsui & Y. Ikuhara. *J Am Ceram Soc.* **2012**, 95, 1701-1708.
[18] J. M. S. Juan, M. L. No & C. A. Schuh. *Adv Mater.* **2008**, 20, 272-+.
[19] W. W. Liang & M. Zhou. *Solid Mech Appl.* **2007**, 144, 135-144.
[20] W. W. Liang, M. Zhou & F. J. Ke. *Nano Lett.* **2005**, 5, 2039-2043.
[21] J. S. Juan, M. L. No & C. A. Schuh. *Nat Nanotechnol.* **2009**, 4, 415-419.
[22] Q. Yu, Z. W. Shan, J. Li, X. X. Huang, L. Xiao, J. Sun & E. Ma. *Nature.* **2010**, 463, 335-338.

[23] J. Ye, R. K. Mishra, A. R. Pelton & A. M. Minor. *Acta Mater.* **2010**, 58, 490-498.
[24] H. G. Kim. *J Korean Phys Soc.* **2012**, 60, 472-476.
[25] V. Demers, V. Brailovski, S. D. Prokoshkin & K. E. Inaekyan. *Mat Sci Eng a-Struct.* **2009**, 513-14, 185-196.
[26] H. S. Zhang & K. Komvopoulos. *Journal of Materials Science.* **2006**, 41, 5021-5024.
[27] R. H. J. Hannink, P. M. Kelly & B. C. Muddle. *J Am Ceram Soc.* **2000**, 83, 461-487.
[28] P. M. Kelly & L. R. F. Rose. *Prog Mater Sci.* **2002**, 47, 463-557.
[29] M. V. Swain. *Nature.* **1986**, 322, 234-236.
[30] P. E. Reyesmorel, J. S. Cherng & I. W. Chen. *J Am Ceram Soc.* **1988**, 71, 648-657.
[31] K. Bhattacharya, S. Conti, G. Zanzotto & J. Zimmer. *Nature.* **2004**, 428, 55-59.
[32] Z. G. Wei, R. Sandstrom & S. Miyazaki. *J Mater Sci.* **1998**, 33, 3743-3762.
[33] A. Shimamoto, H. Y. Zhao & H. Abe. *Int J Fatigue.* **2004**, 26, 533-542.
[34] R. Matsui, Y. Makino, H. Tobushi, Y. Furuichi & F. Yoshida. *Mater Trans.* **2006**, 47, 759-765.
[35] A. Kroger, R. Wernhardt, C. Somsen, G. Eggeler & A. Wieck. *Mat Sci Eng a-Struct.* **2006**, 438, 513-516.
[36] P. X. Gao, W. J. Mai & Z. L. Wang. *Abstr Pap Am Chem S.* **2007**, 234.

Chapter 2

Literature Review

This chapter reviews the literature of shape memory materials, with focus on the martensitic shape memory alloys and ceramics. Previous research on the fundamentals of shape memory effect and its underlining mechanism of martensitic transformation are reviewed. This chapter also reviews the controlling parameters for characteristic shape memory properties in alloys and ceramics, including material dimensions, crystal orientation and testing temperatures.

2.1 Overview of Shape Memory Materials

Shape memory materials, as the name implies, refer to materials with the capability to remember and recover their shape when the right stimulus is applied[1]. Shape memory materials that demonstrate shape memory effect can be directly associated with two distinguishably different underlining mechanisms: reversible phase transformation for shape memory alloys (SMAs) and ceramics (SMCs)[2]; and dual-segment/domain system for shape memory polymers (SMPs)[3].

The phase transformation in SMAs and SMCs could be martensitic, viscoelastic, ferroelectric or ferromagnetic[4]. The martensitic shape memory effect originates directly from the reversible martensitic transformation between the austenite and martensite phases, which can be triggered by heat or stress[5]. Some mica glass materials exhibit viscoelastic shape memory effect, that is, when the principle crystalline phase is dispersed in a continuous glassy phase, the viscous plastic strain developed during heating leads to the shape memory effect[6]. The ferroelectric shape memory effect mainly arises from the large strain generated as a result of paraelectric, ferroelectric and antiferroelectric phase transition[7-9]. The ferromagnetic shape memory effect is magnetic responsive and exhibits recoverable lattice distortion when undergoing paramagnetic, ferromagnetic and antiferromagnetic transition[10-12].

Among all the shape memory mechanisms in SMAs and SMCs, those thermo-responsive ones originate from martensitic phase transformation are of particular interest to us. As the martensitic transformation in these materials can be triggered by external load, the materials are able to deform much significantly in a pseudo-elastic manner[13], i.e. the deformation can be fully recovered without introducing permanent structural damage. In other words, the shape memory effect can enhance the “ductility” of a material, which is of particular importance for brittle materials like ceramics. In the following sections, we will review in detail the reversible martensitic phase transformation and shape memory effect, including the working principle of martensitic transformation and the corresponding thermomechanical behavior[14]. Subsequently, the literature work on thermo-responsive SMAs and SMCs with different structures will be discussed, followed by the review on the key structure-property parameters in SMAs and SMCs.

2.2 Martensitic Transformation induced Shape Memory Effect

Reversible martensitic transformation is a diffusionless, displacive and thermoelastic solid-state phase transition[15]. The high temperature austenite phase and low temperature martensite phase that go through the transformation have a reproducible orientation relationship[16,17]. It involves the coordinated movement of atoms and is characterized by a rapid change of crystal structure as shown in Figure 2.1(a), resulting in a significant shape change[18]. The martensite (monoclinic) phase in zirconia is the equilibrium phase at room temperature and it is defined as the crystal structure formed during diffusionless phase transformation, not the product formed by quenching as defined in traditional steel systems[19]. On the other hand, the austenite (tetragonal) phase is not an equilibrium phase at room temperature. However, after doping with oxides (Y_2O_3 or CeO_2), the cation diffusion in zirconia becomes so slow that it has been proven particularly difficult to establish equilibrium phases at room temperature. The slow diffusion kinetics means that metastable extensions of the phases (tetragonal) can readily occur at room temperature and the phase diagram (Figure 2.4) includes the metastable tetragonal phase. This transformation can be induced by external stress or change in temperature, and involves a significant shear strain and volume change[20]. Martensitic transformation has been discovered in many materials, such as metals, metallic alloys, ceramics[21], but only those with reversible transformation and involve large strain (> 3%) can potentially lead to shape memory effect[22].

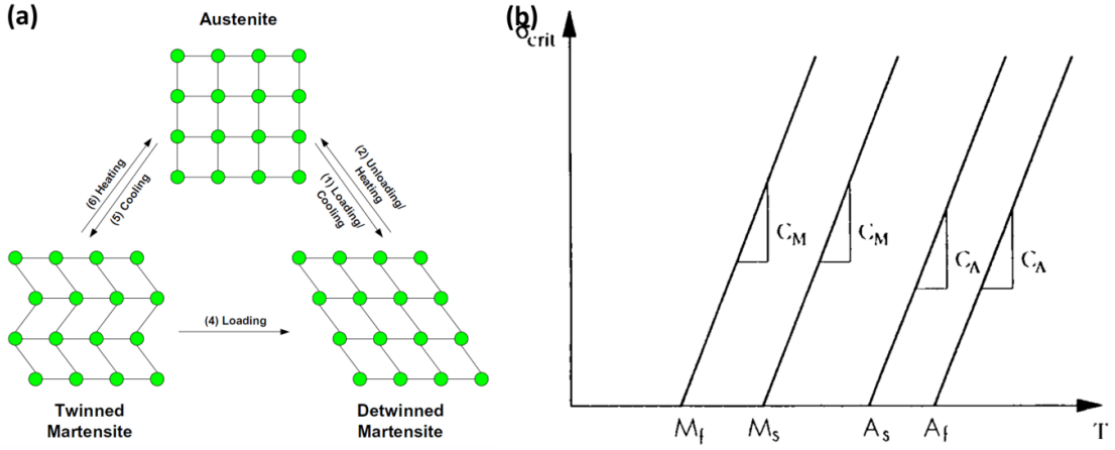

Figure 2.1 (a) Change in lattice structure during martensitic transformation[1]. (b) Critical stresses for transformation as functions of temperature. C_M and C_A are the slopes of the critical stress

curves for the austenite to martensite transformation and the reverse transformation, respectively[23].

The martensitic transformation is featured by four characteristic temperatures during heating and cooling cycles[1]. Upon cooling, the martensitic transformation occurs from M_s (martensite start temperature) to M_f (martensite finish temperature); whereas upon heating, the reverse martensite transformation starts at A_s (austenite start temperature) and ends at A_f (austenite finish temperature). The transformation temperatures are related to the externally applied stress[23], as shown in Figure 2.1(b). The thermal-mechanical property of martensitic transformation provides the foundation for the study of shape memory effect, with only those with transformation temperatures close to the testing temperature can exhibit shape memory effect[1].

To enable shape memory effect, the load should be applied at temperature between M_f and A_s, so that the stress-induced martensitic transformation occurs[24] and causes significant deformation[25] as shown in Figure 2.2(a). Therefore, the deformed material is able to recover to its original shape by heating over the phase transformation temperature to above A_f, at which the reverse martensitic transformation occurs[26]. The ideal stress strain curve for shape memory material should be similar to Figure 2.2(b). Upon applying of load, the stress should initially show liner relationship against strain, with the slope corresponding to the Young's modulus of the austenite phase. At a critical stress, a sudden strain plateau should be observed as the material goes through martensitic transformation from austenite phase to martensite phase, resulting in large shape change. If the applied stress keeps increasing, the stress-strain relationship becomes liner again until reaching the pre-set stress. During unloading, the strain should decreases with stress and achieves a large residual strain after the load is totally removed. Upon heating the material to a higher temperature (above A_f), the martensite phase should go through reverse martensitic transformation and recover back to the original austenite phase.

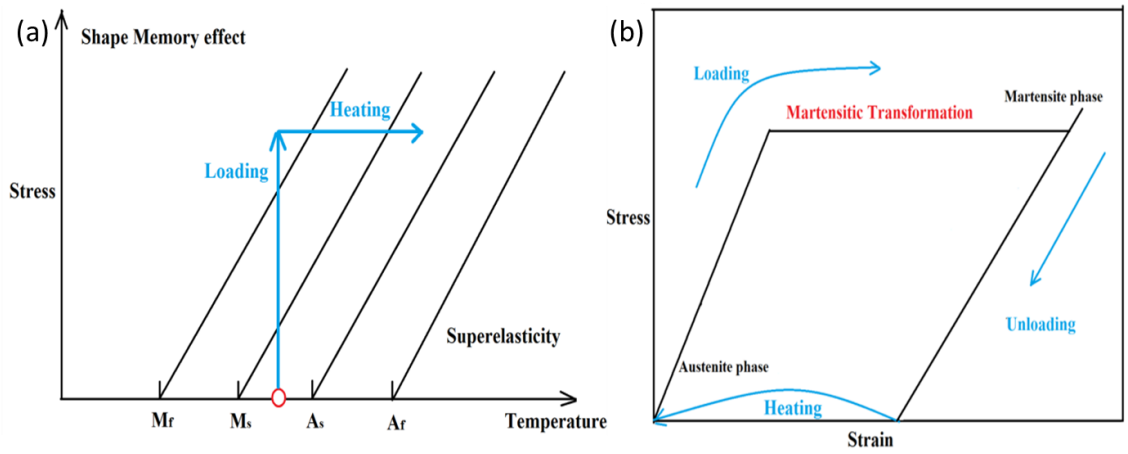

Figure 2.2 (a) Stress-temperature relationship for shape memory effect, (b) Stress-strain relationship for shape memory effect.

2.3 Thermo-responsive Shape Memory Materials

2.3.1 Shape memory alloys

Since the discovery of shape memory effect in Ni-Ti alloys in 1963 by Buehler *et al.*[27], tremendous amount of attention has been drawn to thermo-responsive SMAs[28]. Crystalline SMAs have been reported to have the ability to remember their original shape after deformation and to recover their shape through heating[1,29,30]. SMAs have been recognized as a promising high performance material in the field of shape memory applications as a result of their outstanding properties of large recoverable strain and high damping energy[31]. Such potential has inspired many detailed studies on the famous SMAs including Ti-Ni system alloys[32-34], copper-based alloys[35-39], iron based alloys[40,41] and intermetallic compounds[42-44]. A thorough understanding of bulk SMAs in terms of phenomenon, mechanism and applications have been reviewed by Otsuka[45] and Sun[1].

As has been reviewed by K. Otsuka and X. Ren[46], Ni-Ti based alloys is the most well studied shape memory alloy, due to its good mechanical properties, high ductility, good resistance to corrosion/abrasion and high biocompatibility. A typical stress-strain behavior of Ni-Ti alloy reported by Miyazaki *et al.*[47] is shown in Figure 2.3(a). The alloy has high transformation stress up to ~700 MPa and recoverable strain reaching ~7%; with both parameters changing with test temperature. One of the key applications for Ni-Ti

alloys is in medical field[48]; the good biocompatibility enables them to work in cardiovascular and orthopedic applications or as surgical instruments[49]. For non-medical applications[50], Ni-Ti alloys work well as thermal actuators[51] by converting thermal energy into mechanical energy, due to the simple mechanism, clean work condition and high power/weight ratio. A thorough review on the applications of shape memory alloys has been conducted by Jaronie Mohd Jani *et al.*[52], covering almost every important aspect of applications for SMAs, especially for Ni-Ti alloys.

As compared to Ni-Ti alloys, Cu-based alloys are lower cost materials with shape memory properties, only that they have lower transformation stress of < 200 MPa[30], as shown in Figure 2.3(b). The good shape memory properties and low cost makes Cu-based alloys good candidate in applications such as low thermal expansion (LTD) material[53]. Another important application for SMAs in general is passive energy damping, through directly converting mechanical energy into thermal energy.

Despite all the promising applications, SMAs also face some challenges, including low actuation stresses (generally less than 1 GPa[54]), low energy efficiency in converting heat into mechanical energy, and performance degradation due to microstructure evolution, such as creep and oxidation when subjected to high environmental temperatures[55].

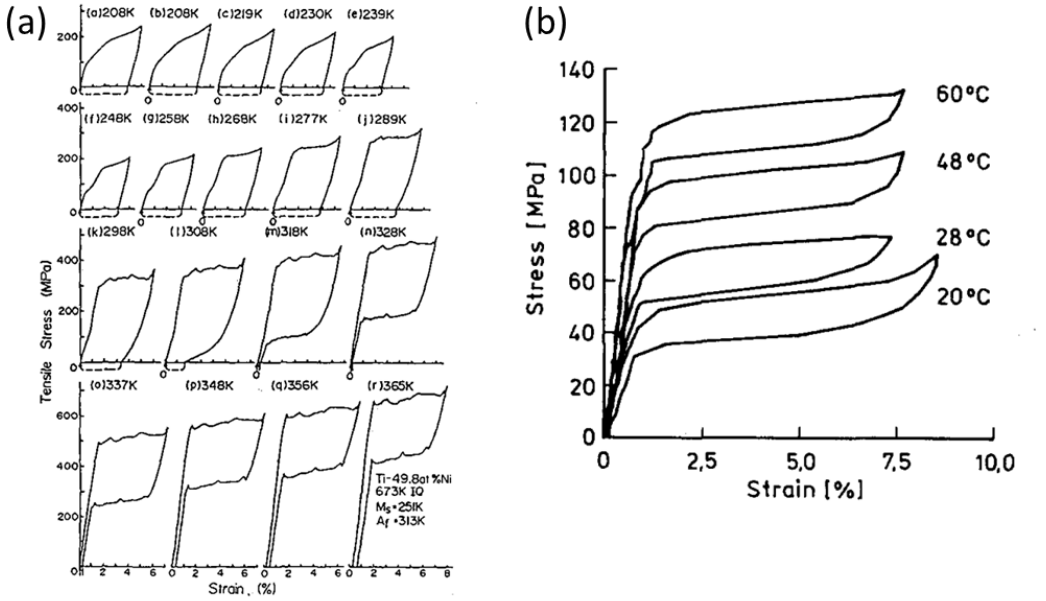

Figure 2.3 Stress-strain behavior of (a) Ti-49.8%Ni alloys[52] at various temperatures and (b) Cu-1.5%Zn-7.1%Al[30] at various temperatures.

2.3.2 Zirconia based shape memory ceramics

Attention has been drawn to zirconia system when it comes to martensitic shape memory ceramics, as zirconia shows outstanding fracture toughness compared to other traditional ceramics[56,57]. Under low pressure[58], zirconia could exist in three phases, including cubic phase at temperature above 2370^{o}C, tetragonal phase from 1170^{o}C to 2370^{o}C, and monoclinic phase at lower temperatures[59]. The large shear and dilatational strain introduced from martensitic transformation between tetragonal phase and monoclinic phase makes zirconia a good candidate as shape memory ceramics. However, the high martensitic transformation temperature (950^{o}C to 1170^{o}C) and accompanying of extensive microcracking during the transition limit the strength and application of pure zirconia as shape memory material[60,61]. By manipulating the microstructure and doping in zirconia[62], martensitic transformation could occur at much lower temperatures and metastable tetragonal phase could be retained at room temperature[63,64]. By the definition of shape memory effect, stabilized zirconia is capable to possess shape memory property at room temperature for materials with martensitic transformation temperature close or slightly above room temperature[59].

It has been conclusively reported that higher doping concentration results in lower martensitic transformation temperature[65]. The doping concentration is one key factor in determining the martensitic transformation temperature as shown in the phase diagram of ZrO_2-Y_2O_3 system[15] in Figure 2.4(a) and ZrO_2-CeO_2 system[66] in Figure 2.4(b). The tetragonal zirconia polycrystalline (TZP) contains almost 100% fine-grained tetragonal phase. It could either be stabilized by adding small amount of yttria[67], ceria[68] or by making nanoscale tetragonal grains[69]. Partially stabilized zirconia (PSZ) contains a considerable amount of dopant (6-10 mol%) such as magnesia[70,71] and yttria[72,73], with a microstructure of fine tetragonal grains embedded in large cubic grains. The doping stabilization mechanism of zirconia has not been fully understood and one widely accepted theory is based on the oxygen vacancies introduced by the doping cations[74]. The lower-valence oxides of yttria and ceria disfavor the existence of monoclinic phase and help stabilize the more symmetric tetragonal phase and cubic phase[75]. The presence of oxygen vacancies accomplished by dopant cations provide local atomic environment that

is similar to monoclinic phase (with average coordination number (ACN) =7) but differ from the corresponding stoichiometric phase (tetragonal or cubic phase with ACN=8)[76].

A few oxides have been found to be effective in stabilizing the tetragonal phase of zirconia at room temperature, such as CeO_2[77], MgO[78] and Y_2O_3[79]. Among these, Y_2O_3 is considered the most effective stabilizer as less than 4 mol% is sufficient to fully stabilize the tetragonal phase[80]. The stress-induced martensitic transformation at crack tip and the resultant volume expansion have been discovered to play a critical role in enhancing the strength of yttria stabilized tetragonal zirconia polycrystals (Y-TZP)[81], serving as the foundation for "strength toughening" effect in zirconia[67]. However, there is a general lack of observations of shape memory effect in YSZ, although it has been reported in the related ceria doped zirconia systems for about three decades[82,83].

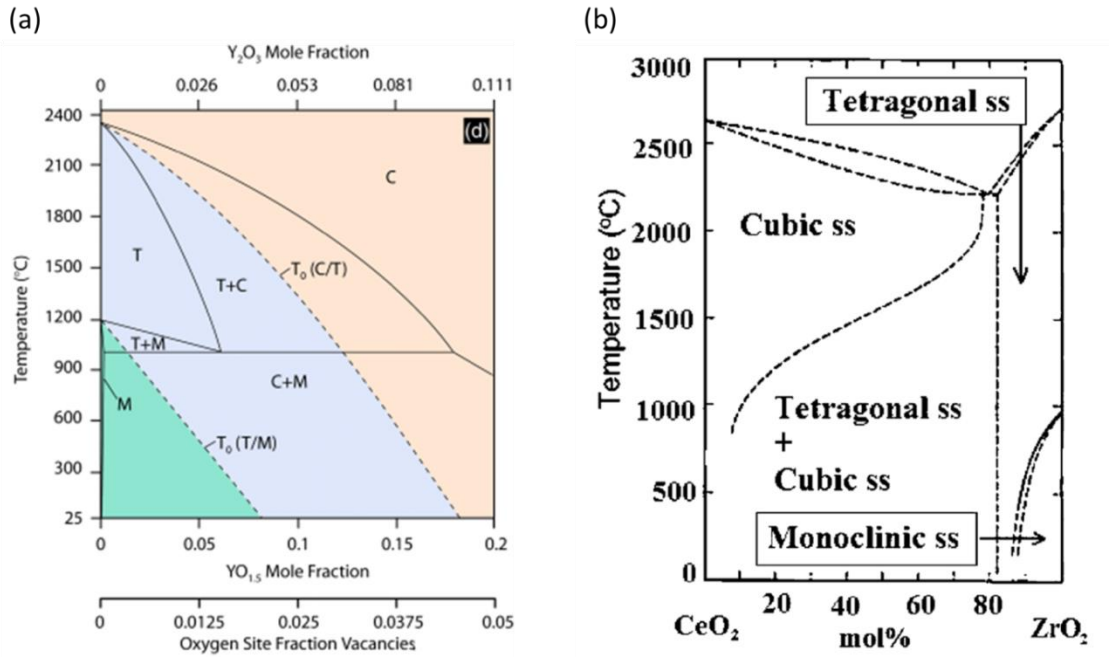

Figure 2.4 Phase diagram of (a) Y_2O_3–ZrO_2 system[15] and (b) CeO_2–ZrO_2 system[66].

Shape memory effect in SMCs has been explored since the discovery of martensitic transformation in zirconia, and the first study can be traced back to 1986, when Swain *et. al* reported that 9.4 mol% MgO partially stabilized zirconia (Mg-PSZ) ceramics were able to recover a strain of about 0.5% after being heated to 800°C[84]. Reyes-Morel *et. al* subsequently reported a comprehensive study on the shape memory effect of 12 mol% CeO_2 stabilized tetragonal zirconia polycrystals (Ce-TZP), where

transformation stress is about 700 MPa and a compressive strain of 1.1% could be recovered through heating[82,83], as shown in Figure 2.5(a). For 3mol% yttria-TZP bulk ceramics, a strain of 2.5% is achieved under a maximum uniaxial stress of 3.8 GPa with residual strain of 0.5% after unloading[85], as shown in Figure 2.5(b).

However, further deformation exceeding 1.1% strain of ceramics generally resulted in microcracking and subsequent microscopic fracture, mainly due to the development of internal mismatch stresses between neighboring grains with different orientations, where the martensitic transformation occurred incommensurately[86]. For zirconia, the martensitic transformation between tetragonal and monoclinic phase involves large shear strain of 16% and volume expansion of 3%[15]. The resulted dramatic strain evolution and redistribution that occurs upon transformation is the source of transformation toughening[87] in bulk zirconia ceramics, as well as potential shape memory properties[84].

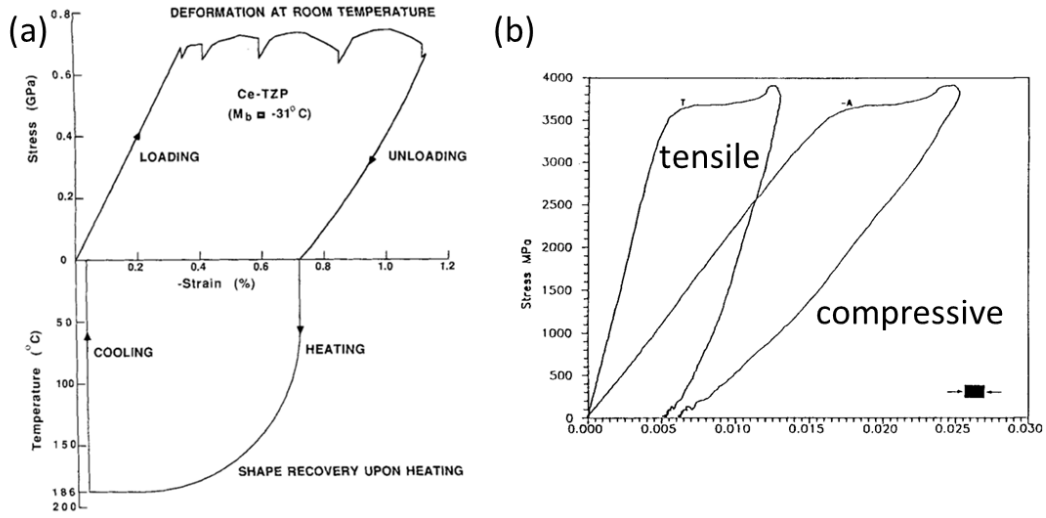

Figure 2.5 (a) Axial stress-strain curve for Ce-TZP under uniaxial compression at room temperature, together with temperature-strain curve showing strain recovery on heating[83]. (b) Stress-strain curves for Y-TZP.

2.4 Shape Memory Materials with Various Structures

The low transformation stress in bulk SMAs and brittle nature of bulk SMCs have driven the study of shape memory effect in different structures like foams, thin films, fibers and microscale structures, with the aim to enhance shape memory effect in

applications with different requirements.

2.4.1 Three-dimension shape memory foams

The promising potential of Ni-Ti alloys as biomedical materials has driven researchers to develop porous SMAs to mimic natural bone structure, not only with high porosity but also to provide appropriate mechanical support. As been reviewed by Wen *et al.* in 2010[88], the yield stresses of porous Ni-Ti alloys vary with different processing methods but generally decrease with increase in porosity, ranging from 200 MPa to 1700 MPa. Among all the processing methods, space-holding sintering using another material as pore template provides best control over porosity and pore size/shape to develop bone-resembling structures[89]. A few highly porous Ni-Ti alloys with porosity of 71~ 87% were developed with space-holding sintering by Xiong *et al.*[90], achieving pore size of 200 ~ 500 μm as shown in Figure 2.6(a), which is very close to that of new bone (pore size of 100 ~ 500 μm). The respective stress-strain behavior of Ni-Ti foam in Figure 2.6(b) shows that the transformation strength is < 40 MPa and recoverable strain reaches 7%, with strength significantly lower than bulk Ni-Ti alloy but comparable strain. They concluded that these highly porous shape memory foams could provide mechanical properties comparable to natural bone. However, it was reported recently that the significantly larger surface area-to-volume ratio could greatly increase the corrosion rate[91], which is critical for biomedical implant. Despite that, the sponge-like structure of shape memory alloys with low weight and high ductility hold significant promise in future applications.

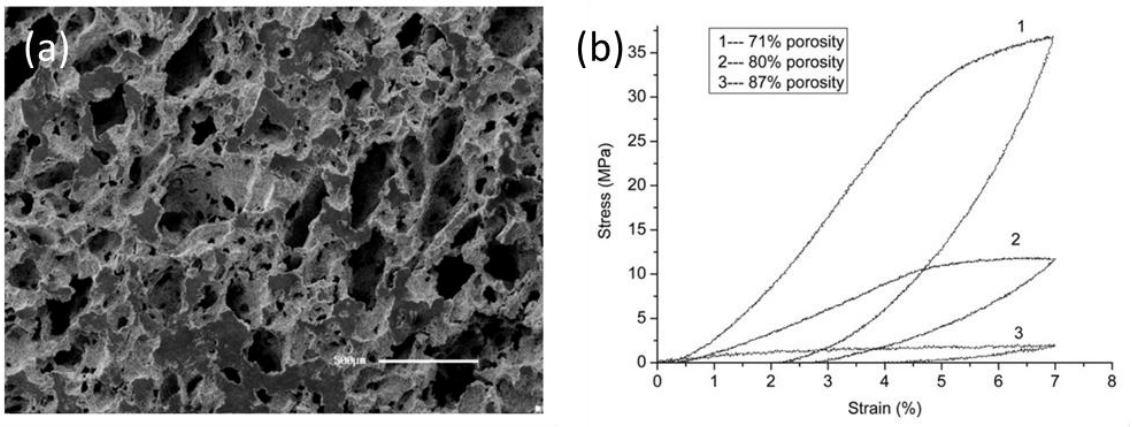

Figure 2.6 (a) SEM of the porous Ti-Ni alloy foam with 71% porosity. (b) Stress–strain behavior of Ti-Ni alloy foam with different porosities.

Due to the lack of reliable shape memory properties in zirconia, there has been not much effort in developing porous ceramic structure for shape memory applications. Nevertheless, researchers have explored a few porous zirconia structures for the enhancement of thermal conductivity and optical properties[92]. Chen *et al.*[93] reported the development of porous zirconia for bone tissue engineering scaffolds, to provide high porosity and reliable mechanical properties. By combining the processing method of template replication with electro-spraying, porous zirconia with pore size of 200 ~ 400 μm was obtained, as shown in Figure 2.7(a), with a compressive strength of ~ 3 MPa achieved at porosity of ~75%. For ultra-high porosity zirconia as shown in Figure 2.7(b), In-Kook Jun *et al.*[94] reported that by using carbon coated polymeric sponge as template, the compressive strength can reach ~ 0.85 MPa at porosity of 96%. It seems clear that the compressive strength of porous zirconia is less than 1% of condensed bulk zirconia, mainly because that the microcracking of brittle zirconia is much more critical in porous structure. We suspect that if the porous zirconia could be modified to have shape memory effect by doping, the high ductility could significantly enhance its strength and the structure could be more useful in applications where mechanical strength is critical.

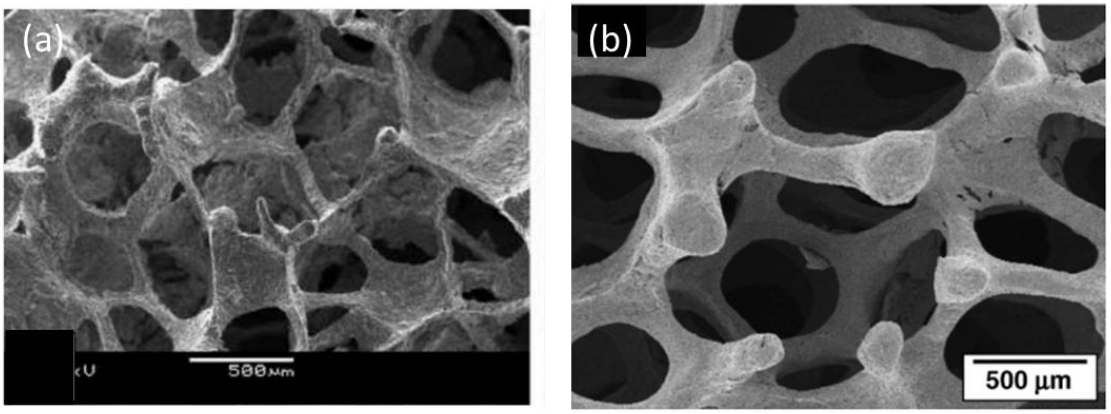

Figure 2.7 (a) SEM of macroporous structure of zirconia foam developed with template replication method with electrospraying[93] (b) SEM of porous zirconia ceramics fabricated with carbon coated polymeric sponge as template[94].

2.4.2 Two-dimension shape memory films

Great effort has been devoted to develop thin film shape memory alloys as it can sustain larger stress, tolerate higher strain and survive more cycles without failure compared to its bulk form[95,96]. The enhanced properties enable thin film alloys to be widely applied in medical devices[97] and actuated micropumps[98,99]. Thin film Ti-Ni based alloys have also been actively investigated as micro-actuators in the rapidly growing field of micro-electro-mechanical systems (MEMSs)[100-102]. The fabrication methods of thin film alloys include sputtering[34,103-106], plasma ion plating[107] and ion beam assisted deposition[108]. Most microscale analysis of SMAs are based on thin film with thickness of few micrometers[109], exhibiting both shape memory effect[110-112] and superelasticity[113,114]. A typical Ti-Ni SMA thin film for MEMS applications was reported by Fu *et al.*[102], that a thin film of Ni-Ti with thickness of ~ 5 μm (Figure 2.8(a)) was deposited on silicon cantilever. The cantilever bended during heating as a result of thermal-induced martensitic transformation in Ni-Ti thin film, as shown in Figure 2.8(b). The tip displacement of cantilever up to 60 mm during transformation temperatures is fairly large (Figure 2.8(c)), showing clear shape memory effect in Ni-Ti thin film. The mechanical properties of sputter-deposited SMA films were summarized by Akira Ishida and Valery Martynov[106], that the yield stress could reach 800 MPa with transformation strain up to 7%, as shown in Figure 2.8(d), which are close to those of bulk SMAs.

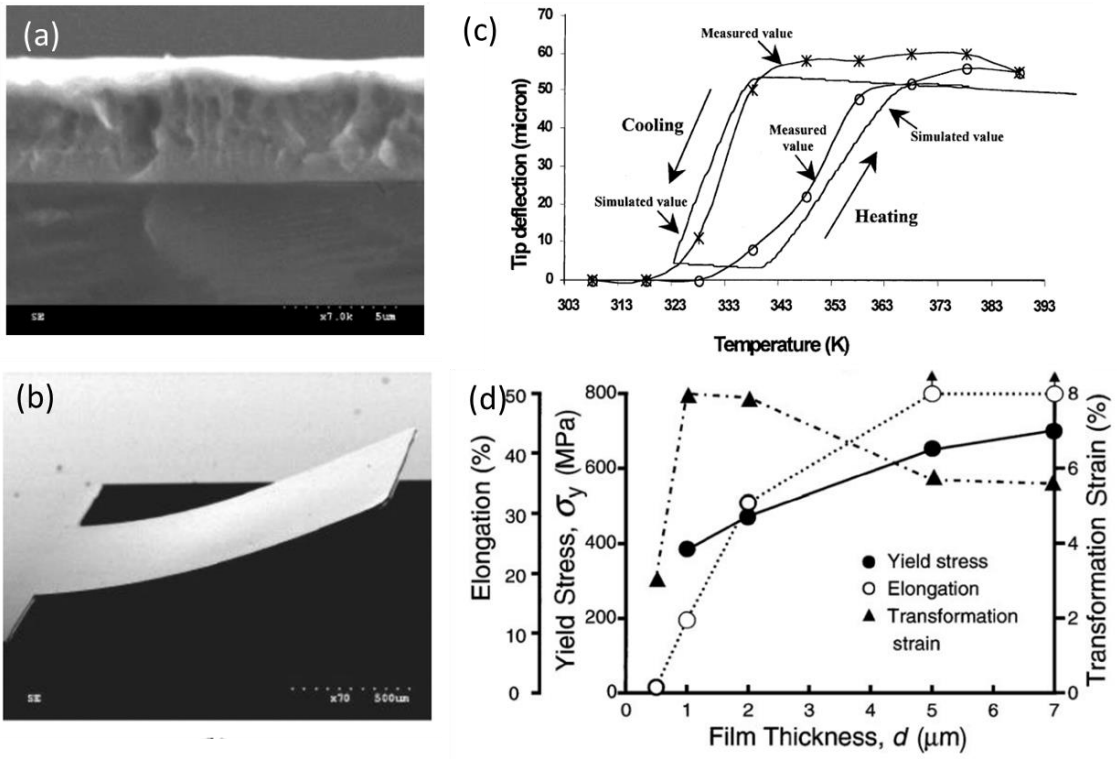

Figure 2.8 (a) Cross-section of the annealed Ti-Ni thin film fabricated with sputtering deposition[102], (b) Silicon cantilever deposited with Ni-Ti films bent during heating for MEMS applications[102]. (c) Displacement of the cantilever beam deposited with Ni-Ti film at different temperatures[102]. (d) Shape-memory behavior and mechanical properties of a Ti-50%Ni thin film with different thickness fabricated with sputtering deposition[106].

Though there has not been much work on developing thin film shape memory zirconia, the study on traditional zirconia thin film has been rather overwhelming due to its excellent electrical properties[115-117]. The most well studied area of thin film zirconia is to use yttria-stabilized zirconia (YSZ) as solid-state electrolytes in solid-oxide fuel cells (SOFCs)[118]. By spray deposition, the zirconia film with thickness of a few micrometers can be deposited on another material[119], as shown in Figure 2.9(b). Regarding the mechanical properties of thin film zirconia, Heiroth *et al.*[120] developed a film of YSZ with thickness of around 500 nm using pulsed lase deposition (Figure 2.9(b)). They discovered that the tetragonal zirconia films exhibited higher fracture toughness than cubic zirconia film, and suggested that the stress-induced martensitic transformation in tetragonal zirconia contributed to the strength hardening effect in such thin film. This work holds significant promise for the potential of shape memory zirconia as thin film,

that martensitic transformation could occur in such structure.

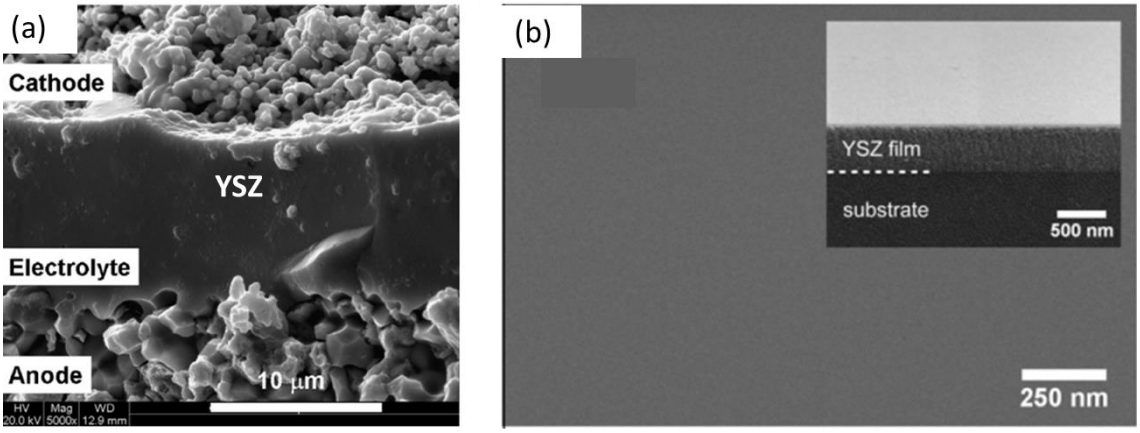

Figure 2.9 (a) SEM of the cross-section of yttria stabilized zirconia (YSZ) as electrolyte on the pre-calcined substrate[119]. (b) SEM of the surface and cross-section (insets) of tetragonal YSZ[120].

2.4.3 One-dimension shape memory fibers

By making SMA into one-dimension fibers with diameter in microscale, the SMA was reported to retain the shape memory effect[121], as shown in Figure 2.10. The recoverable strain reaches 4% with the transformation occurs at ~ 400 MPa; both are slightly lower than that in bulk and thin film SMAs. However, while embedding these fibers in composite materials, they work very well in improving the yield stress and the fracture toughness of the matrix materials[122,123].

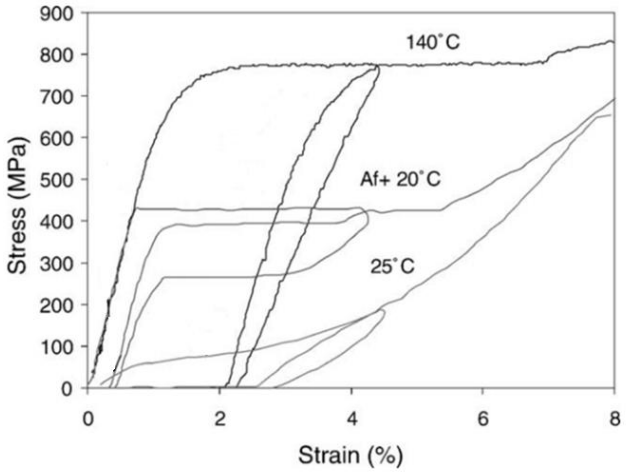

Figure 2.10 Stress-strain behavior of NiTiCu SMA wire (with diameter of 150 μm) at different test temperatures[121].

As been reviewed by Nespoli *et al.*[124], SMA is highly promising to work as mini-actuators. In addition to using SMA thin films as actuators, another well studied approach is to embed one dimensional SMA fibers in composite materials to work as structural enhancement as well as actuator. A detailed study conducted by Furuya *et al.*[122] revealed that by compositing Ni-Ti SMA fibers in Al matrix (Figure 2.11(a) and (b)), the damping capacity of the material could be significantly enhanced at temperature lower than 450K, as shown in Figure 2.11(c). The reinforcement in energy damping capacity is mainly due to the compressive residual stress induced by martensitic transformation in Ni-Ti fibers.

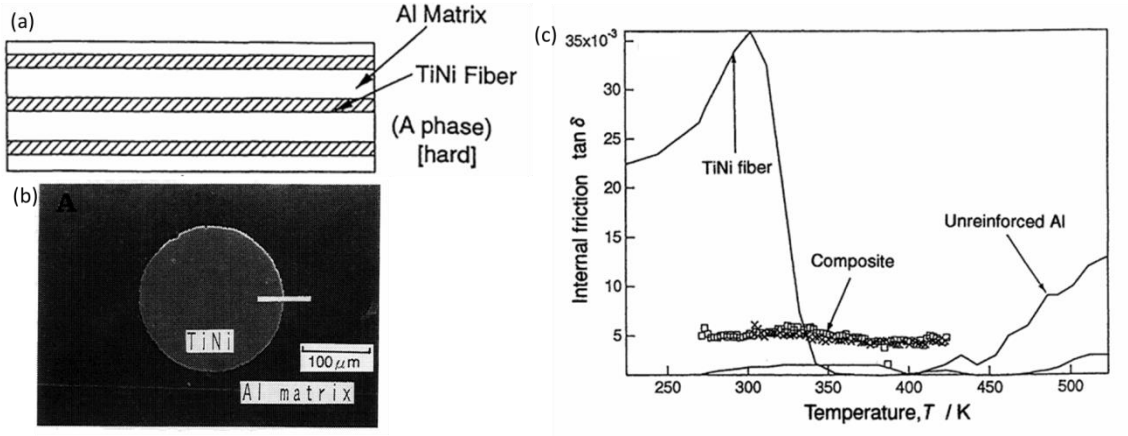

Figure 2.11 (a) Concept of shape memory Ni-Ti fiber /Al composite[122]. (b) SEM of cross section of Ni-Ti fiber/ Al matrix composite[122]. (c) Damping capacity of Ni-Ti fibers, unreinforced Al matrix and composite at different temperatures[122].

Similar to SMAs, zirconia fibers are very promising to work as composite reinforcement material, due to their excellent corrosion resistance, high strength and toughness[125,126]. Zirconia fibers could be produced either through electrospinning[127] or sol-gel[128,129]. Liu *et al.*[130] managed to fabricate continuous zirconia fibers with diameter of 10 ~ 40 μm (Figure 2.12(a)) with length longer than 1 m (Figure 2.12(b)), achieving tensile strength up to 2.8 GPa. To increase the surface area-to-volume ratio of yttria stabilized zirconia as electrolyte in SOFCs, researches have explored the fabrication of hollow zirconia fibers[131,132]. A typical hollow zirconia fiber[133] could be seen in Figure 2.12(c), with the hollow structure shown in Figure 2.12(d) and (e).

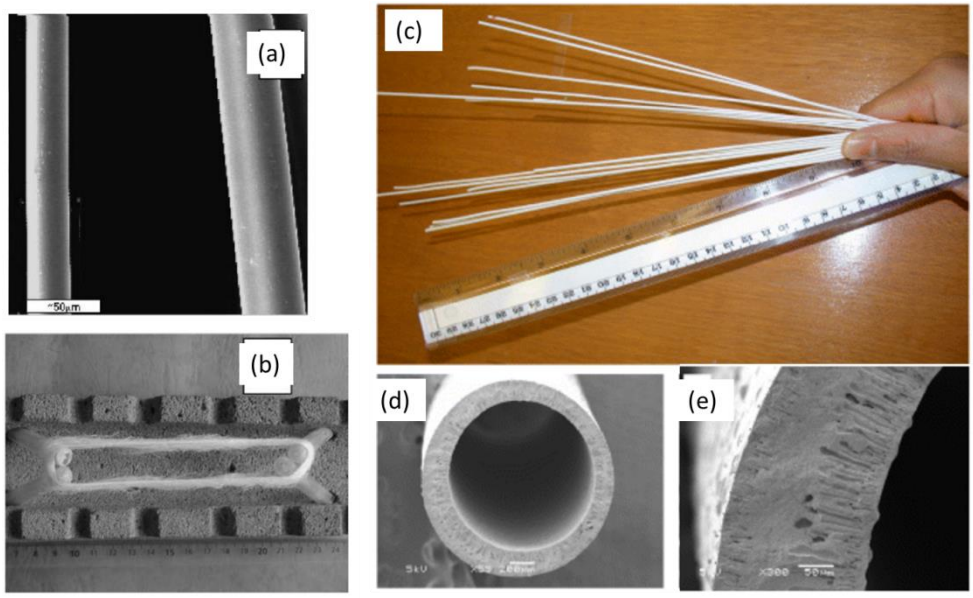

Figure 2.12 (a) SEM of zirconia fibers with (b) length more than 1 m[130]. (c) Picture of yttria stabilized zirconia hollow fibers with the SEM shown in (d) and (e)[133].

2.4.4 Shape memory micro-pillars

The studies on porous foams, thin films, and fibers in SMAs and zirconia have shown that particular structure is critical in changing the mechanical behavior of materials. SMAs in the form of porous structure and the thin film could retain the shape memory properties to a large extent, and illustrate additional properties like lower density and better electrical properties. The mechanical property is affected by both the material elastic constants and the material structure which determines the local stress field. The local stress field which is related to the surface area-to-volume ratio could largely affect the elastic strain energy for martensitic transformation, and ultimately, the shape memory properties[134]. In addition to the size effect on fracture strength, the constraint from surrounding matrix could play a key role in changing the triggering mechanism of martensitic transformation[135]. An extremely case to study the effect of surface area-to-volume ratio is through microscale pillars or particles with controlled sample dimensions.

In an effort to produce SMAs with high surface area-to-volume ratio, San Juan *et al.*[136] have devoted their work to make micro and nanometer scale pillars with focused ion beam. Instrumented micro-compression has been conducted on the pillars with

diameter of ~ 1 μm. They have demonstrated that micro- and nanoscale pillars of Cu–Al–Ni SMA possess excellent shape memory property[137] with recoverable strain up to 7%, as shown in Figure 2.13(a), (b) and (c). The mechanical damping energy of nanosize Cu–Al–Ni SMA was reported to be substantially higher than bulk material, making it highly potential for energy damping application[138], as shown in Figure 2.13(d). The better performance of SMAs in the form of single crystal pillars are mainly attributed to the low structural defects which makes the structure more conductive to uniform loading and leads to higher strength. Ozdemir *et al.*[139] further reported with $Ni_{54}Fe_{19}Ga_{27}$ SMA that pillar size is critical for determining the critical stress for phase transformation, as shown in Figure 2.13(e).

The study of microscale SMA pillars has inspired us to explore the size effect in polycrystalline zirconia ceramics. In our recent work, we showed that microcracking can be mitigated by reducing the sample size to the order of the grain size, thereby forming an oligocrystal structure with greater free surface area and fewer grain boundaries[140]. Such small volume ceramics allow the release of internal stresses at the free surfaces and therefore mitigate cracking. In the 8mol% CeO_2 stabilized zirconia system (with a trace amount of Y_2O_3), our research group has demonstrated a recoverable strain up to 8% without fracture in the oligocrystal pillars, as shown in Figure 2.14(b). The microscale dimension of ceramics is critical to avoid crack right after elastic deformation and enable the occurrence of martensitic transformation.

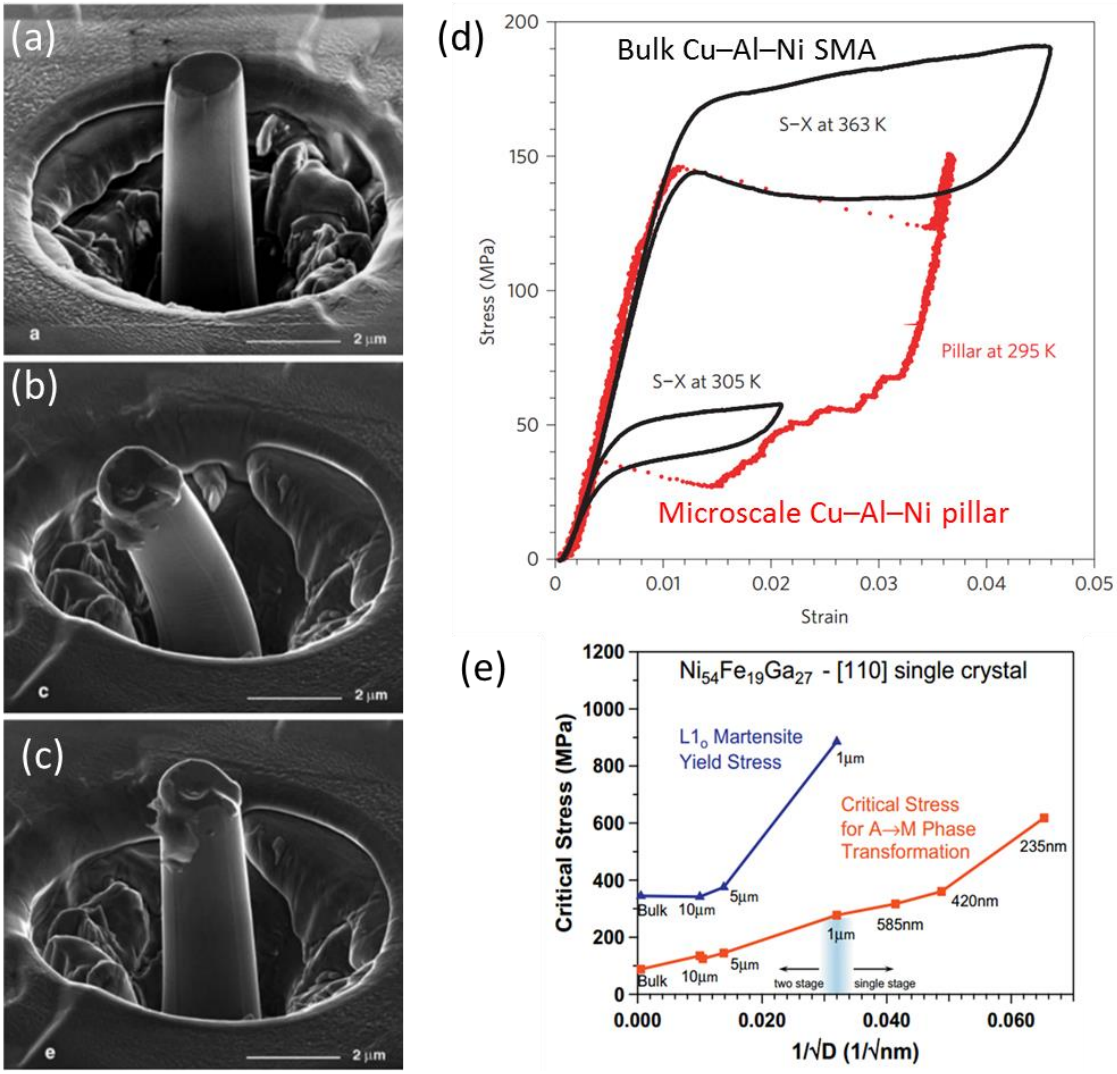

Figure 2.13 (a), (b) and (c) Cu-Al-Ni pillar demonstrating shape memory effect with bending[137]. (d) Comparison of the stress-strain behavior in bulk single crystals and microscale pillars[138]. (e) The transformation stress of $Ni_{54}Fe_{19}Ga_{27}$ pillars with different pillar diameters[139].

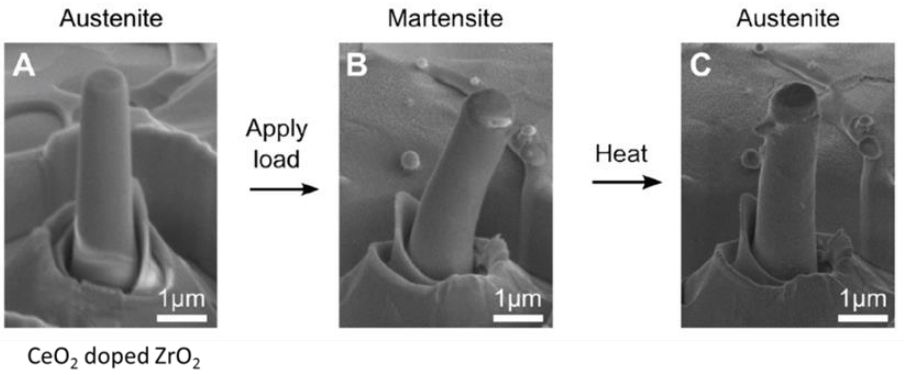

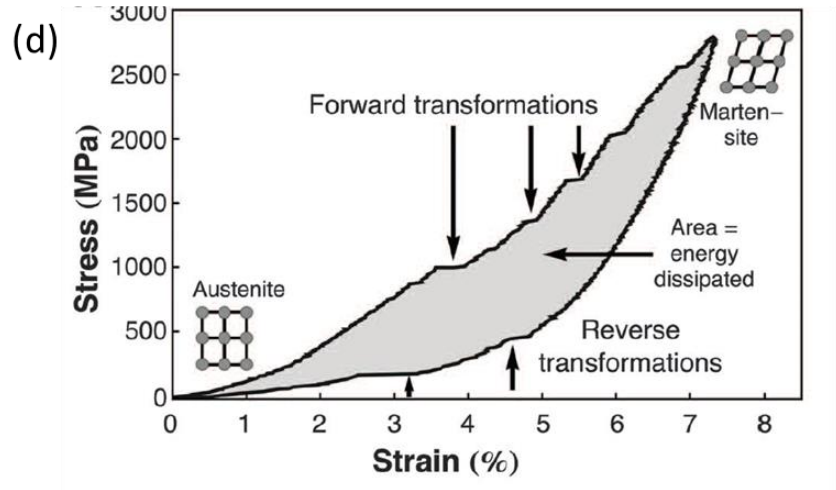

Figure 2.14 (a), (b) and (c) CeO_2 doped zirconia demonstrating shape memory effect with bending[140]. (d) Stress-strain behavior of CeO_2 doped zirconia pillar under compression[140].

2.5 Controlling Parameters for Shape Memory Effect

To obtain a full understanding of shape memory effect in SMAs and SMCs, not only martensitic transformation need to be observed, but also the controlling parameters needs to be understood for the characteristic shape memory properties of transformation stress, recoverable strain and transformation temperatures. The quantitative study of shape memory effect can be approached by a systematic analysis of the underlining mechanism of martensitic transformation. The studies have revealed that, despite the material dimensions[134,136] that have been discussed in section 2.4, crystal orientation[141,142], material composition[143] and test temperature[141] all affect the martensitic transformation, and should consequently affect the martensitic shape memory effect in ceramics.

2.5.1 Crystal orientation dependence of shape memory effect

Due to the difference in crystal symmetry of parent and martensite phases, the martensitic transformation is highly dependent on the crystallographic evolution[52]. Studies on martensitic transformation behavior in SMAs have revealed that the crystal orientation plays a key role to the resulted shape memory behavior in terms of actuation stress and recoverable strain[46]. Saburi *et al.*[54] reported in 1984 that the shape memory effect in Ni-Ti alloy is highly dependent on the crystal orientation, with strain varying significantly from 4% to 12%, as shown in Figure 2.15(a). For Cu-Al-Ni alloy, it was found that both the critical transformation stress and transformation strain are highly dependent on the crystal orientation[141]. The critical stress varies from 0.15 GPa to 0.35 GPa, while transformation strain varies from 4% to 8% for different crystal orientations, as shown in Figure 2.15(b).

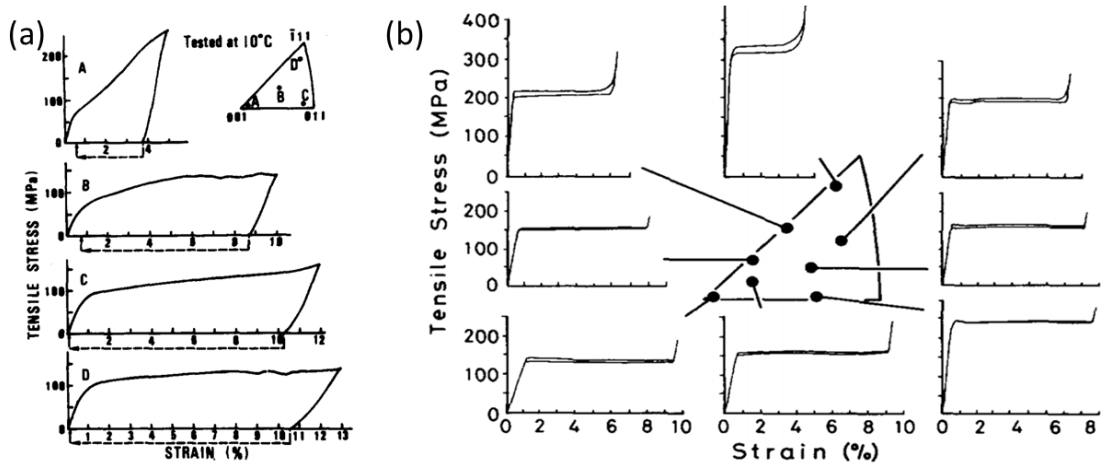

Figure 2.15 Orientation dependence of stress-strain curves for martensitic transformation in (a) Ni-Ti alloy[54] and (b) Cu-Al-Ni alloy[141].

Since the discovery of stress-induced martensitic transformation in zirconia[144], numerous studies have been devoted to understand the corresponding crystal structure transition and the accompanying shape change[15]. The studies of the crystallography between the tetragonal and monoclinic phases revealed that the transformation is highly anisotropic[20,145]. The transformation in response to externally applied stress therefore should be crystallographic dependent, similar to the observation in shape memory alloy[141]. Since the current theory that explains the relationship between martensitic transformation

and microstructure is based on single crystal alloy systems[146], the relationship may not be applicable to ceramic systems with different crystal structures. The polycrystalline ceramic structure further complicates the shape change and fracture behavior, making it a challenge to fully understand the shape memory properties that are observed experimentally. The pioneer work on zirconia discovered that by fabricating small volume oligocrystal pillar, significant shape memory effect can be achieved without interfering with the matrix constraint[140,147]. Such an approach opens up the possibility to fabricate single crystal pillars and systematically study the martensitic transformation and its crystal orientation dependence.

2.5.2 Test temperature dependence of shape memory effect

According to the Clausius-Clapeyron relationship[148], the martensitic transformation stress (σ) is related to testing temperatures (T) by Equation 1:

$$\frac{d\sigma}{dT} = -\frac{\Delta S}{\varepsilon} = -\frac{\Delta H}{T \cdot \varepsilon} \qquad \text{Equation 1}$$

where ΔS and ΔH are the entropy and enthalpy of transformation, while ε is the transformation strain. It was discovered in Cu-Al-Ni alloy that a higher test temperature results in larger transformation stress[141], as shown in Figure 2.3. Both crystal orientation and testing temperatures are found to be critical in determining the stress-strain behavior of martensitic SMAs. Due to the similarly of martensitic transformation between zirconia and SMAs, shape memory zirconia is expected to display similar phenomenon, which will be explored in this thesis. The challenge is to develop single crystal structure for generally nanoscale-grain YSZ ceramics to enable the study of crystal orientation, with which we can decouple the effect of crystal orientation from the testing temperatures. The challenge will be addressed by exploring the oxide additives to increase the grain size from nanoscale to microscale, which will be elaborated in Chapter 4.

2.6 Concluding Remarks

Previous researches on martensitic shape memory materials have been reviewed together with the mechanism for shape memory effect and martensitic transformation.

Various structures of shape memory alloys and ceramics, including bulk materials, porous structure, thin films, fibers and microscale pillars have been discussed on their mechanical properties and applications. It was reported that the shape memory effect in alloys can be affected by various parameters, including the material dimensions, crystal orientations and testing temperatures. This literature work sheds light on the systematic understanding of shape memory ceramics for our thesis work.

Reference:

[1] L. Sun, W. M. Huang, Z. Ding, Y. Zhao, C. C. Wang, H. Purnawali & C. Tang. *Materials & Design.* **2012**, 33, 577-640.
[2] Z. K. Lu & G. J. Weng. *J Mech Phys Solids.* **1997**, 45, 1905-&.
[3] J. S. Leng, X. Lan, Y. J. Liu & S. Y. Du. *Prog Mater Sci.* **2011**, 56, 1077-1135.
[4] Z. G. Wei, R. Sandstrom & S. Miyazaki. *J Mater Sci.* **1998**, 33, 3743-3762.
[5] R. D. James & K. F. Hane. *Acta Mater.* **2000**, 48, 197-222.
[6] K. E. Schurch & K. H. G. Ashbee. *Nature.* **1977**, 266, 706-707.
[7] W. F. Liu, W. Chen, L. Yang, Y. Wang, L. X. Zhang, C. Zhou, S. T. Li & X. B. Ren. *Mat Sci Eng a-Struct.* **2006**, 438, 350-353.
[8] L. Yang, W. F. Liu, W. Chen, Y. Wang, X. L. Cao & X. B. Ren. *Mat Sci Eng a-Struct.* **2006**, 438, 176-180.
[9] J. Y. Li & Y. F. Ma. *Mech Mater.* **2008**, 40, 1022-1036.
[10] G. D. Liu, Z. H. Liu, X. F. Dai, S. Y. Yu, J. L. Chen & G. H. Wu. *Sci Technol Adv Mat.* **2005**, 6, 772-777.
[11] Y. Tanaka, T. Ohmori, K. Oikawa, R. Kainuma & K. Ishida. *Mater Trans.* **2004**, 45, 427-430.
[12] C. M. Craciunescu & M. Wuttig. *J Optoelectron Adv M.* **2003**, 5, 139-146.
[13] K. O. a. K.Shimizu. *International Metals Reviews.* **1986**, 31, 93-114.
[14] K. Bhattacharya. *Continuum Mech Therm.* **1993**, 5, 205-242.
[15] J. Chevalier, L. Gremillard, A. V. Virkar & D. R. Clarke. *J Am Ceram Soc.* **2009**, 92, 1901-1920.
[16] K. Bhattacharya, S. Conti, G. Zanzotto & J. Zimmer. *Nature.* **2004**, 428, 55-59.
[17] H. K. D. H. Bhadeshia. *J Phys Iv.* **1997**, 7, 367-376.
[18] K. Otsuka. *J Phys Iv.* **2001**, 11, 3-9.
[19] S. Berveiller, K. Inal, R. Kubler, A. Eberhardt & E. Patoor. *J Phys Iv.* **2004**, 115, 261-268.
[20] P. M. Kelly & C. J. Ball. *J Am Ceram Soc.* **1986**, 69, 259-264.
[21] Z. Nishiyama, M. E. Fine, M. Meshii & C. M. Wayman. Martensitic transformation. (*: Academic Press,* 1978).
[22] L. Delaey, R. V. Krishnan, H. Tas & Warlimon.H. *J Mater Sci.* **1974**, 9, 1521-1535.
[23] L. C. Brinson. *J Intel Mat Syst Str.* **1993**, 4, 229-242.
[24] R. Delville, B. Malard, J. Pilch, P. Sittner & D. Schryvers. *Int J Plasticity.* **2011**, 27, 282-297.

[25] W. M. Huang, Z. Ding, C. C. Wang, J. Wei, Y. Zhao & H. Purnawali. *Mater Today.* **2010**, 13, 54-61.
[26] K. Otsuka, A. Saxena, J. K. Deng & X. B. Ren. *Philos Mag.* **2011**, 91, 4514-4535.
[27] W. J. Buehler, R. C. Wiley & J. V. Gilfrich. *J Appl Phys.* **1963**, 34, 1475-&.
[28] S. Miyazaki & K. Otsuka. *Isij International.* **1989**, 29, 353-377.
[29] H. Y. Kim, Y. Ikehara, J. I. Kim, H. Hosoda & S. Miyazaki. *Acta Mater.* **2006**, 54, 2419-2429.
[30] M. I & H. Xu. *Acta Metall Mater.* **1991**, 39, 263-271.
[31] Y. Q. Fu, H. J. Du, W. M. Huang, S. Zhang & M. Hu. *Sensor Actuat a-Phys.* **2004**, 112, 395-408.
[32] K. Gall, H. Sehitoglu, Y. I. Chumlyakov & I. V. Kireeva. *Acta Mater.* **1999**, 47, 1203-1217.
[33] S. Miyazaki & A. Ishida. *Mat Sci Eng a-Struct.* **1999**, 273, 106-133.
[34] S. Miyazaki & H. Y. Kim. *Mater Sci Forum.* **2007**, 561-565, 5-21.
[35] S. N. Golyandin, K. V. Sapozhnikov & S. B. Kustov. *Phys Solid State+*. **2005**, 47, 638-645.
[36] N. F. Kennon, D. P. Dunne & L. Middleton. *Metall Trans A.* **1982**, 13, 551-555.
[37] D. Schofield & A. P. Miodownik. *Met Technol.* **1980**, 7, 167-173.
[38] N. Kayah, S. Cakmak, E. Artunc & O. Adiguzel. *J Phys Iv.* **1995**, 5, 895-900.
[39] A. Isalgue, V. Torra, F. C. Lovey & J. L. Pelegrina. *Esomat 2009 - 8th European Symposium on Martensitic Transformations.* **2009**.
[40] A. Sato, E. Chishima, Y. Yamaji & T. Mori. *Acta Metall Mater.* **1984**, 32, 539-547.
[41] H. Otsuka, H. Yamada, T. Maruyama, H. Tanahashi, S. Matsuda & M. Murakami. *Isij Int.* **1990**, 30, 674-679.
[42] Y. N. Koval, G. S. Firstov & A. V. Kotko. *Scripta Metall Mater.* **1992**, 27, 1611-1616.
[43] M. Notomi, K. J. Van Vliet & S. Yip. *Mater Res Soc Symp P.* **2007**, 980, 223-228.
[44] K. K. Song, S. Pauly, Y. Zhang, R. Li, S. Gorantla, N. Narayanan, U. Kuhn, T. Gemming & J. Eckert. *Acta Mater.* **2012**, 60, 6000-6012.
[45] K. Otsuka & X. B. Ren. *Intermetallics.* **1999**, 7, 511-528.
[46] K. Otsuka & X. Ren. *Prog Mater Sci.* **2005**, 50, 511-678.
[47] S. Miyazaki, Y. Ohmi, K. Otsuka & Y. Suzuki. *J Phys-Paris.* **1982**, 43, 255-260.
[48] L. G. Machado & M. A. Savi. *Braz J Med Biol Res.* **2003**, 36, 683-691.
[49] N. B. Morgan. *Mat Sci Eng a-Struct.* **2004**, 378, 16-23.
[50] J. Van Humbeeck. *Mat Sci Eng a-Struct.* **1999**, 273, 134-148.
[51] W. Huang. *Mater Design.* **2002**, 23, 11-19.
[52] J. M. Jani, M. Leary, A. Subic & M. A. Gibson. *Mater Design.* **2014**, 56, 1078-1113.
[53] Y. Sutou, T. Omori, J. J. Wang, R. Kainuma & K. Ishida. *Mat Sci Eng a-Struct.* **2004**, 378, 278-282.
[54] T. Saburi, M. Yoshida & S. Nenno. *Scripta Metallurgica.* **1984**, 18, 363-366.
[55] J. Vanhumbeeck. *J Phys Iv.* **1991**, 1, 189-197.
[56] G. T. M. Stam, E. Vandergiessen & P. Meijers. *Int J Solids Struct.* **1994**, 31, 1923-1948.
[57] G. T. M. Stam & E. vanderGiessen. *Am Soc Test Mater.* **1995**, 1220, 3-18.

[58] R. Terki, G. Bertrand, H. Aourag & C. Coddet. *Mat Sci Semicon Proc.* **2006**, 9, 1006-1013.
[59] X. J. Jin. *Curr Opin Solid St M.* **2005**, 9, 313-318.
[60] Y. L. Zhang, X. J. Jin, T. Y. Hsu, Y. F. Zhang & J. L. Shi. *Scripta Mater.* **2001**, 45, 621-624.
[61] E. C. Subbarao, H. S. Maiti & Srivasta.Kk. *Phys Status Solidi A.* **1974**, 21, 9-40.
[62] P. Li, I. W. Chen & J. E. Pennerhahn. *J Am Ceram Soc.* **1994**, 77, 118-128.
[63] S. Deville, G. Guenin & K. Chevalier. *Acta Mater.* **2004**, 52, 5697-5707.
[64] A. E. Bohe, J. J. A. Gamboa & D. M. Pasquevich. *Mat Sci Eng a-Struct.* **1999**, 273, 218-221.
[65] J. S. Lee, M. Lerch & J. Maier. *J Solid State Chem.* **2006**, 179, 270-277.
[66] F. Zhang, C. H. Chen, J. C. Hanson, R. D. Robinson, I. P. Herman & S. W. Chan. *J Am Ceram Soc.* **2006**, 89, 1028-1036.
[67] D. Casellas, F. L. Cumbrera, F. Sanchez-Bajo, W. Forsling, L. Llanes & M. Anglada. *J Eur Ceram Soc.* **2001**, 21, 765-777.
[68] S. A. Muqtader, B. R. Rao & S. G. Samdani. *J Mater Sci Lett.* **1990**, 9, 1075-1076.
[69] R. Chaim. *Mat Sci Eng a-Struct.* **2008**, 486, 439-446.
[70] D. L. Porter & A. H. Heuer. *J Am Ceram Soc.* **1979**, 62, 298-305.
[71] M. V. Swain. *Acta Metall Mater.* **1985**, 33, 2083-2091.
[72] K. Tsukama & M. Shimada. *J Mater Sci Lett.* **1985**, 4, 857-861.
[73] P. Christel, A. Meunier, M. Heller, J. P. Torre & C. N. Peille. *J Biomed Mater Res.* **1989**, 23, 45-61.
[74] H. T. Chen & J. G. Chang. *J Chem Phys.* **2010**, 132.
[75] P. Dalach, D. E. Ellis & A. van de Walle. *Phys Rev B.* **2010**, 82.
[76] S. Fabris, A. T. Paxton & M. W. Finnis. *Acta Mater.* **2002**, 50, 5171-5178.
[77] K. H. Heussner & N. Claussen. *J Am Ceram Soc.* **1989**, 72, 1044-1046.
[78] P. Duwez, F. Odell & F. H. Brown. *J Am Ceram Soc.* **1952**, 35, 107-113.
[79] A. Suresh, M. J. Mayo, W. D. Porter & C. J. Rawn. *J Am Ceram Soc.* **2003**, 86, 360-362.
[80] H. G. Scott. *J Aust Ceram Soc.* **1981**, 17, 16-20.
[81] R. H. J. Hannink, P. M. Kelly & B. C. Muddle. *J Am Ceram Soc.* **2000**, 83, 461-487.
[82] P. E. Reyesmorel & I. W. Chen. *J Am Ceram Soc.* **1988**, 71, 343-353.
[83] P. E. Reyesmorel, J. S. Cherng & I. W. Chen. *J Am Ceram Soc.* **1988**, 71, 648-657.
[84] M. V. Swain. *Nature.* **1986**, 322, 234-236.
[85] G. Subhash & S. Nematnasser. *J Am Ceram Soc.* **1993**, 76, 153-165.
[86] S. M. Ueland & C. A. Schuh. *J Appl Phys.* **2013**, 114.
[87] A. G. Evans & A. H. Heuer. *J Am Ceram Soc.* **1980**, 63, 241-248.
[88] C. E. Wen, J. Y. Xiong, Y. C. Li & P. D. Hodgson. *Phys Scripta.* **2010**, T139.
[89] A. Bansiddhi & D. C. Dunand. *Acta Biomater.* **2008**, 4, 1996-2007.
[90] J. Y. Xiong, Y. C. Li, X. J. Wang, P. D. Hodgson & C. E. Wen. *J Mech Behav Biomed.* **2008**, 1, 269-273.
[91] A. Biesiekierski, J. Wang, M. A. H. Gepreel & C. Wen. *Acta Biomater.* **2012**, 8, 1661-1669.
[92] P. F. Hsu & J. R. Howell. *Exp Heat Transfer.* **1992**, 5, 293-313.

[93] Q. Z. Chen, A. R. Boccaccini, H. B. Zhang, D. Z. Wang & M. J. Edirisinghe. *J Am Ceram Soc.* **2006**, 89, 1534-1539.
[94] I. K. Jun, Y. H. Koh, J. H. Song, S. H. Lee & H. E. Kim. *Mater Lett.* **2006**, 60, 2507-2510.
[95] T. Lehnert, H. Grimmer, P. Boni, M. Horisberger & R. Gotthardt. *Acta Mater.* **2000**, 48, 4065-4071.
[96] T. Lehnert, S. Tixier, B. Boni & R. Gotthardt. *Mat Sci Eng a-Struct.* **1999**, 273, 713-716.
[97] V. Gupta, A. D. Johnson & V. Martynov. *Pricm 4: Forth Pacific Rim International Conference on Advanced Materials and Processing, Vols I and Ii.* **2001**, 2347-2349.
[98] W. L. Benard, H. Kahn, A. H. Heuer & M. A. Huff. *J Microelectromech S.* **1998**, 7, 245-251.
[99] D. Xu, B. C. Cai, G. F. Ding, Y. Zhou, A. B. Yu, L. Wang & X. L. Zhao. *Electronics and Structures for Mems.* **1999**, 3891, 369-375.
[100] R. H. Wolf & A. H. Heuer. *J Microelectromech S.* **1995**, 4, 206-212.
[101] H. Kahn, M. A. Huff & A. H. Heuer. *J Micromech Microeng.* **1998**, 8, 213-221.
[102] Y. Q. Fu, W. M. Huang, H. J. Du, X. Huang, J. P. Tan & X. Y. Gao. *Surf Coat Tech.* **2001**, 145, 107-112.
[103] S. Miyazaki, M. Tomozawa & H. Y. Kim. *Actuator.* **2008**, 372-377.
[104] K. K. Ho & G. P. Carman. *Thin Solid Films.* **2000**, 370, 18-29.
[105] K. K. Ho, K. P. Mohanchandra & G. P. Carman. *Thin Solid Films.* **2002**, 413, 1-7.
[106] A. Ishida & V. Martynov. *Mrs Bull.* **2002**, 27, 111-114.
[107] J. L. He, K. W. Won & J. T. Chang. *Thin Solid Films.* **2000**, 359, 46-54.
[108] E. Baldwin, B. Thomas, J. W. Lee & A. Rabiei. *Surf Coat Tech.* **2005**, 200, 2571-2579.
[109] G. A. Shaw & W. C. Crone. *Mechanical Properties of Nanostructured Materials and Nanocomposites.* **2004**, 791, 215-220.
[110] G. A. Shaw, D. S. Stone, A. D. Johnson, A. B. Ellis & W. C. Crone. *Appl Phys Lett.* **2003**, 83, 257-259.
[111] R. Zarnetta, P. J. S. Buenconsejo, A. Savan, S. Thienhaus & A. Ludwig. *Intermetallics.* **2012**, 26, 98-109.
[112] H. Cho, H. Y. Kim & S. Miyazaki. *Sci Technol Adv Mat.* **2005**, 6, 678-683.
[113] X. G. Ma & K. Komvopoulos. *Appl Phys Lett.* **2003**, 83, 3773-3775.
[114] O. Adiguzel. *J Phys Conf Ser.* **2010**, 248.
[115] P. C. Su, C. C. Chao, J. H. Shim, R. Fasching & F. B. Prinz. *Nano Lett.* **2008**, 8, 2289-2292.
[116] A. Galtayries, R. Sporken, J. Riga, G. Blanchard & R. Caudano. *J Electron Spectrosc.* **1998**, 88, 951-956.
[117] I. Kosacki, T. Suzuki, V. Petrovsky & H. U. Anderson. *Solid State Ionics.* **2000**, 136, 1225-1233.
[118] S. deSouza, S. J. Visco & L. C. DeJonghe. *Solid State Ionics.* **1997**, 98, 57-61.
[119] W. Zhou, H. G. Shi, R. Ran, R. Cai, Z. P. Shao & W. Q. Jin. *J Power Sources.* **2008**, 184, 229-237.
[120] S. Heiroth, R. Ghisleni, T. Lippert, J. Michler & A. Wokaun. *Acta Mater.* **2011**, 59, 2330-2340.

[121] K. A. Tsoi, J. Schrooten, Y. J. Zheng & R. Stalmans. *Mat Sci Eng a-Struct.* **2004**, 368, 299-310.
[122] Y. Furuya, A. Sasaki & M. Taya. *Mater T Jim.* **1993**, 34, 224-227.
[123] M. Taya, Y. Furuya, Y. Yamada, R. Watanabe, S. Shibata & T. Mori. *Smart Materials.* **1993**, 1916, 373-383.
[124] A. Nespoli, S. Besseghini, S. Pittaccio, E. Villa & S. Viscuso. *Sensor Actuat a-Phys.* **2010**, 158, 149-160.
[125] R. J. Kane, W. M. Yue, J. J. Mason & R. K. Roeder. *J Mech Behav Biomed.* **2010**, 3, 504-511.
[126] N. N. Mahmud, S. K. Vajpai & K. Ameyama. *Mater Trans.* **2014**, 55, 1827-1833.
[127] H. B. Zhang & M. J. Edirisinghe. *J Am Ceram Soc.* **2006**, 89, 1870-1875.
[128] J. J. Li, X. L. Jiao & D. R. Chen. *J Disper Sci Technol.* **2007**, 28, 531-535.
[129] J. Chandradass & M. Balasubramanian. *Mater Manuf Process.* **2008**, 23, 159-162.
[130] H. Y. Liu, X. Q. Hou, X. Q. Wang, Y. L. Wang, D. Xu, C. Wang, W. Du, M. K. Lu & D. R. Yuan. *J Am Ceram Soc.* **2004**, 87, 2237-2241.
[131] N. Droushiotis, U. Doraswami, K. Kanawka, G. H. Kelsall & K. Li. *Solid State Ionics.* **2009**, 180, 1091-1099.
[132] C. C. Wei & K. Li. *Ind Eng Chem Res.* **2008**, 47, 1506-1512.
[133] L. H. Liu, X. Y. Tan & S. M. Liu. *J Am Ceram Soc.* **2006**, 89, 1156-1159.
[134] F. F. Lange. *J Mater Sci.* **1982**, 17, 225-234.
[135] F. F. Lange. *Am Ceram Soc Bull.* **1981**, 60, 852-852.
[136] J. S. Juan, M. L. No & C. A. Schuh. *J Mater Res.* **2011**, 26, 2461-2469.
[137] J. San Juan, M. L. No & C. A. Schuh. *Advanced Materials.* **2008**, 20, 272-+.
[138] J. S. Juan, M. L. No & C. A. Schuh. *Nat Nanotechnol.* **2009**, 4, 415-419.
[139] N. Ozdemir, I. Karaman, N. A. Mara, Y. I. Chumlyakov & H. E. Karaca. *Acta Mater.* **2012**, 60, 5670-5685.
[140] A. Lai, Z. H. Du, C. L. Gan & C. A. Schuh. *Science.* **2013**, 341, 1505-1508.
[141] H. Horikawa, S. Ichinose, K. Morii, S. Miyazaki & K. Otsuka. *Metall Trans A.* **1988**, 19, 915-923.
[142] X. Y. Zhang, L. C. Brinson & Q. P. Sun. *Smart Mater Struct.* **2000**, 9, 571-581.
[143] R. C. Garvie & M. V. Swain. *J Mater Sci.* **1985**, 20, 1193-1200.
[144] R. C. Garvie, R. H. Hannink & R. T. Pascoe. *Nature.* **1975**, 258, 703-704.
[145] P. M. Kelly & L. R. F. Rose. *Prog Mater Sci.* **2002**, 47, 463-557.
[146] K. Otsuka, Y. Xu & R. X. *Thermec'2003, Pts 1-5.* **2003**, 426-4, 251-258.
[147] X. M. Z. Zehui Du, Qing Liu,Alan Lai, Shahrouz Amini, Ali Miserez,Christopher A. Schuh, Chee Lip Gan. *Scripta Mater.* **2015**, 101, 40-43.
[148] Y. N. Liu & H. Yang. *Smart Mater Struct.* **2007**, 16, S22-S27.

Chapter 3

Experimental Methodology

This chapter presents the experimental techniques for the development and mechanical characterization of small volume shape memory ceramics. It involves the discussion on the methodology for the fabrication of bulk yttria stabilized zirconia (YSZ) and yttria-titania doped zirconia (YTDZ) ceramics, followed by the evaluation on the techniques for the micro-machining and mechanical tests of small volume ceramics. A few critical characterization techniques to study the microstructures and material compositions of the YSZ and YTDZ ceramics will also be elaborated.

3.1 Rationale for Experimental Design

The experiments were designed with the aim to prepare and characterize small volume shape memory zirconia ceramics. The experiments include two attempts in preparing the ceramics and the work flow is illustrated in Figure 3.1. The first attempt was to evaluate the shape memory effect in traditional yttria stabilized zirconia (YSZ) ceramics, but at small scale. The experimental procedure involves the following steps: fabricating bulk zirconia with conventional ceramic processing techniques, characterizing the YSZ ceramics to understand the microstructure and relevant composition properties, preparing small volume ceramics at microscale, and finally conducting mechanical tests on the small volume ceramics to explore the shape memory effect. Once the concept that small volume zirconia can demonstrate shape memory effect was proven, the material composition was modified, with the attempt to optimize the properties by developing single crystal shape memory ceramics. The preliminary work on exploring the suitable composition is discussed in detail in Appendix 9.1. A similar experimental procedure was employed until a suitable composition was obtained to achieve repeatable and reliable shape memory effect.

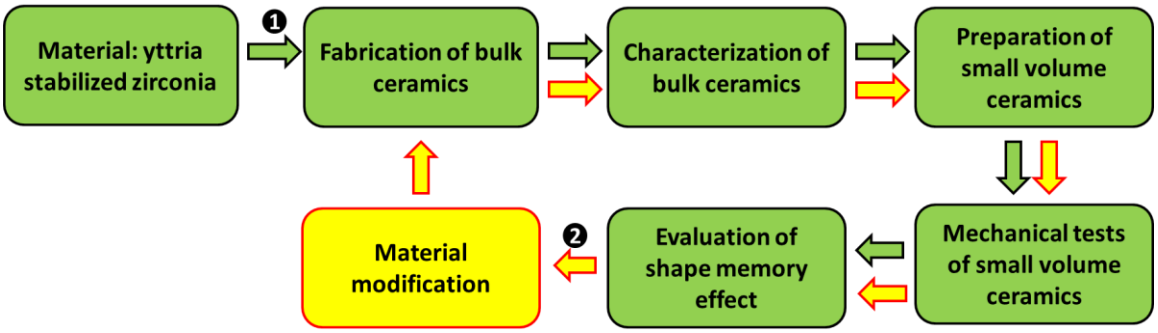

Figure 3.1 The experimental work flow on studying SMCs properties.

3.2 Fabrication of Bulk Ceramics

The bulk zirconia ceramics were fabricated with conventional "powder mixing" ceramic processing procedure and solid state sintering methods[1]. The synthesis procedure of bulk YSZ ceramics is shown in Figure 3.2. The starting powders were purchased from well-recognized powder fabrication companies according to numerous literatures. The

zirconia powders were purchased from Tosoh, Japan, who is well known for good quality of 3 mol% yttria doped zirconia (size = 40 nm, TZ-3Y grade) and pure zirconia (≥99%). The doping candidates of yttria (≥99.99%), titania (≥99%), magnesia (≥99.99%), ceria (≥99.9%) and niobium pentoxide (≥99.99%) were purchased from Sigma-Aldrich, USA. To prepare bulk YSZ ceramics, the ceramic powders were weighed and mixed according to molar formula of xY_2O_3-$(100-x)ZrO_2$. As 8mol% of yttria is enough to fully stabilize the zirconia into cubic phase[2], the doping concentration was controlled to be $x = 0 \sim 7$ with 0.005-0.01 as interval, by adding pure zirconia or yttria powders into the TZ-3Y powders. The powders were mixed with zirconia milling balls (with three diameters of 1 mm, 3 mm and 10 mm) and ethanol as milling medium, followed by horizontal ball milling for 24 hours to obtain a homogeneous powder mixture. After sieving out the milling balls, the mixture was dried at 80^{o}C for 48 hours to obtain dry powders. The powders were grinded and sieved several times to remove any agglomerates and obtain uniformly mixed nanosize powders. The powders were subsequently uniformly mixed with 0.35 wt% polyvinyl alcohol (PVA, Mw = 72k) as binder. The mixture was further pressed into pellets (weight = 1.5 g, green pellet diameter = 15mm) at 100 MP using a hydraulic presser. A cold isostatic press (CIP) was applied at 240 MPa for 3 minutes to increase the density of the green pellets.

The green pellets were pre-sintered to pyrolyze the PVA, in order to reduce the production of pores as a result of PVA decomposition during sintering. A second CIP step was conducted at 240 MPa for 3 minutes to further densify the ceramics. The pellets were then sintered in air at elevated temperatures of 1500 or 1700^{o}C (to explore the effect of sintering temperature) for 6 hours at a ramping rate of 5^{o}C/minute. Subsequently, the sintered pellets were ground to remove the surface layer with a thickness of 500 μm, followed by polishing with diamond slurry for 30 minutes. Finally, the polished pellets were hot etched at 1450^{o}C for 30 minutes. With the hot etching, the grain boundaries become visible at microscale but the grain size and morphology can be retained. The pellets were then coated with 15 nm of carbon to compensate charging to enable morphology imaging and further characterization in a scanning electron microscope.

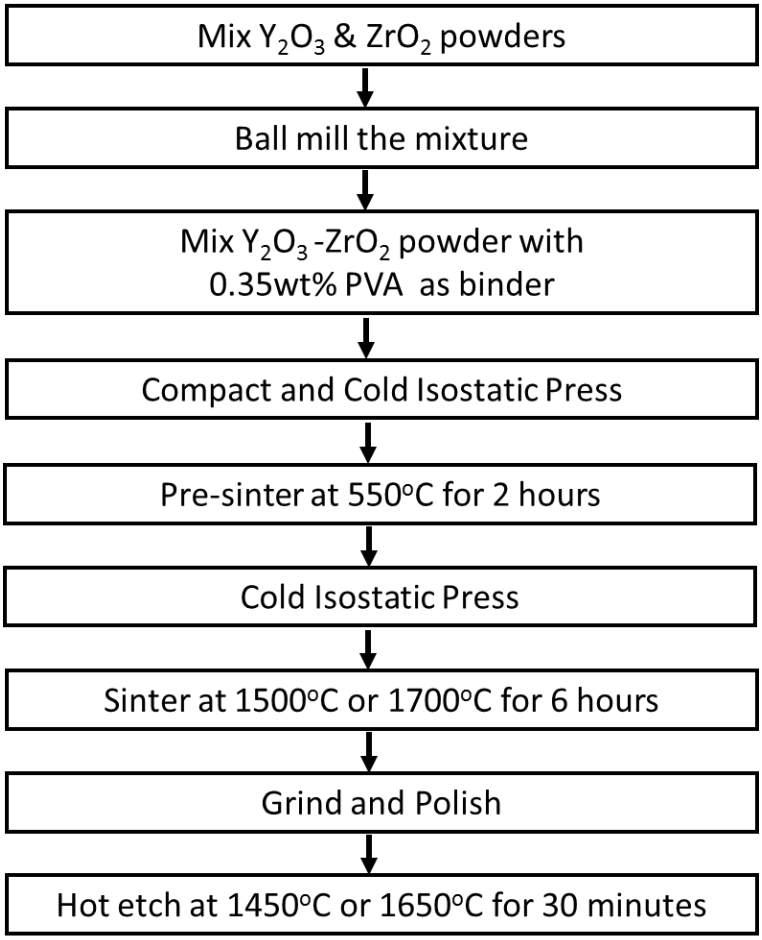

Figure 3.2 (a) Flow chart of the synthesis procedure for YSZ ceramics.

3.3 Characterization of Bulk Ceramics

The ceramics characterization involves the study of bulk ceramics in terms of microstructure, phase composition, phase transformation temperature, chemical composition distribution and crystal orientation with various scientific instruments.

3.3.1 Microstructure and grain size

The characterization of bulk ceramics starts with detailed microstructural analysis of the ceramic surface using field emission scanning electron microscopy (FESEM, JOEL 7600F). In high vacuum, the field emission of electrons takes place under a high electrical field and the contrast of work functions is displayed on the florescent screen,

showing the microstructure of samples. All the images were taken at a voltage of 5 kV and an emission current of 0.42 nA. The working distance was maintained at 5 mm and there is no tilting or rotation involved during the imaging. The magnification for imaging ranges from ×50 to ×20000 to view both the morphology and grain structure of the ceramics, as shown in Figure 3.3. The surface morphology can qualitatively show information on the existence of micro-cracks and grain boundaries, the range of grain size, grain shape and pore density. For pure zirconia ceramics shown in Figure 3.3, clear grains boundaries can be observed at a magnification higher than ×5000, which can be used to calculate the grain size distribution in subsequent section.

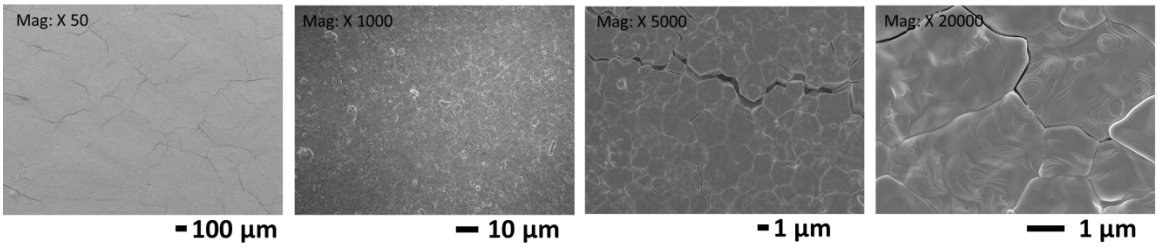

Figure 3.3 FESEM images for the surface morphology of pure zirconia ceramics at various magnifications.

The FESEM images were used for the grain size study with image analysis software (ImageJ, National Institutes of Health, West Bethesda, MD)[3]. Firstly, the grain boundaries on the FESEM image were manually highlighted to be recognized and processed by the software ImageJ. The contrast of the images was adjusted to differentiate the grain boundaries from other areas and the area within each boundary was measured and averaged, as seen in Figure 3.4. Finally the diameter was deduced from the area, assuming spherical grains, and the grain size distribution can be analysed.

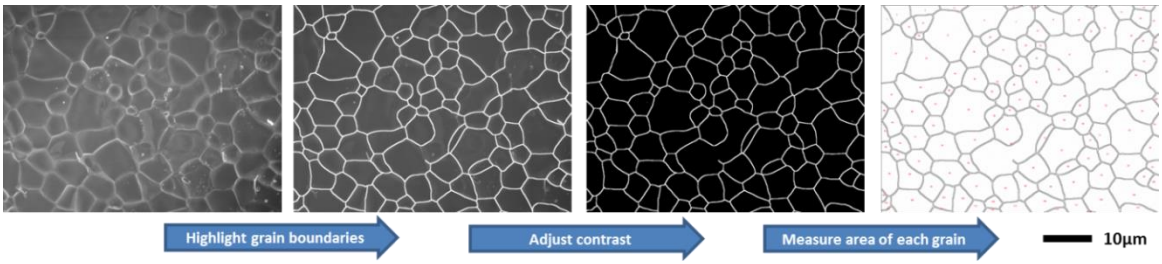

Figure 3.4 Measurement of grain size with ImageJ.

3.3.2 Phase composition

The phase composition of the bulk ceramics at room temperature was collected and analyzed by x-ray diffraction (XRD, D8, Bruker) with Cu Kα radiation. The finely focused monochromatic beam of X-rays (with wavelength λ=1.54 nm) bombarded towards the sample from an angle θ, and the reflected diffraction patterns were captured by the detector at an angle of 2θ. According to Bragg's Law,

$$n\lambda = 2dsin\theta \qquad \text{Equation 2}$$

where n is an integer and d is the d-spacing between two constructive crystal planes. Once Bragg's Law is satisfied at certain 2θ, constructive interference can be obtained and diffraction peaks with high intensity can be detected. According to the database for the positions of characteristic diffraction peaks of zirconia crystals, the measurements were performed at room temperature over two different 2θ ranges, 2θ = 25°-90° with step size of 0.2°/sec as shown in Figure 3.5.

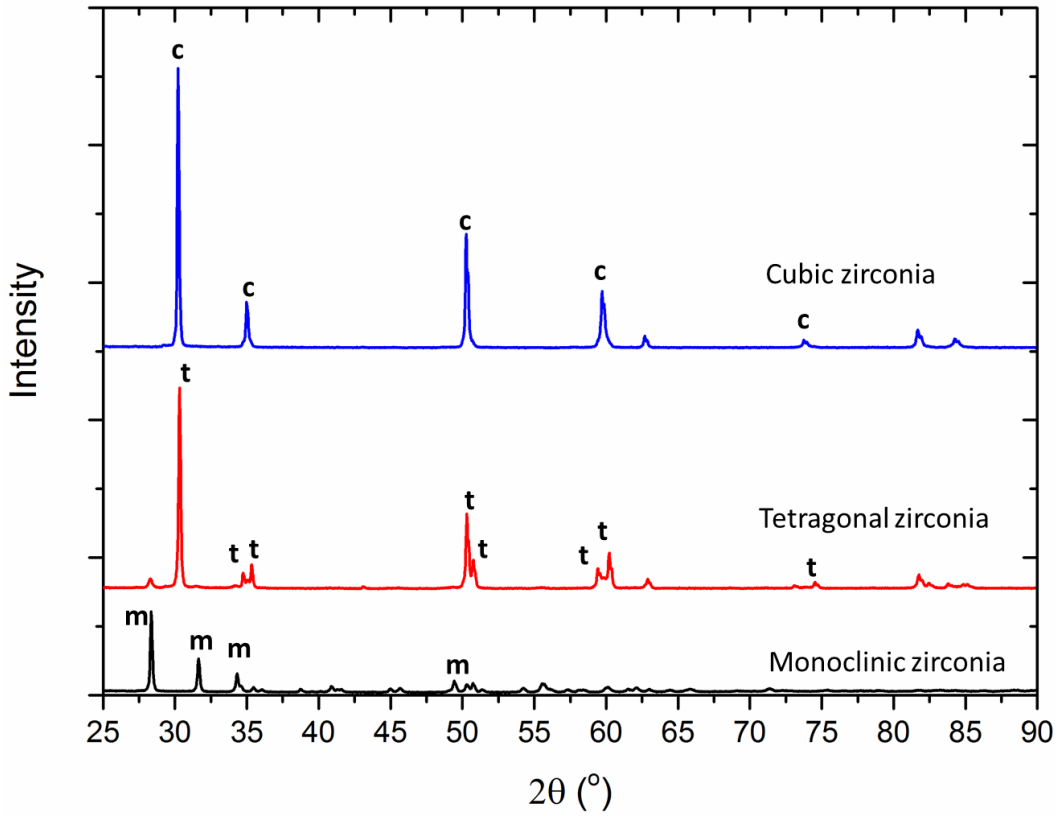

Figure 3.5 Typical XRD spectra of three phases of zirconia (cubic, tetragonal and monoclinic) and their characteristic peaks.

3.3.3 Martensitic transformation temperature

The martensitic transformation temperatures were obtained with differential scanning calorimetry (DSC). DSC is a thermo-analytical technique that can measure the variation of the amount of heat required to change the temperature, thus it can identify any crystal changes that absorb or emit heat at different temperatures. As reviewed in Chapter 2, the occurrence of the reversible martensitic transformation of zirconia is always accompanied by heat absorption and release, at temperatures between 25^{o}C and 1000^{o}C. Therefore, heat peaks are expected during martensitic transformation and the corresponding transformation temperatures can be obtained, as shown in Figure 3.6.

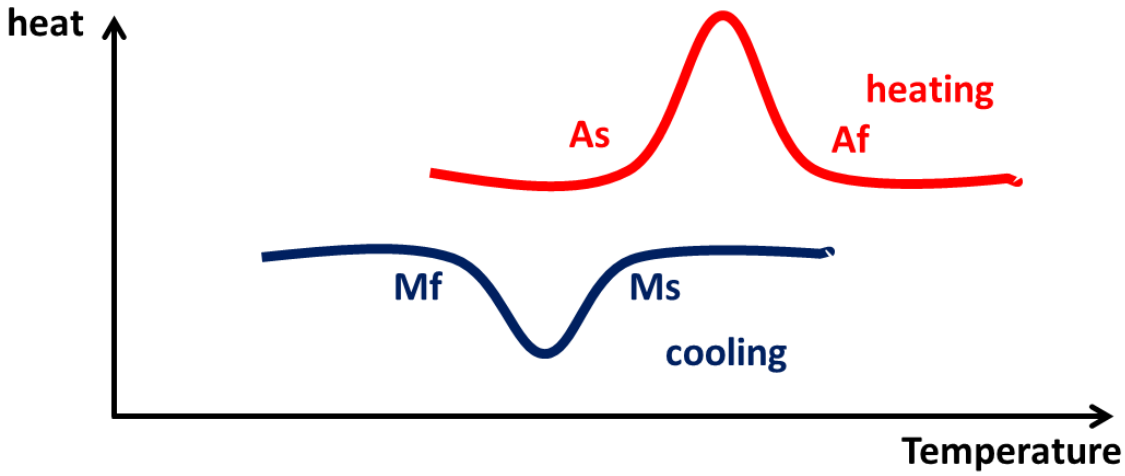

Figure 3.6 Typical DSC curves during the occurrence of martensitic transformation.

The martensitic transformations were therefore determined by heating the ceramics from 25^{o}C to 1000^{o}C in air with a ramping rate of 10^{o}C/min, followed by cooling to room temperature at the same rate. This method only works when the martensitic transformation occurs at large scale across the whole ceramic, with absorbed or released heat high enough to be detected by the calorimetry. For martensitic transformation of small volume ceramics at microscale or transformation temperature close to room temperature, DSC is not applicable as the accompanied heat is not differentiable from the background signal. A more detailed discussion on the characterization of martensitic transformation for both bulk and microscale zirconia ceramics will be presented in Chapter 4.

3.3.4 Chemical composition distribution at grain-scale

As the focus of our project is ceramics at small volume, the grain-scale chemical distribution instead of the gross ceramic composition is of higher importance, especially when the composition can determine the shape memory behavior, as reviewed in Chapter 2. The zoomed-in spatial chemical distribution at grain-scale was mapped and quantitatively analyzed with electron probe micro-analysis (EPMA, JXA-8500F, JEOL). EPMA is an analytical technique that uses focused electrons to produce characteristic x-rays from the samples within a small volume (typically a few microns). The characteristic x-rays with different wavelengths from different elements are detected and used to establish the elemental composition of the samples. The EMPA could provide grain-scale resolution in terms of chemical distribution. By combining with FESEM, the elemental mapping with EPMA can provide composition map of the ceramics at grain-scale, and the spot scan can give more accurate composition information at various positions of the ceramics. Elemental mapping was conducted for zirconium, yttrium, titanium and oxygen of the ceramics, with mapping area of 200 × 200 μm^2 that covers hundreds of grains. Due to the small spot size of EPMA, it can provide more accurate and reliable elemental information than EDX (Energy-dispersive X-ray spectroscopy). Here we illustrate one typical EPMA elemental mapping with an area of 30 × 40 μm^2, together with their corresponding FESEM and BSE maps, as shown in Figure 3.7. The EPMA map allows precise positioning of the scanning area, and we are able to match the grain morphology with the elemental map. Therefore with EPMA maps, we are able to confirm whether there is elemental segregation across grains or at grain boundaries. A more detailed discussion on the chemical distribution of zirconia ceramics will be presented in Chapter 4.

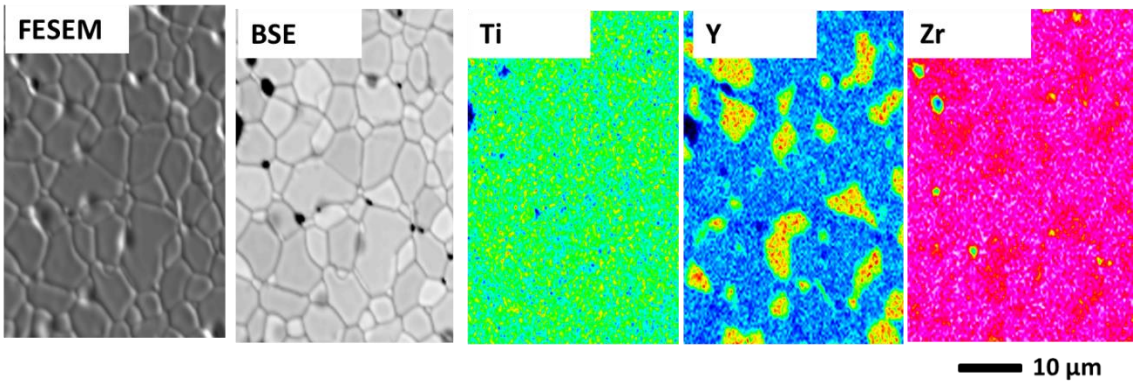

Figure 3.7 Typical EMPA elemental maps of yttria-titania doped zirconia, including the FESEM, BSE image, and the titanium, yttrium and titanium mapping. The map is coded in rainbow, with more reddish color represents higher concentration of element.

3.3 5 Crystal orientation

As reviewed in Chapter 2, crystal orientation is expected to affect the martensitic transformation behavior. The distribution of crystal orientation at grain-scale was mapped with electron backscattered diffraction (EBSD, Edax, USA). At a high voltage of 20 kV and a high current of 9.5 nA, the Kikuchi bands that form from the backscattered electrons in the FESEM chamber can be detected by the EBSD detector. The Kikuchi bands will not only provide information on crystal structure but also the crystal orientation. For zirconia ceramics, the obtained Kikuchi bands were indexed with monoclinic, tetragonal and cubic zirconia crystals, until a successful indexing is achieved with confidence index higher than 0.1. The crystal orientations of grains were obtained by mapping across the ceramic surface and indexing to a color map, with an exemplar mapping of tetragonal zirconia shown in Figure 3.8. Each color in the EBSD map represents a particular orientation in the reduced inverse pole figure of tetragonal zirconia. The variation of color indicates that tetragonal crystals in the polycrystalline ceramic are randomly distributed and there is no texture in terms of crystal orientation.

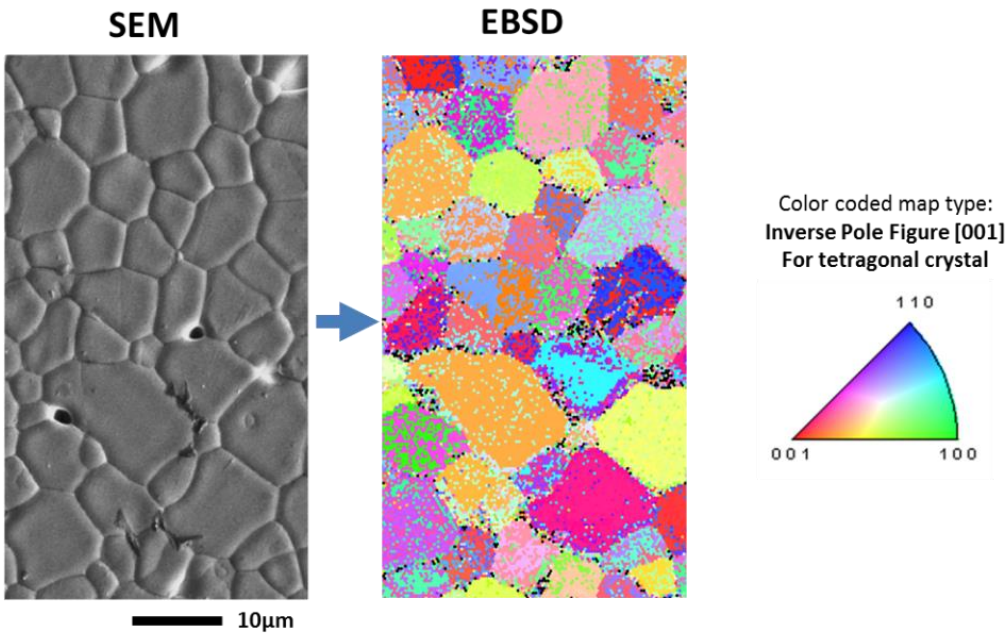

Figure 3.8 EBSD map of zirconia ceramics and the reduced inverse pole figure of tetragonal zirconia.

3.3.6 Crystal structure evolution and phase composition at grain-scale

As standard XRD and DSC only work for bulk ceramics at macro-scale and there is no resolution at grain-scale, the crystal structure of some individual grains was studied by synchrotron radiation scanning X-ray micro-diffraction (μXRD) technique[4] on beamline 12.3.2 at the Advanced Light Source, Berkeley, CA.

The configuration of the μXRD[4] is illustrated in Figure 3.9. The x-rays with high energy were provided by the synchrotron superconducting magnet source, which was focused by M1 toroidal mirror at the entrance of the experimental hutch. The beam window and roll slits were used to control the x-ray flux to be used for scanning. A monochromator is inserted to enable selection between white and monochromatic beam, providing a choice between a continued x-ray spectra with various wavelengths and a single x-ray wavelength. Subsequently, elliptically bent ultra-smooth mirrors are inserted to enable achromatic focusing, allowing submicron x-ray spot size on the sample with x-ray energy between 5 kV to 22 kV.

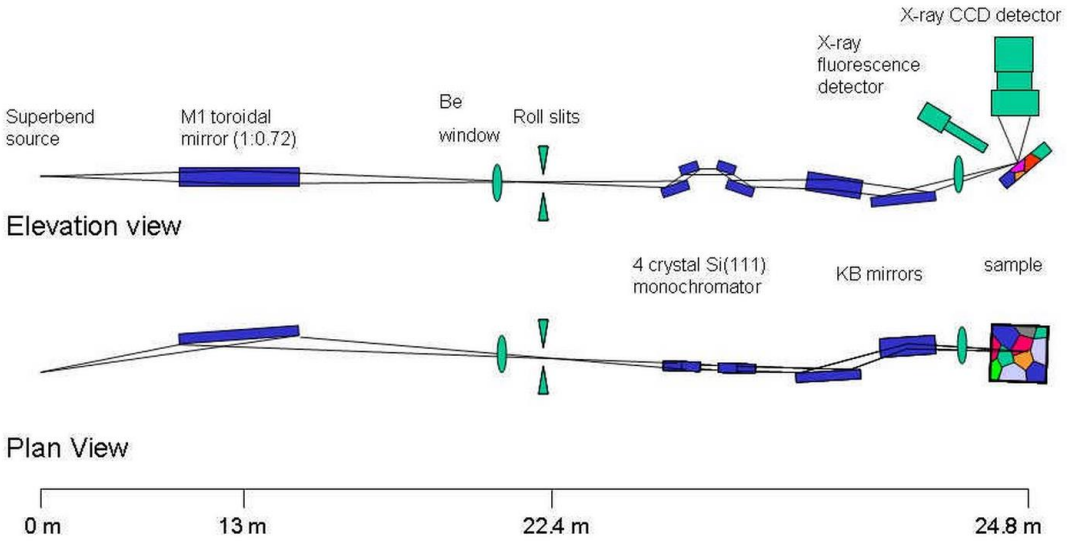

Figure 3.9 Schematic illustration of the beamline 12.3.2 at the Advanced Light Source, Berkeley, CA[4].

The samples are placed on a positioning stage with high precision, as shown in Figure 3.10(a). The x-ray fluorescence detector is used to precisely locate the microscale scanning area. The diffracted x-rays are collected using a DECTRIS Pilatus hybrid pixel array detector.

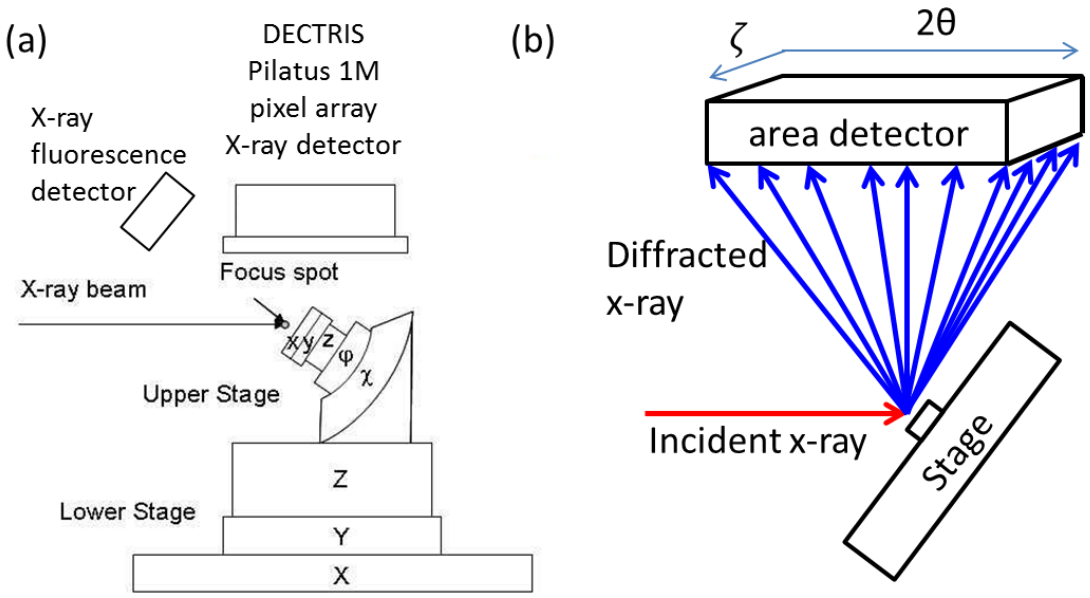

Figure 3.10 (a) Schematic diagram showing the relative positions of sample stage, florescence detector and x-ray detector. (b) The diffraction of x-ray and collection of signal with area detector.

Small volume zirconia grains were thinned using focus ion beam (FIB). The grains were then cut from the bulk ceramics and attached to a Mo or Si substrate using Omni-Probe™ in the FEI Nova 600i Nanolab FIB/SEM system. With the x-ray fluorescence detector, we were able to scan the substrate and locate the zirconia grain using fluorescence elemental mapping like Zr and Mo, as shown in Figure 3.11.

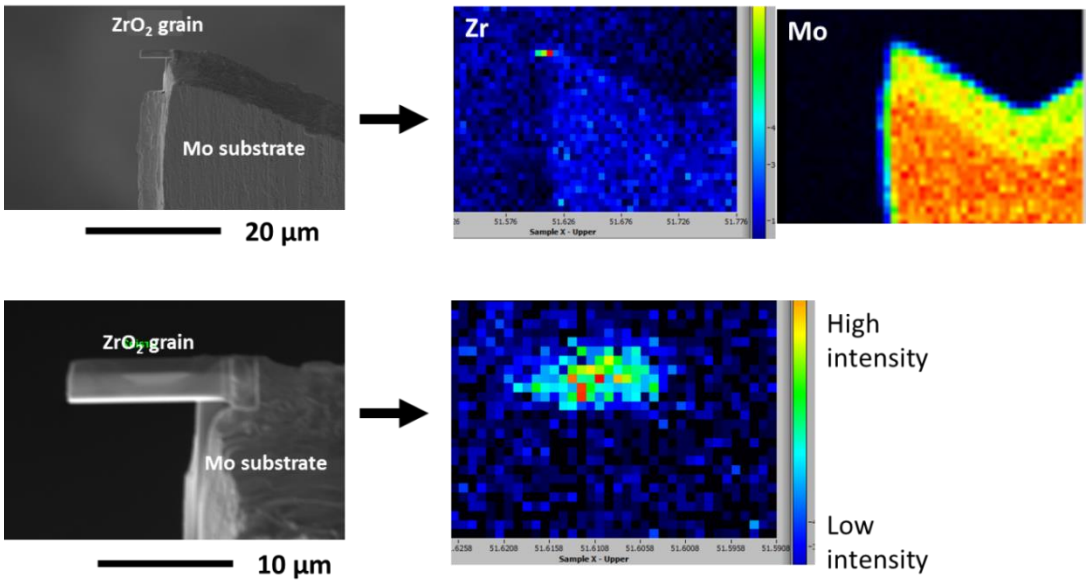

Figure 3.11 FESEM images and corresponding x-ray florescence mapping of zirconia grains that is attached to the Mo substrate.

With the florescence maps, we can select different positions on the sample and shin it with white beam x-ray. The area detector can collect x-ray signals diffracted within a large scattering area and the detector dimension can be interpreted as diffraction angles of 2θ and ζ, as shown in Figure 3.10(b). For a single crystal Si substrate, it can produce a 2D Laue diffraction pattern as shown in Figure 3.12(a), with two directions represented by 2θ and ζ. The white spots within the Laue diffraction pattern represent planes that produce constructive interference at various wavelengths that satisfy Bragg's Law. Multiple reflections can be satisfied at the same time due to the continuous spectra of white beam. The relative positions of the reflections are determined by the shape and orientation of the unit cell, and therefore can be used to analyze the crystal structure and orientation. The Laue diffraction pattern was analyzed using the XMAS (µXRD analysis

software) software package developed by scientist Nobumichi Tamura from Advanced Light Source, Berkeley, CA. A successful indexation of Si crystal is illustrated in Figure 3.12(b) using Si cubic crystal. The interfered plane for each peak can be clearly illustrated as well.

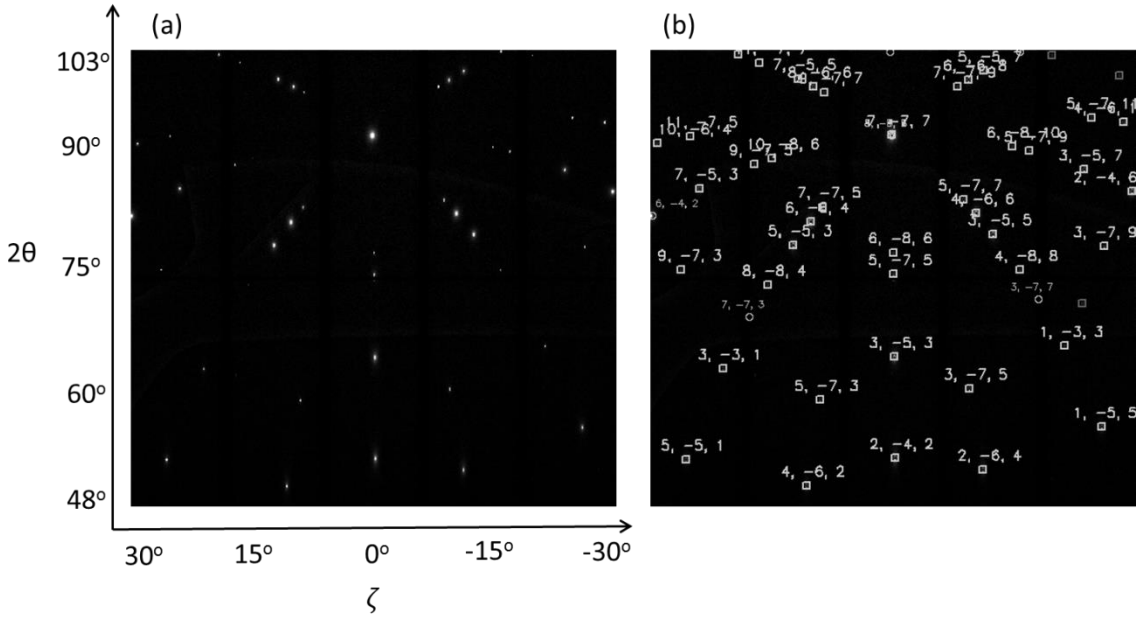

Figure 3.12 (a) Laue diffraction of single crystal Si substrate using area x-ray detector and (b) the indexed planes that produce constructive interference at white beam.

The sample stage of μXRD enables the installation of a heating stage that allows us to scan the zirconia grain at various temperatures from 25°C to 700°C. Therefore, we were able to study the martensitic transformation temperatures and crystal orientation evolution of microscale zirconia grains.

Some zirconia grains were characterized with transmission electron microscopy (TEM, Joel 2010F) and selected area diffraction (SEAD) to study the crystal structure and atomic arrangement.

3.4 Preparation of Small Volume Ceramics

The first step before milling the ceramics into small volume is to select the suitable grains to be machined into micro/nano-scale pillars. Prior to the selection, both the EBSD and EPMA maps need to be obtained and those with suitable compositions and

orientations were chosen. For YSZ ceramics where the grain size is much smaller than pillar dimensions, small tetragonal grains were selected with no information on crystal orientation. These grains were machined into microscale columnar pillars with focused ion beam milling system (FIB, FEI Nova 600i Nanolab), as shown in Figure 3.13. The pillar-shaped ceramics are very suitable for subsequent nanomechanical tests and stress/strain analysis.

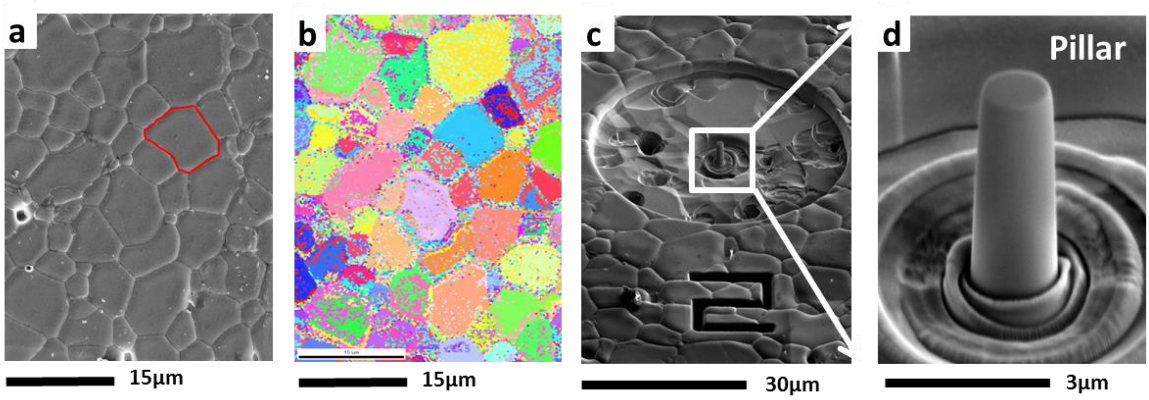

Figure 3.13 The preparation procedure for a pillar, including (a) select tetragonal grain, (b) obtain crystal orientation with EBSD, (c) and (d) mill the pillar on the selected grain.

The FIB is equipped with both electron beam and ion beam, enabling concurrently milling and imaging of materials in the chamber (Figure 3.14(a)). The stage was tilted 52^{o}C to align the surface of the ceramics with the ion gun, as shown in Figure 3.14(b). The pillar diameter is in the range of hundreds of nanometers to a few micrometers and the height is between 3 µm to 6 µm. Each pillar was machined in the center of a crater with a diameter of 40 µm and 2 µm in depth as indicated in Figure 3.14(b), to avoid possible contact of the surrounding matrix with the compression tip during subsequent mechanical tests.

The quality of pillar is highly dependent on the pre-set milling dimension, ion beam current and the properties of the ceramic materials. After a few trials and errors, we managed to establish an optimized milling procedure to micro-machine the ceramics into pillars with desired size and small tapping angle. Generally, it involves a three-step milling procedure that includes creating a large crater at 21 nA, milling to the desired size at 0.92 nA and final polishing to reduce tappering at 28 pA.

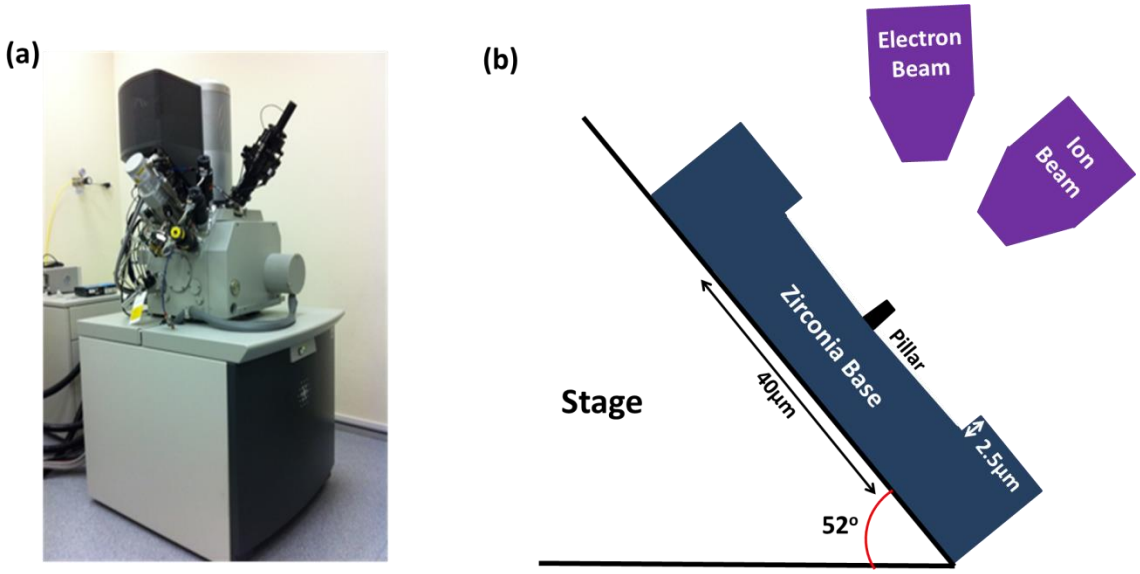

Figure 3.14 (a) Nova 600 Nanolab FIB system, (b) Schematic illustration of relative positions of ceramic sample, stage, ion beam and electron beam in Nova 600 Nanolab FIB system.

3.5 Mechanical Tests of Small Volume Ceramics

The nanomechanical characterization of pillars was performed with nanoindenter (TI950 and PI85, Hysitron. Inc. USA). For TI950, the nanoindenter can apply a load up to 30mN with precise position control. The pillars were carefully aligned by scanning the topography with a 20 μm spherical-conical diamond tip to enable uniaxial compression, as schematically illustrated in Figure 3.15(a). The indentation was controlled by load-control mode with a loading and unloading rate of 50 μN/sec. The data of load and concurrent indented depth was recorded in a real-time manner.

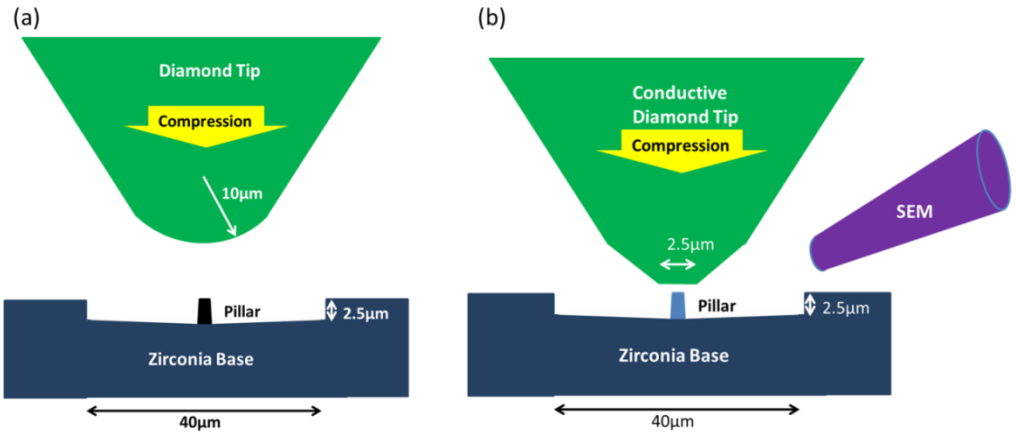

Figure 3.15 Schematic illustration of relative positions of ceramic pillar with respective to the indentation tip in (a) Hysitron TI950 nanoindenter and (b) Hysitron PI85 *in-situ* nanoindenter.

Unlike TI950, PI85 is an *in-situ* nanoindenter that can be installed inside a FESEM chamber, enabling the location and approach of the tip with FESEM imaging, as shown in Figure 3.15(b). The 2 µm flat-end diamond tip was carefully aligned by scanning electron microscopy to enable uniaxial compression, as shown in Figure 3.16.

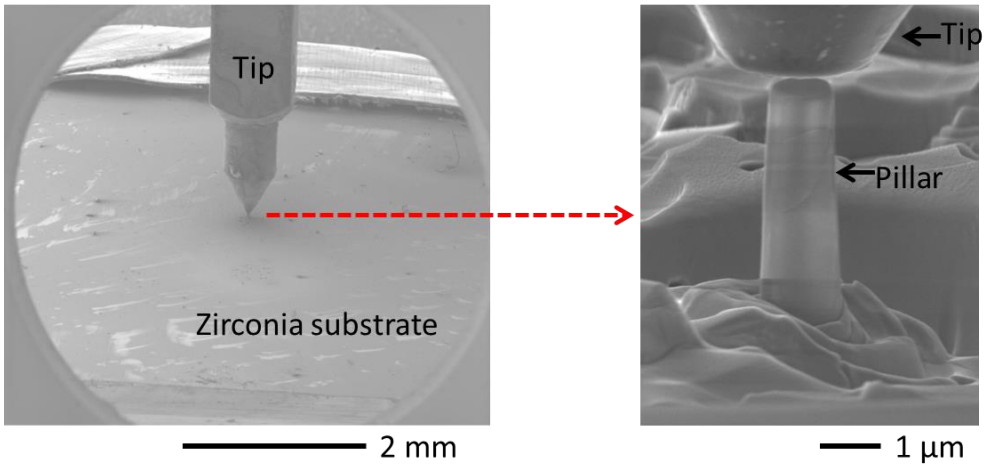

Figure 3.16 The 2 µm flat-end diamond tip with respect to zirconia sample during nanoindentation of PI85 *in-situ* nanoindenter, the sample was tilted to 20^{o}.

The *in-situ* indentation enables the real-time recording of pillar behaviors with SEM imaging simultaneously during compression, allowing us to have better control of tip-pillar alignment. More importantly, we can monitor the shape deformation during martensitic transformation and instantly differentiate phase transformation from plastic deformation or fracture.

3.6 Modification of the Ceramics

The motivation for material modification and the selection of suitable additives will be explained in Chapter 4 and 5. Titania has been used as an additive to the YSZ ceramics to promote the grain growth. After the modification, the new material system is with formula $x\mathrm{Y_2O_3}$-$y\mathrm{TiO_2}$-$(100\text{-}x\text{-}y)\mathrm{ZrO_2}$, with $x = 0 \sim 6$ and $y = 0 \sim 10$, by mixing pure $\mathrm{TiO_2}$ and $\mathrm{Y_2O_3}$ powders with TZ-3Y powders. A similar bulk ceramic fabrication procedure and characterization techniques were employed to understand the properties of

the modified ceramics. After characterization, grains with size larger than 8 μm were chosen and milled into single crystal pillars with diameter ~ 0.5 ~ 2.5 μm and height of 3 ~ 4 μm using FIB and finally compressed with nanoindenter. The compressed pillars were imaged with FESEM at a viewing angle of 52^o at different sample rotations to record the surface morphology.

3.7 Characterization on Shape Recovery

To investigate the thermally induced shape recovery capability of the ceramics, the compressed pillars were heated to temperatures of 300, 400, 450 and 550^oC for 30 minutes in air with a ramping rate of 5^oC/minute. After each heat treatment temperature, the ceramics were coated with 15 nm carbon again and imaged at the same conditions as the compressed pillars, to verify whether there is any change in pillar morphology. The heat-image process continues from low treatment temperature until a significant shape recovery is achieved, with clear surface morphology change. With such, we are able to roughly estimate the reverse martensitic transformation temperature for compressed pillars.

3.8 High Temperature Mechanical Tests

Part of the work on high temperature compression of pillars was conducted in MIT with nanoindenter (Hysitron TI950) equipped with a heating stage. The ceramic pillars and substrate were heated to the temperatures of 50^oC, 100^oC, 150^oC and 200^oC, and micro-compression were conducted at each temperature. Based on the shape recovery temperature determined in section 3.7, the ceramics were heat treated after each compression and the procedure is illustrated in Figure 3.17. The thermal vibration becomes significant at temperature higher than 150^oC, making it difficult to precisely locate the pillar and ensure uniaxial compression test. This is mainly due to the temperature gradient along the diamond tip and between tip and pillar. As only the ceramic samples were heated in TI950, the diamond tip temperature keeps changing

during the approach and indenting process, and large temperature gradient exist along the tip, making the thermal vibration much more significant at higher temperature.

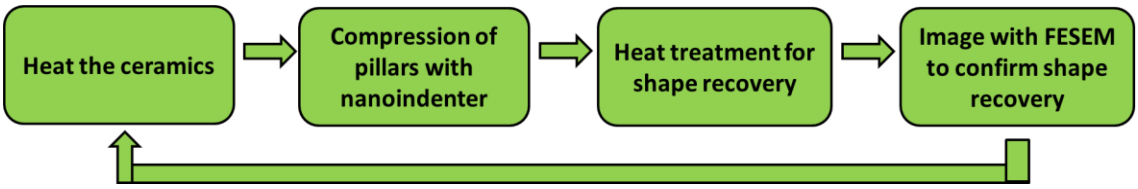

Figure 3.17 Schematic illustration of experimental procedure for high temperature compression of pillars.

Subsequently, we used Hysitron PI87 *in-situ* nanoindenter equipped with a heating stage to conduct high temperature nanoindentation. In this case, heating blocks were attached to both the sample stage and the tip to enable spontaneous heating and minimize thermal vibration. Similar to PI85, PI 87 indenter was installed inside a FESEM chamber and the FESEM was used to locate the pillar and align the tip. The real-time monitoring of tip and sample ensures uniaxial compression test all the time. With PI87, the pillars were heated to 400^{o}C and compressed to induced martensitic transformation and shape deformation, followed by *in-situ* heating to 650^{o}C to achieve reverse martensitic transformation temperature to enable *in-situ* shape recovery. The pillars were maintained at 650^{o}C and compressed again.

3.9 Overview of Methodology

The methodology designed for the study of small volume shape memory ceramics includes the fabrication and characterization of bulk ceramics, machining of small volume ceramics and mechanical tests for shape memory effect. The fabrication of bulk ceramics using powders as starting materials was done with a conventional approach. The characterization techniques were employed with the aim to learn the microstructure, phase composition and martensitic transformation of the ceramics at both bulk scale and microscale. The machining of small volume ceramics with precise shape control can be achieved effectively with a focused ion beam. The compressive mechanical tests for microscale ceramics can be carried out precisely with a nanoindenter, which provides

accurate load and displacement control to apply compressive load within 30 mN, high enough to reach the transformation stress for shape memory ceramics. High temperature nanoindentations were conducted as well to explore the working temperature of zirconia as a shape memory material.

Reference:

[1] T. H. Yeh, G. E. Kusuma, M. B. Suresh & C. C. Chou. *Mater Res Bull*. **2010**, 45, 318-323.
[2] K. Matsui, H. Yoshida & Y. Ikuhara. *Acta Mater*. **2008**, 56, 1315-1325.
[3] C. Igathinathane, L. O. Pordesimo & W. D. Batchelor. *Food Res Int.* **2009**, 42, 76-84.
[4] A. S. Budiman, N. Li, Q. Wei, J. K. Baldwin, J. Xiong, H. Luo, D. Trugman, Q. X. Jia, N. Tamura, M. Kunz, K. Chen & A. Misra. *Thin Solid Films.* **2011**, 519, 4137-4143.

Chapter 4

Ceramic Characterization*

This chapter discusses the characterization on the morphology and phase composition of yttria stabilized zirconia (YSZ) ceramics and the modified yttria-titania doped zirconia (YTDZ) ceramics. The effect of titania dopant on the ceramics was systematically evaluated, with the aim to obtain ceramics that have the suitable phase and grain size to develop single crystal shape memory ceramics at small volume.

*The content of this chapter was published in article:

Xiao Mei Zeng, Zehui Du, Christopher A Schuh, Nobumichi Tamura, Chee Lip Gan, Microstructure, Crystallization and Shape Memory Behavior of Titania and Yttria doped Zirconia. Journal of European Ceramic Society, 36, I5, 1277–1283, 2016

4.1 Introduction

Shape memory effect in zirconia with significant shape deformation can only be achieved by using tetragonal as parent phase, which can be transformed to monoclinic phase through stress-induced martensitic transformation during mechanical test. The phase composition is therefore the most critical property that needs to be addressed. As discussed in Chapter 2, the grain boundaries play an important role in nucleating cracks before martensitic transformation can be triggered. The grain size is therefore another important parameter that affects the shape memory effect. Hence, the characterization on bulk zirconia was focused on its phase composition and morphology, both as bulk and at microscale.

4.2 Yttria-Stabilized Zirconia (YSZ) Ceramics

Though the stress-induced martensitic transformation in YSZ has been well-studied, as reviewed in Chapter 2, there has been no report discussing on its shape memory effect. In the aim to find the most suitable composition for shape memory effect, our first attempt was to prepare a series of zirconia with various yttria concentrations and conduct a systematic characterization of the key properties that affect the martensitic transformation: namely, the phase composition and ceramic morphology.

4.2.1 Phase composition of YSZ

To investigate the phase composition of YSZ with different yttria concentrations, XRD characterizations were conducted and the spectrums are illustrated in Figure 4.1(a). The spectrum indicates that the YSZ ceramics are composed of monoclinic, tetragonal and cubic phases of zirconia, and no other crystals are formed. As shown in Figure 4.1(a), monoclinic $(11\bar{1})$ and (111) peaks can be resolved from cubic/tetragonal (111) peak with 2θ = 20-90° scan; whereas cubic (400) peak can be resolved from tetragonal (400) and (004) peaks with 2θ = 70-76° scan. The weight fraction of each phase present in the

YSZ ceramics can be quantified using the relative intensities of the diffraction peaks[1, 2]. The weight fraction of the monoclinic phase, X_m can be calculated with Equation[3]:

$$X_m = \frac{I(11\bar{1})_m + I(111)_m}{I(11\bar{1})_m + I(111)_m + I(111)_{t/c}} \qquad \text{Equation 3}$$

where I $(111)_m$ and I$(11\bar{1})_m$ are the integrated intensity from the monoclinic (111) and $(11\bar{1})$ peaks, respectively and I $(111)_{t/c}$ is the integrated intensity from the tetragonal/cubic (111) peak.

The weight fraction of the cubic phase and tetragonal phase, X_c, X_t can be calculated using Equation 4 and 5, respectively[3]:

$$X_c = \frac{I(400)_c}{I(004)_t + I(400)_t + I(400)_c}(1 - X_m) \qquad \text{Equation 4}$$

$$X_t = 1 - X_m - X_c \qquad \text{Equation 5}$$

where I$(400)_c$ is the integrated intensity from the cubic (400) peak, I$(400)_t$ and I$(004)_t$ are the integrated intensity from the tetragonal (400) and (004) peak, respectively.

The calculated weight fractions of monoclinic/tetragonal/cubic phase of YSZ ceramics as a function of yttria content are shown in Figure 4.1(b). It is indicated that the ceramics are dominated by monoclinic phase with yttria ≤ 2 mol%, implying that no tetragonal phase could be stabilized to room temperature. The tetragonal phase started to appear at 2.5 mol% and dramatically increases to a maximum of 80wt% at 3 mol% of yttria, followed by a gradual decrease to around 20 wt% when yttria content is 7 mol%. The cubic phase can be observed at 3 mol% yttria and it gradually increases at a steady rate to 82 wt% for 7 mol% of yttria, which is consistent with literatures stating that 8 mol% yttria doped ZrO_2 is 100% cubic phase[4,5].

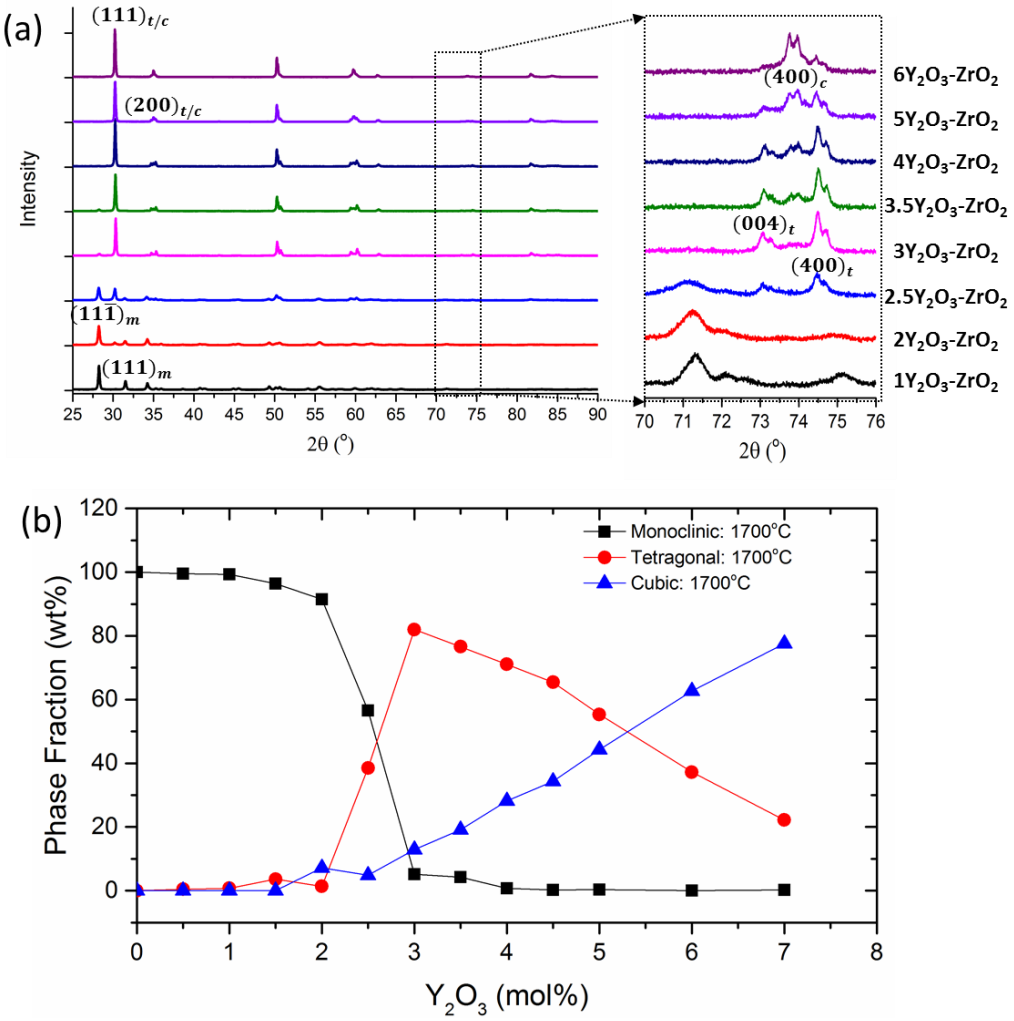

Figure 4.1 (a) The XRD spectrum of YSZ ceramics with 0 ~6 mol% of yttria sintered at 1700°C at a scan range of 25°-90° and a high resolution scan at 2θ = 70-76°. (b) The calculated weight fraction of monoclinic, tetragonal and cubic phase of YSZ ceramics sintered at 1700°C.

4.2.2 Ceramic morphology of YSZ

The ceramic microstructures were examined with FESEM. As zirconia with yttria between 2.5 and 5 mol% contains significant amount of tetragonal phase, here we only show three compositions in Figure 4.2 with representative morphologies of tetragonal zirconia. The surface after hot-etching is found relatively flat and grains are dense and crack-free. An increase of annealing temperature from 1500°C to 1700°C could coarsen the grains but the grain size remains mostly at submicron scale. Typical YSZ generally

has submicron grains[6], mainly due to the large ionic radius of yttrium. The low diffusion rate of yttrium in zirconium matrix results in a low grain growth rate.

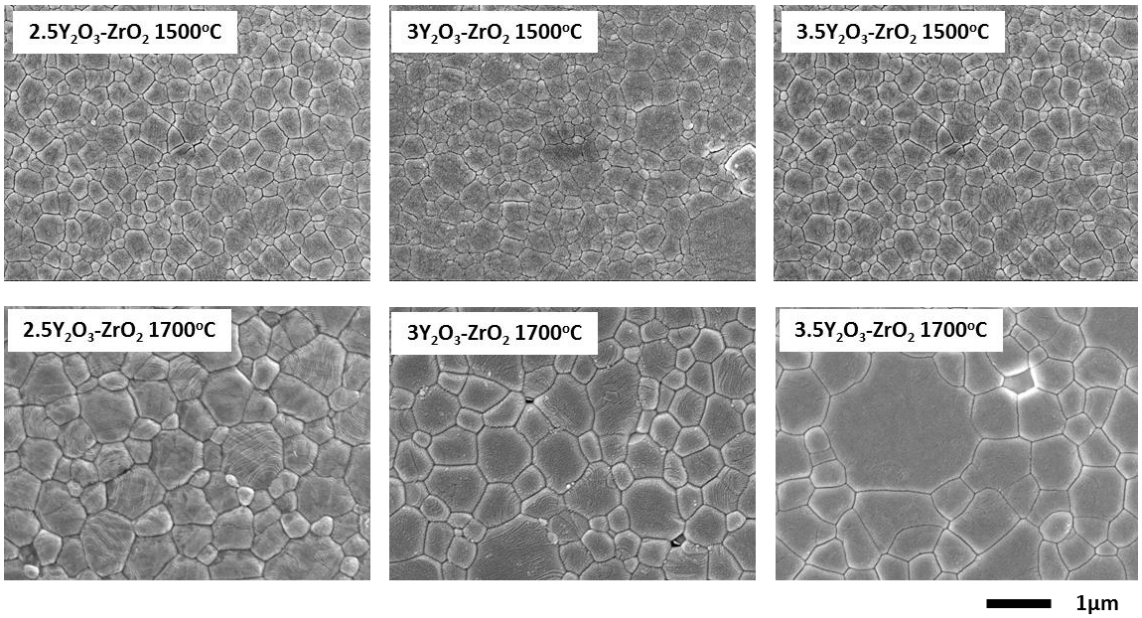

Figure 4.2 FESEM images of YSZ ceramics with 2.5mol%, 3mol% and 3.5mol% yttria at sintering temperatures of 1500°C and 1700°C.

4.3 Motivation for System Modification

The submicron grains of YSZ are much smaller than the typical pillar size (a few micrometers), meaning that the small volume pillar we propose to fabricate will contain many small grains and grain boundaries are inevitable. Though the high surface-to-volume ratio of the pillar could help release the concentrated stress during deformation, the possibility of cracking due to grain boundaries could still suppress the martensitic transformation and make the shape memory effect unreliable and unrepeatable. To explore the shape memory effect of conventional YSZ, we need to either prepare commensurately much smaller sample in submicron scale size or increase the YSZ grain size from submicron to micron scale without suppressing the martensitic transformation behavior. As preparing submicron pillars with good shape control using FIB was found very challenging and time consuming, here we employ the alternative approach by exploring methods to increase the grain size of YSZ to a few microns.

In addition to the effect of sintering temperature as observed in Figure 4.2, it was found that the grain growth of zirconia can also be controlled by the dopant material[7]. Some literatures have reported that by sintering at very high temperatures of around 2500^{o}C (skull sintering), very large grains can be obtained[8] but sophisticated furnace is required. Others discovered that by doping with some additives such as MgO, CeO_2, Nb_2O_5, or TiO_2, the grain size can also be significantly increased when sintering at much lower temperatures[9-11]. Here we employ the second approach of introducing extra doping additives as there are lower requirements on experimental set-up and it is a more energy-saving process for future real-life applications. Four candidates of MgO, Nb_2O_5, CeO_2 and TiO_2 were explored and TiO_2 was found to be the most suitable dopant. MgO helped to promote the grain growth significantly but it further stabilized the tetragonal phase into cubic phase, making the material not useful for shape memory effect. When Nb_2O_5 was introduced into YSZ, the ceramic grew in a way that it crushed into particles during sintering, making it not suitable for fabricating bulk ceramics. CeO_2 was found not suitable either as it evaporated very fast at 1700^{o}C, making it difficult to control the doping concentration. By adding 5 mol% TiO_2 into YSZ, the oxide remained very stable at high sintering temperatures. We discovered that not only the grains were grown much larger, but also the tetragonal phase was retained. The modified YSZ ceramics with titania are called yttria-titania doped zirconia (YTDZ) ceramics.

4.4 Yttria-Titania Doped Zirconia (YTDZ)

With the preliminary results and information from literature work[12], we fabricated YTDZ ternary system with varied concentrations of both dopants, and systematically characterized the phase composition, ceramic morphology and spatial chemical distribution. The YTDZ ceramics were compared to the YSZ binary system and the effect of titania doping was evaluated.

4.4.1 Ceramic morphology of YTDZ

To have a full understanding of the effect of titania doping on the YTDZ ceramics as well as the mutual effect between titania and yttria, we varied the titania concentration from 0 to 10 mol% and yttria concentration from 2 to 4 mol%. The representative microstructures of xY_2O_3-$yTiO_2$-ZrO_2 are shown in Figure 4.3.

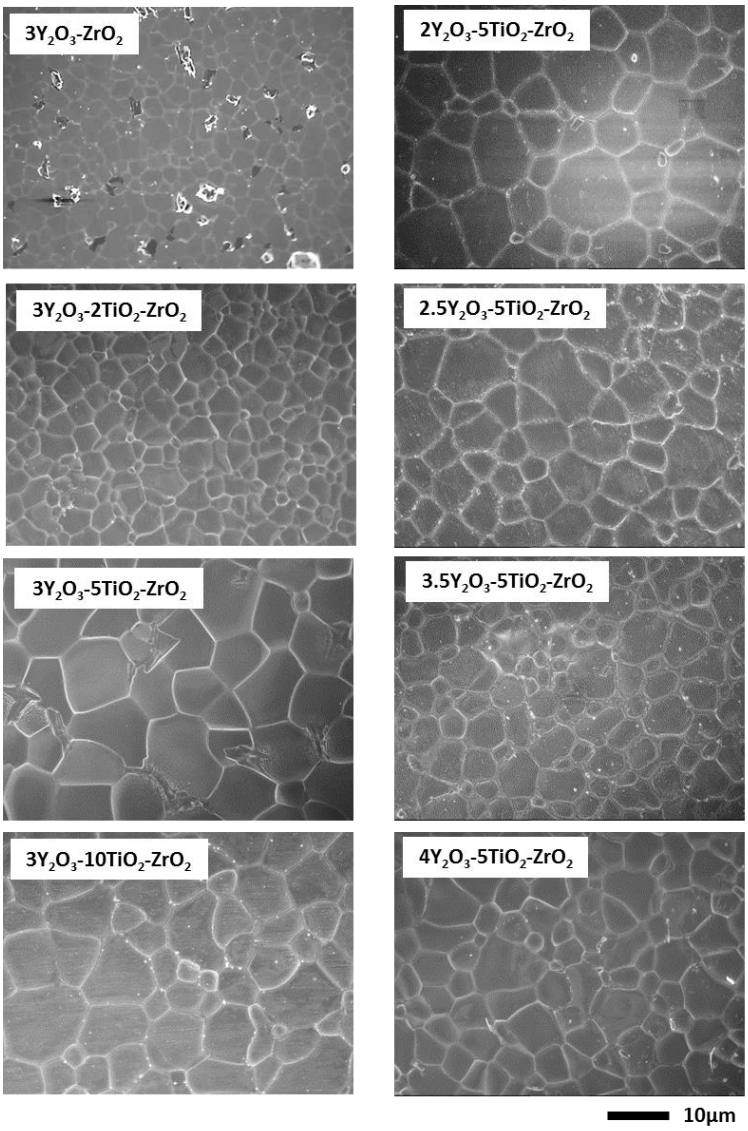

Figure 4.3 The microstructure of YTDZ with different concentration of titania and yttria.

The hot-etching process enables us to observe very clear grain boundaries and the ceramics are very dense with no visible pores. By comparing the SEM images of YSZ and YTSZ ceramics, it seems that titania could significantly affect the grain size, whereas the effect of yttria is less obvious. With the introduction of a small amount of titania, the grain size is increased from submicron to a few microns. The microscale grains would

enable us to fabricate single crystal pillars on the ceramics without grain boundaries. The single crystal structure will not only improve the mechanical performance of the pillars but also make it possible for the study of the role of crystal orientation on the shape memory effect in YTDZ ceramics.

The measured grain sizes of $x$$Y_2O_3-5TiO_2$-$ZrO_2$ ternary system as well as the $x$$Y_2O_3$-$ZrO_2$ binary system are shown in Figure 4.4(a). Comparing the two systems of YSZ (black dots) and YTSZ (blue dots), by adding 5 mol% TiO_2, the grain size of $x$$Y_2O_3-5TiO_2$-$ZrO_2$ system is significantly increased, from an average of 0.5μm for 2 to 4 mol% of Y_2O_3 to 3.1 μm at the same sintering temperature. Compared to the study in literature of 10 mol% TiO_2 sintered at 1400^oC[13], we found that 5 mol% of TiO_2 works similarly in promoting grain growth at a higher temperature of 1700^oC, but did not react with ZrO_2 to form the undesired $ZrTiO_4$ compounds with ZrO_2. Figure 4.4(a) also shows the effect of Y_2O_3 on the grain growth in the Y_2O_3-ZrO_2 binary system. Though the phase changes with Y_2O_3 concentration, the grain size remains relatively constant in the range of 0.4 - 0.5 μm for ceramics sintered at 1500^oC. An increase in sintering temperature (red dots) can help the grains to grow up to 0.55 μm, as also suggested in Figure 4.2, but the effect is much less significant as compared to TiO_2.

To get a more quantitative understanding of the TiO_2 effect on the grain growth of the ceramics, the average grain size as a function of TiO_2 concentration is plotted in Figure 4.4(b). By varying the TiO_2 concentration while maintaining the Y_2O_3 content, the grain size increases linearly to 4 μm with TiO_2 for doping up to 5mol%. This observation complies with literature that TiO_2 is a grain growth promoter in YSZ system[13,14], as it can improve the growth kinetics during sintering. The grain size remains relative constant with further doping of TiO_2, most probably because the TiO_2 saturates in the Y_2O_3-TiO_2-ZrO_2 solid solution before reaching 10 mol%, since the solubility of TiO_2 in Y-TZP is expected to be lower than 13 mol% at 1700^oC[15,16].

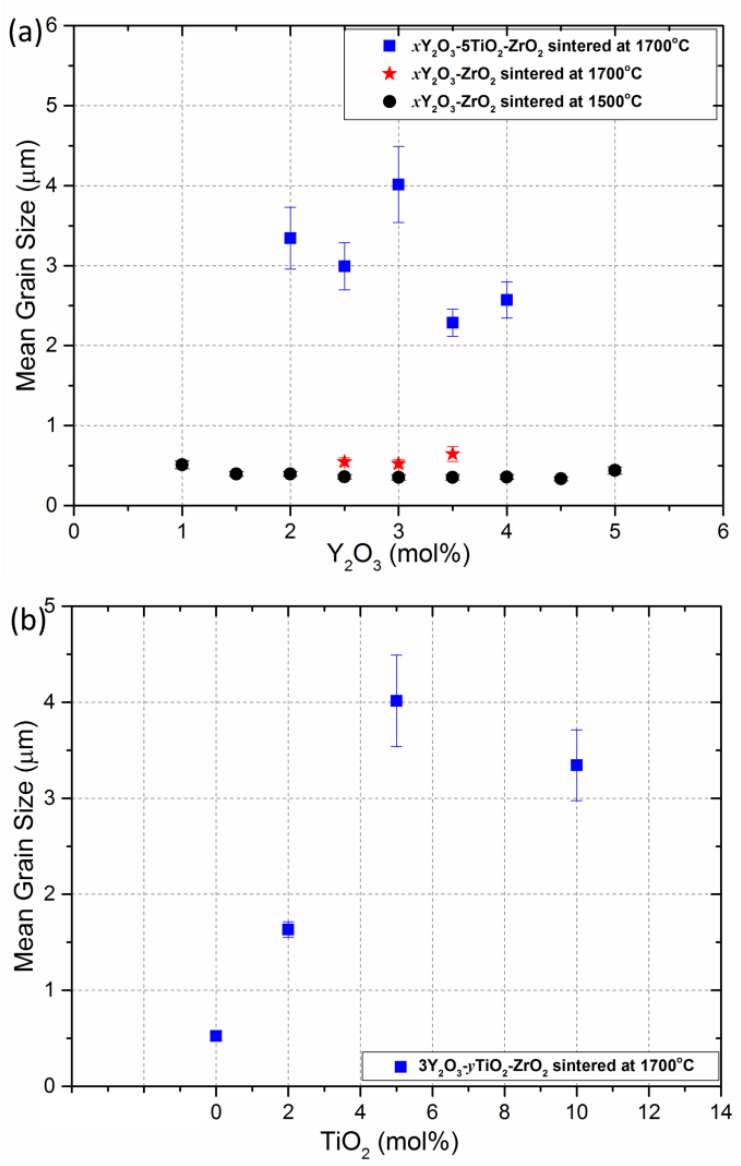

Figure 4.4 Average grain size of (a) Y_2O_3-ZrO_2 and xY_2O_3-5TiO_2-ZrO_2 doped with various amount of Y_2O_3, sintered at both 1500°C and 1700°C. (b) $3Y_2O_3$-$yTiO_2$-ZrO_2 with different amount of TiO_2 and sintered at 1700°C.

4.4.2 Phase composition of YTDZ

Similar to YSZ system, YTDZ system was characterized with XRD, with a scanning range of 2θ = 25-90° and a fine scanning with 2θ = 70-76°. The spectrums for xY_2O_3-5TiO_2-ZrO_2 with x varying from 2 to 4 mol% are shown in Figure 4.5. All the

characteristic peaks for monoclinic, tetragonal and cubic are observed in these compositions, similar to what was presented in Figure 4.1.

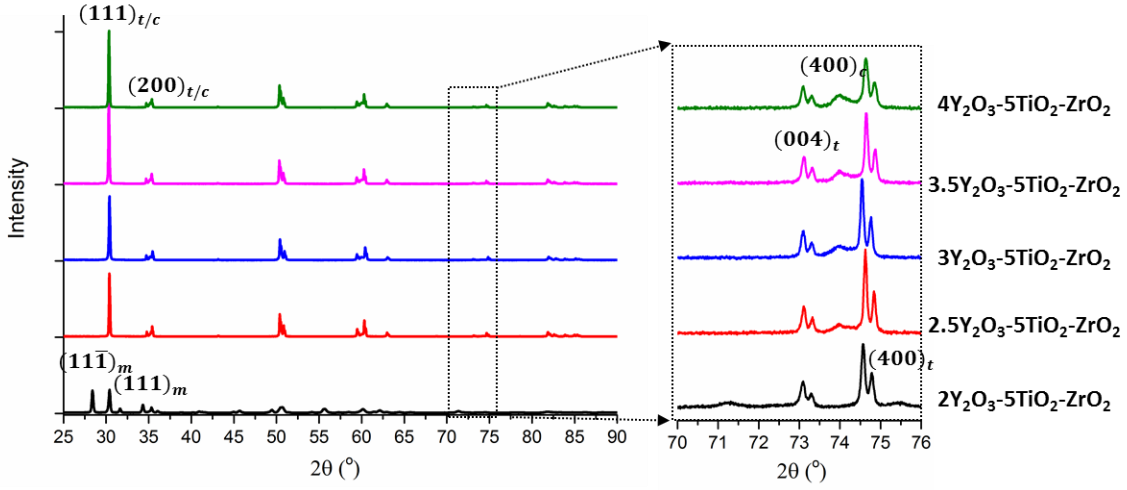

Figure 4.5 XRD spectrum for ternary xY_2O_3-$5TiO_2$-ZrO_2 system.

Similar analysis of the weight fraction for each phase was conducted according to Equations 3-5, as shown in Figure 4.6. The results have revealed that by alloying the binary system with a small amount of TiO_2, the phase composition is slightly altered.

TiO_2 doping is found to be very effective in stabilizing the tetragonal phase and suppressing the formation of cubic phase. By adding 5 mol% of TiO_2 into the Y_2O_3-ZrO_2 ceramics, the fraction of tetragonal phase significantly increases. According to Figure 4.6, the maximum fraction of 92 wt% of tetragonal phase can be obtained at $2.5Y_2O_3$-$5TiO_2$-ZrO_2. When the Y_2O_3 concentration increases to 3-4 mol%, the weight fraction of tetragonal phase remains above 85 wt% and the cubic phase is only ~10-15 wt%. Since Y_2O_3-$5TiO_2$-ZrO_2 ternary system consists of higher amount of tetragonal phase over a larger range of Y_2O_3 concentration, it can be a promising candidate as a shape memory ceramics.

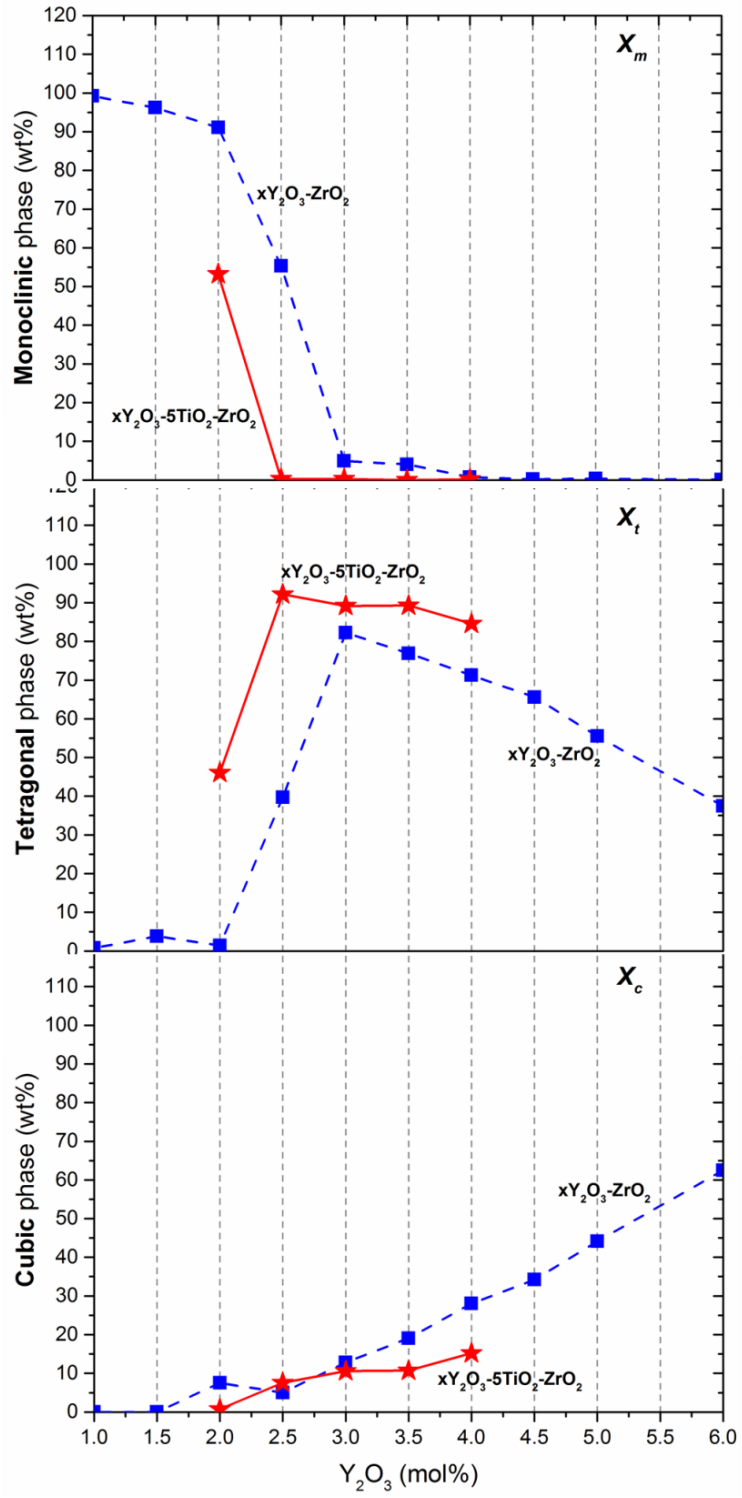

Figure 4.6 The calculated weight fraction (wt%) of monoclinic, tetragonal and cubic phases of YTDZ system and its comparison with YSZ system.

4.4.3 Lattice parameter of YTDZ

The lattice constants of both YSZ and YTDZ systems were obtained according to the precise position of some characteristic peaks in the XRD spectrum. The calculated lattice parameters of tetragonal and cubic phases are shown in Figure 4.7(a). It is worth noting that for both tetragonal and cubic phases, the effect of Y_2O_3 doping on lattice constants of zirconia is negligible. This can be attributed to the segregation of yttria in the ceramics, as will be presented and discussed in subsequent sections.

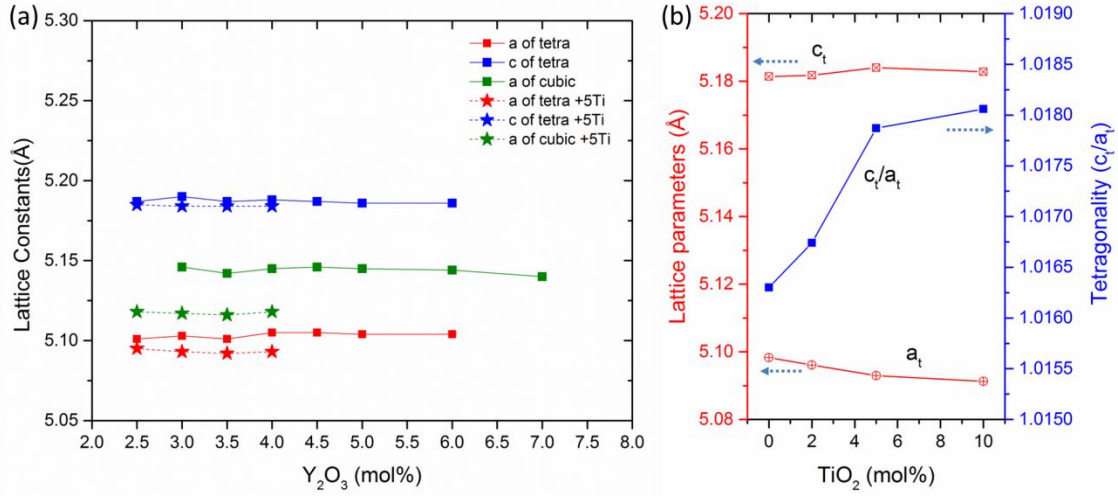

Figure 4.7 (a) Lattice parameters of tetragonal and cubic phases for both YSZ and YTDZ systems. (b) Lattice constants and tetragonality of the tetragonal phase in Y_2O_3-TiO_2-ZrO_2 as a function of TiO_2 concentration.

For YSZ ceramics, the lattice constants are a_t = 5.103±0.002 Å, c_t = 5.187±0.002 Å for tetragonal phase and a_c = 5.145±0.003 Å for cubic phase. These lattice constants are in good agreement with the tetragonal $2Y_2O_3$-ZrO_2 ceramics reported in literature (a = 5.1003 Å, c = 5.1866 Å)[17,18] as well as theoretically calculated data in pure zirconia (a = 5.105 Å, c = 5.20 Å)[19] and experimentally prepared undoped tetragonal zirconia (a = 5.084 Å, c = 5.182 Å)[20]. With 5 mol% titania doping, the lattice constants of both tetragonal phase and cubic phase are slightly smaller than that of YSZ systems. The lattice constants in YTDZ systems are a_t = 5.093±0.002 Å, c_t = 5.184±0.001 Å for tetragonal phase and a_c = 5.117±0.003 Å for cubic phase. This can be attributed to the smaller ionic diameter of titanium (0.074 nm) than zirconium (0.084 nm)[11]/

With a variation of TiO_2 concentration, we observed a change of lattice constants in $3Y_2O_3$-$y$$TiO_2$-$ZrO_2$ ceramics as shown in Figure 4.7(b). The tetragonal lattice constant a_t keeps decreasing, while c_t increases with TiO_2 concentration from 2 to 10 mol%, resulting in the increase of tetragonality (c_t/a_t) of zirconia. This result follows the Vegard's law of solid solution[15].

4.4.4 Elemental heterogeneity of YTDZ

It has been reported that the solubility of Y_2O_3 in tetragonal zirconia is lower than 3mol% when sintered at 1400^{o}C and it can further decrease at higher sintering temperature[21]. We therefore suspect that segregation of yttrium may have occurred in the as-prepared YSZ and YTDZ ceramics since both systems were sintered at 1700^{o}C.

Furthermore, as the focus of the project is to study zirconia at microscale, the local properties at grain-scale are of more interest to us than the bulk properties. In order to obtain single crystal tetragonal pillars that demonstrate the desired shape memory effect, we need to determine the phase composition for each particular grain and understand how different elements are distributed across grains. In addition, the information on crystal orientation needs to be obtained for the tetragonal grain inside the polycrystalline bulk YTDZ ceramics. As concluded by the XRD analysis that for zirconia with Y_2O_3 higher than 2.5 mol%, the bulk YTDZ ceramics are always composed of a mixture of tetragonal and cubic phases. Therefore, a finer characterization on the bulk ceramics with the focus on grain-scale properties was conducted, to determine the elemental distribution and phase composition of grains of interest.

As yttria is the stabilizer, the phase distribution should be directly related to the distribution of yttrium cations inside the zirconium cation matrix. It was reported that signatures of yttrium inhomogeneity has been found in the Y_2O_3-ZrO_2 system[6], especially when it is exposed to high sintering temperatures for a long time. Here we explore the elemental distribution at grain-scale, with the goal to reveal the relationship between the elemental distribution and phase segregation, with the focus on the ternary YTDZ system with both Y_2O_3 and TiO_2 as dopants.

Electron probe micro-analyzer (EPMA) that has spatial elemental resolution of submicron was employed and chemical mapping of yttrium, titanium and zirconium were conducted on the surface of both YSZ and YTDZ ceramics. Figure 4.8 illustrates an exemplar mapping conducted on $3Y_2O_3$-$5TiO_2$-ZrO_2 ceramics, together with corresponding SEM image. Two distinct elemental compositions of yttrium were identified in general, that is the "high yttrium regions" (HYR) (in yellow) and "low yttrium regions" (LYR) (in blue). By comparing the SEM image with the yttrium map, we can see that yttrium cations are segregated at grain-scale, into LYR and HYR domains. Different from what Schelling observed that the yttrium tends to localize at grain boundaries,[6] the yttrium segregation in YTDZ ceramics occurs in a grain-wise fashion. Due to the very low solubility of yttrium in tetragonal crystal, the excess yttrium tends to accumulate in certain grains and forms cubic phase. The phase is determined according to the quantitative yttria composition in both HYR and LYR, which will be elaborated in Figure 4.10(a). The titanium map is quite homogeneous as compared to yttrium as titanium solubility in tetragonal zirconia is higher than 5 mol%. The zirconium map shows slight color contrast with a pattern similar to yttrium distribution.

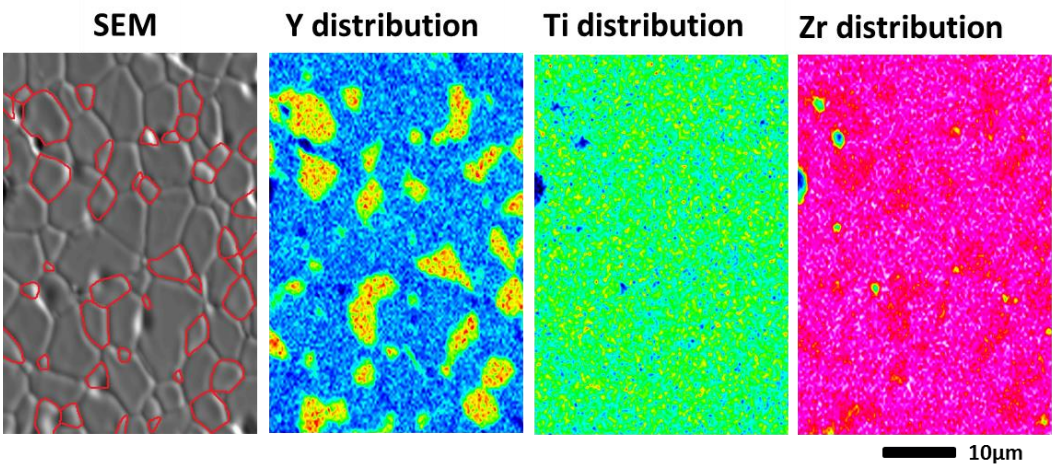

Figure 4.8 EMPA mapping of $3Y_2O_3$-$5TiO_2$-ZrO_2 ceramics, with the SEM image and elemental distribution of Yttrium, Titatnium and Zirconium at the corresponding area. The color is coded to be rainbow, with reddish colour represents higher concentration.

To study the effect of TiO_2 on yttrium segregation, samples with and without titania (i.e. $3Y_2O_3$-ZrO_2, $2.5Y_2O_3$-$5TiO_2$-ZrO_2, $3Y_2O_3$-$5TiO_2$-ZrO_2 and $4Y_2O_3$-$5TiO_2$-

ZrO_2) were mapped across an area of a few hundred μm^2, as shown in Figure 4.9. These ceramics all exhibit yttrium segregation of HYR and LYR, with patterns relatively consistent for different global compositions. The yttrium segregation in ternary YTDZ ceramics is found to have a much coarser length scale, with typical domain areas of ~ 4 μm^2 for both HYR and LYR, compared with a domain area ~ 1 μm^2 in binary YSZ ceramics. The sizes of domain areas for both YSZ and YTDZ systems are in good agreement with the corresponding grain size, confirming that yttrium elemental segregation is accompanied with the grain growth of the ceramics. It is also clear that the area fraction of HYR with respect to LYR is larger for YTDZ with more Y_2O_3.

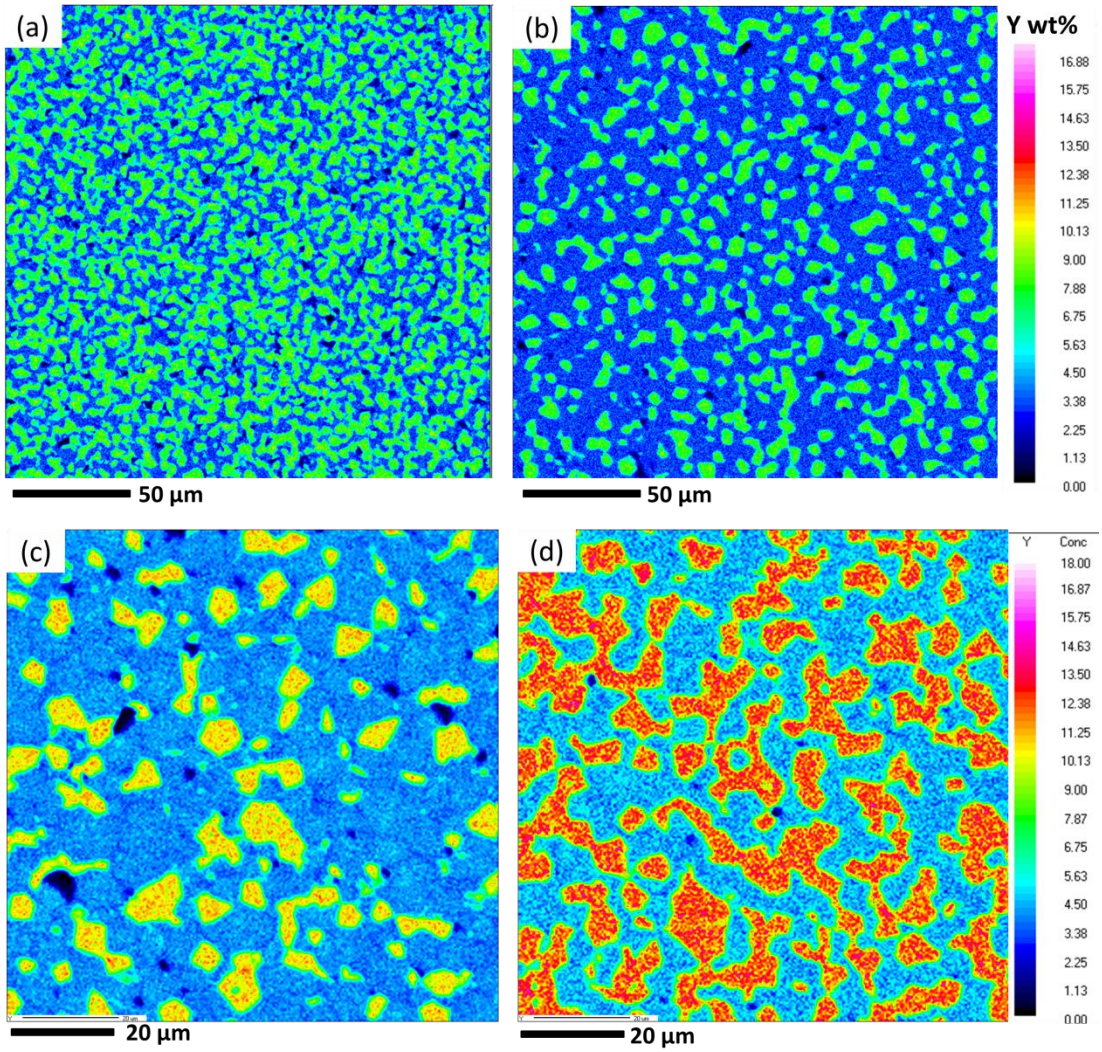

Figure 4.9 EMPA mapping of yttrium in (a) $3Y_2O_3$-ZrO_2, (b) $3Y_2O_3$-$5TiO_2$-ZrO_2, (c) $2.5Y_2O_3$-$5TiO_2$-ZrO_2, (d) $4Y_2O_3$-$5TiO_2$-ZrO_2 ceramics.

In addition to the mapping, EMPA enables quantitative spot analysis with a better accuracy of the weight fraction for each element. The corresponding local Y_2O_3 mole percentage of both LYR and HYR are shown in Figure 4.10(a). The spot analysis suggests that the HYR generally have ~ 5 mol% Y_2O_3, which can be easily distinguished from the LYR of ~ 2 mol% Y_2O_3. As the YTDZ ceramics in Figure 4.9 consist of a mixture of tetragonal and cubic phase, the HYR with 5 mol% is most likely to be cubic phase due to the low solubility of Y_2O_3 in tetragonal zirconia[21].

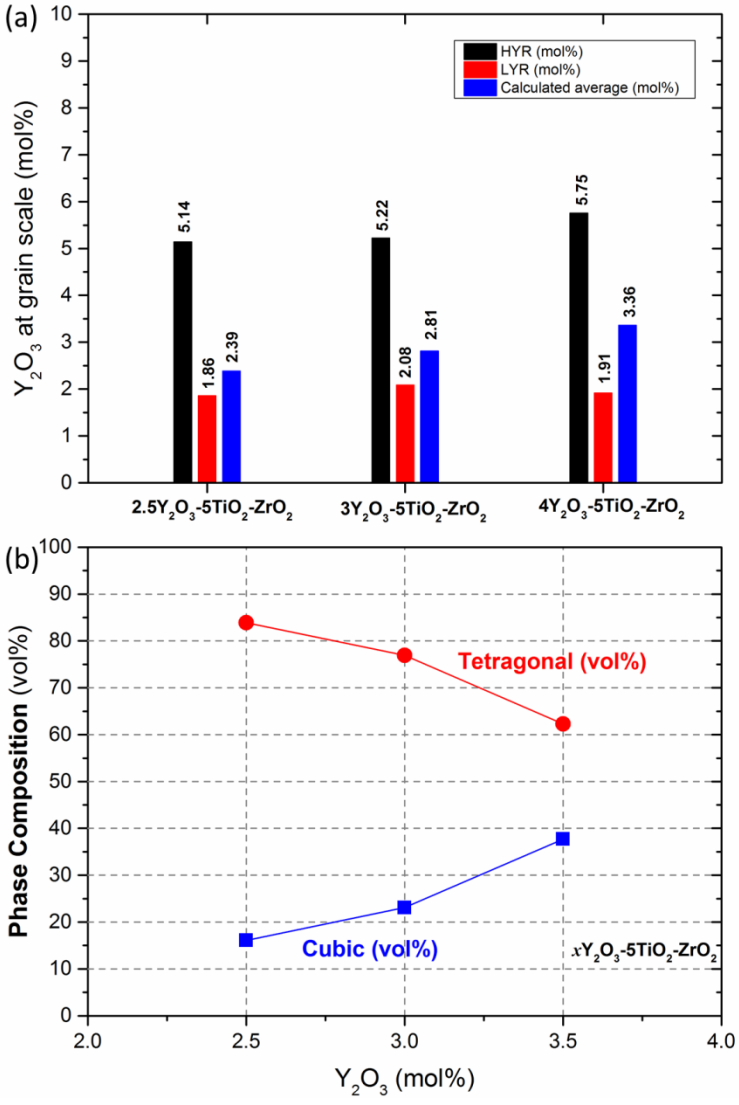

Figure 4.10 (a) Localized concentration of Y_2O_3 for high yttrium region (HYR) and low yttrium region (LYR) and (b) phase composition of HYR and LYR for xY_2O_3-5TiO_2-ZrO_2.

Therefore, the phase partition is directly resulted from yttrium segregation, whereas the excess yttrium cations in LYR were expelled from tetragonal crystals to grains with HYR and formed cubic crystals. The ratio between LYR and HYR is actually the phase composition ratio between the tetragonal and cubic phases. Assuming that the spatial distribution of yttrium is homogeneous across the whole ceramic, the volume fraction of tetragonal and cubic phase is the same as the area fraction, as plotted in Figure 4.10(b). It is clear that the YTDZ ceramics are dominated by tetragonal phase for Y_2O_3 higher than 2.5 mol%, which is in good agreement with the results from XRD analysis. When the global Y_2O_3 doping level increases from 2.5 to 4 mol%, the volume fraction of tetragonal phase drops from ~84 to ~62 vol%, accompanied by the increase of cubic phase from ~16 to ~38 vol%.

4.4.5 Phase composition at grain-scale

As tetragonal grains are of our interest, it is necessary to confirm that the grains in LYR are indeed tetragonal crystals. To enable a fine phase analysis on LYR grains, a single grain was first taken out from the $3Y_2O_3$-$5TiO_2$-ZrO_2 ceramics using Omni-Probe™ in the FEI Nova 600i Nanolab FIB/SEM system. The grain was analyzed using two techniques: X-ray micro-diffraction (μXRD) and transmission electron microscopy (TEM).

To enable analysis with μXRD, the selected grain in the LYR was first attached to a TEM grid, as shown in Figure 4.11(a). The grain was subsequently scanned with high resolution synchrotron radiation scanning using μXRD. The obtained Laue diffraction orientation map is shown in Figure 4.11(b), and the color evolution is an indication of the mis-orientation across the grain. As the difference between the red and dark purple regions is only about 0.1°, the LYR grain is confirmed to be single crystal. Each pixel in the map represents a Laue diffraction pattern on different areas of the grain, as in Figure 4.11(c). By indexing the sharp spots in the diffraction pattern with the lattice parameters obtained in section 4.3.3, we confirmed that the grain is of tetragonal zirconia (Figure 4.11(d)). Such μXRD analysis was conducted on many LYR grains and only tetragonal

phase has been identified. It is therefore confirmed that the grains in LYR are tetragonal crystals, which can be further machined into small volume tetragonal pillars.

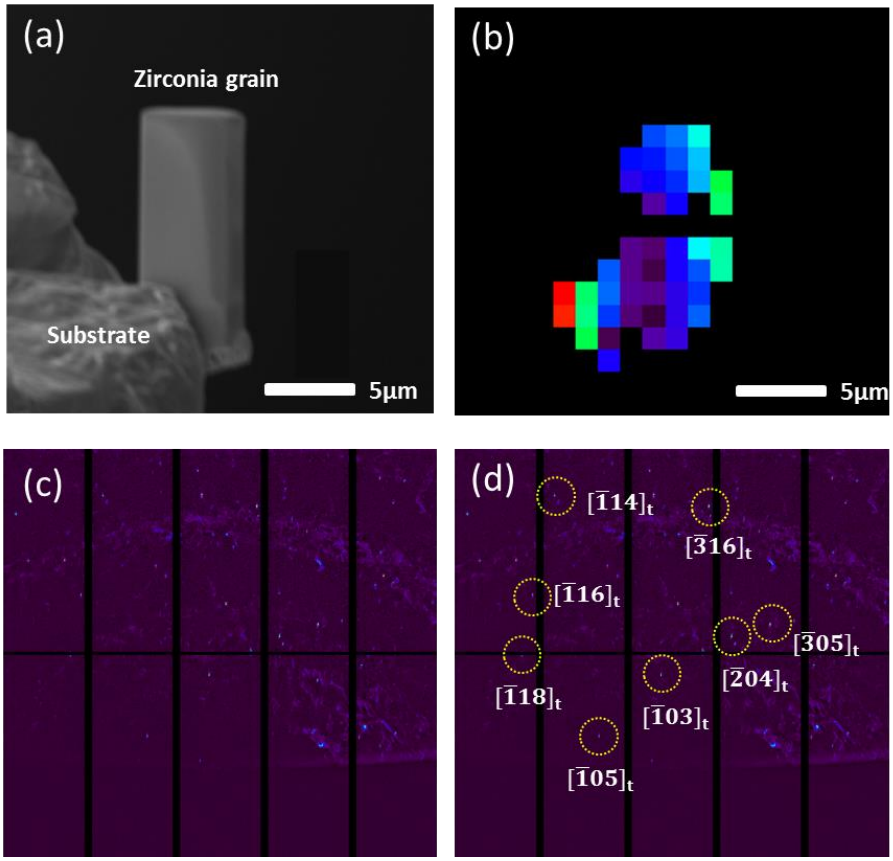

Figure 4.11 (a) SEM image of the grain cut from the LYR region, (b) the orientation map of the grain, (c) the corresponding Laue diffraction pattern and (d) its indexed peaks.

The TEM characterization of LYR grain can provide more details on the lattice arrangement and dislocations of the as-prepared grain. Thus, the grain was further thinned into lamellae as shown in Figure 4.12(a), to enable TEM and selected area electron diffraction (SEAD).

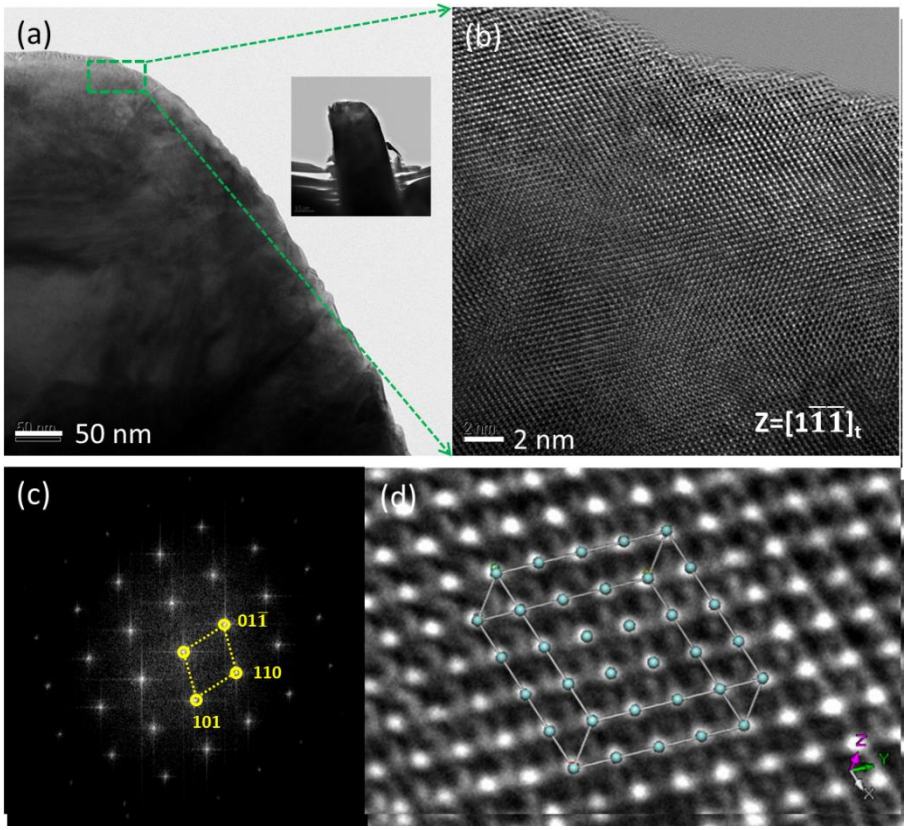

Figure 4.12 (a) A cross-section view of one section of Pillar 3 under TEM after cutting (inserted image is the view of the whole pillar area). (b) Magnified High resolution TEM image of selected area on pillar. (c) The Fast Fourier Transform (FFT) spectra of the crystal with a zone axis of $[1\bar{1}\bar{1}]$. (d) The atomic arrangement of cations matched with the unit cell with lattice parameter of a = 5.103, c = 5.187.

A high-resolution image was taken in the top region of the pillar (Figure 4.12(b)), showing crystalline structure of YSZ ceramics. It is clear that the crystals are nicely structured without any visible large scale dislocations. Based on the diffraction pattern across the lamellae (Figure 4.12(c)), the crystal was indexed as a tetragonal phase aligned along the zone axis of $[1\bar{1}\bar{1}]$. A part of the Figure 4.12(b) was magnified (Figure 4.12(d)) and it can be seen that the atomic arrangement of cations matches perfectly with the theoretical calculated unit cell of tetragonal zirconia crystal, with lattice parameters of a = 5.103 and c = 5.187 projected in $[1\bar{1}\bar{1}]$ direction. The imaging confirms that the as-milled YSZ pillar is composed of single crystal tetragonal zirconia.

4.5 Concluding Remarks

We have successfully prepared the conventional binary YSZ ceramics and the modified YTDZ ternary ceramics in bulk form. Characterization techniques of XRD, FESEM, EPMA, μXRD and EBSD have been used to study the bulk ceramics. The microstructure and phase composition of the two systems have been compared and discussed. The introduction of TiO_2 enabled meaningful characterization of spatial elemental distribution and crystal orientation for YTDZ ceramics, making it possible to prepare single crystal tetragonal pillars with known orientations. A few conclusions can be drawn as follows:

1) With the introduction of 5 mol% TiO_2, the grain size of tetragonal zirconia is significantly increased from submicron (in conventional YSZ ceramics) to microscale (in YTDZ ceramics).

2) With Y_2O_3 doping higher than 2.5 mol%, both YSZ and YTDZ ceramics have been stabilized with a majority of tetragonal phase, which is the desired parent crystal for stress-induced martensitic transformation and potential shape memory effect.

3) Yttria segregation is present inside the grains of both the YSZ and YTDZ ceramics. The YTDZ ceramics comprised of a mixture of tetragonal phase with ~ 2 mol% Y_2O_3 and cubic phase with ~ 5 mol% Y_2O_3.

Reference:

[1] R. Srinivasan, R. J. Deangelis, G. Ice & B. H. Davis. *J Mater Res.* **1991**, 6, 1287-1292.
[2] R. C. Garvie. *J Am Ceram Soc.* **1972**, 55, 303-&.
[3] P. M. Delaforce, J. A. Yeomans, N. C. Filkin, G. J. Wright & R. C. Thomson. *J Am Ceram Soc.* **2007**, 90, 918-924.
[4] K. Matsui, H. Yoshida & Y. Ikuhara. *Acta Mater.* **2008**, 56, 1315-1325.
[5] H. G. Scott. *J Aust Ceram Soc.* **1981**, 17, 16-20.
[6] K. Matsui, H. Horikoshi, N. Ohmichi, M. Ohgai, H. Yoshida & Y. Ikuhara. *J Am Ceram Soc.* **2003**, 86, 1401-1408.
[7] R. M. German. *Crit Rev Solid State.* **2010**, 35, 263-305.
[8] D. Michel, L. Mazerolles & M. P. Y. Jorba. *J Mater Sci.* **1983**, 18, 2618-2628.
[9] Y. Sakka, T. S. Suzuki, T. Matsumoto, K. Morita, K. Hiraga & Y. Moriyoshi. *Solid State Ionics.* **2004**, 172, 499-503.
[10] D. J. Kim. *J Am Ceram Soc.* **1990**, 73, 115-120.

[11] C. A. Bateman & M. R. Notis. *J Am Ceram Soc.* **1992**, 75, 1566-1569.
[12] M. M. R. Boutz, A. J. A. Winnubst & A. J. Burggraaf. *J Eur Ceram Soc.* **1994**, 13, 89-102.
[13] X. G. Miao, D. Sun, P. W. Hoo, J. L. Liu, Y. F. Hu & Y. M. Chen. *Ceram Int.* **2004**, 30, 1041-1047.
[14] F. Capel, C. Moure, P. Duran, A. R. Gonzalez-Elipe & A. Caballero. *Ceram Int.* **1999**, 25, 639-648.
[15] F. Capel, M. A. Banares, C. Moure & P. Duran. *Mater Lett.* **1999**, 38, 331-335.
[16] L. S. M. Traqueia, T. Pagnier & F. M. B. Marques. *J Eur Ceram Soc.* **1997**, 17, 1019-1026.
[17] M. Hayakawa, N. Kuntani & M. Oka. *Acta Metall Mater.* **1989**, 37, 2223-2228.
[18] M. Hayakawa & M. Oka. *Acta Metall Mater.* **1989**, 37, 2229-2235.
[19] Y. Natanzon, M. Boniecki & Z. Lodziana. *J Phys Chem Solids.* **2009**, 70, 15-19.
[20] P. Bouvier, E. Djurado, G. Lucazeau & T. Le Bihan. *Phys Rev B.* **2000**, 62, 8731-8737.
[21] N. Ohmichi, K. Kamioka, K. Ueda, K. Matsui & M. Ohgai. *J Ceram Soc Jpn.* **1999**, 107, 128-133.

Chapter 5

Martensitic Transformation Temperatures*

As reviewed in Chapter 2, the characteristic martensitic transformation temperatures (A_s, A_f, M_s, M_f) of zirconia, and their relationship with the testing temperature, is critical to assess their suitability for the stress-induced martensitic transformation and the resultant shape memory effect. For zirconia to exhibit shape memory effect, its composition must be controlled so that the transformation temperatures are within the range of testing conditions. This chapter will present our work on the exploration of the martensitic transformation temperatures for YTDZ ceramics, so as to select the suitable candidates for mechanically responsive shape memory effect.

*The content of this chapter was drafted into manuscript:

Xiao Mei Zeng, Zehui Du, Nobumichi Tamura, Qing Liu, Chee Lip Gan, *In-situ* studies on martensitic transformation and high-temperature shape memory effect in small volume zirconia. Acta Materialia, in submission.

5.1 Martensitic Transformation Temperatures in Bulk YTDZ

As the martensitic transformation can be thermally induced, differential scanning calorimetry (DSC) analysis was used to determine the four characteristic temperatures (A_s, A_f, M_s, M_f). The ceramics were heated up from 25°C to 1000°C in air at a ramp rate of 10°C/min and cooled down at the same rate. The exothermic peaks during heating and the endothermic peaks during cooling were diagnosed as occurrence of reverse and forward martensitic transformations, respectively[1]. For YSZ ceramics, we were unable to determine the transformation temperature as the peaks were not obvious enough to be differentiated from the background, mainly due to wider spread transformation temperature in small grains. For YTDZ ceramics with much larger grains, the DSC tests were conducted on seven $x$$Y_2O_3-5TiO_2$-$ZrO_2$ ceramics with x varying from 0.5 to 3.5 mol%. The corresponding heating and cooling curves are shown in Figure 5.1.

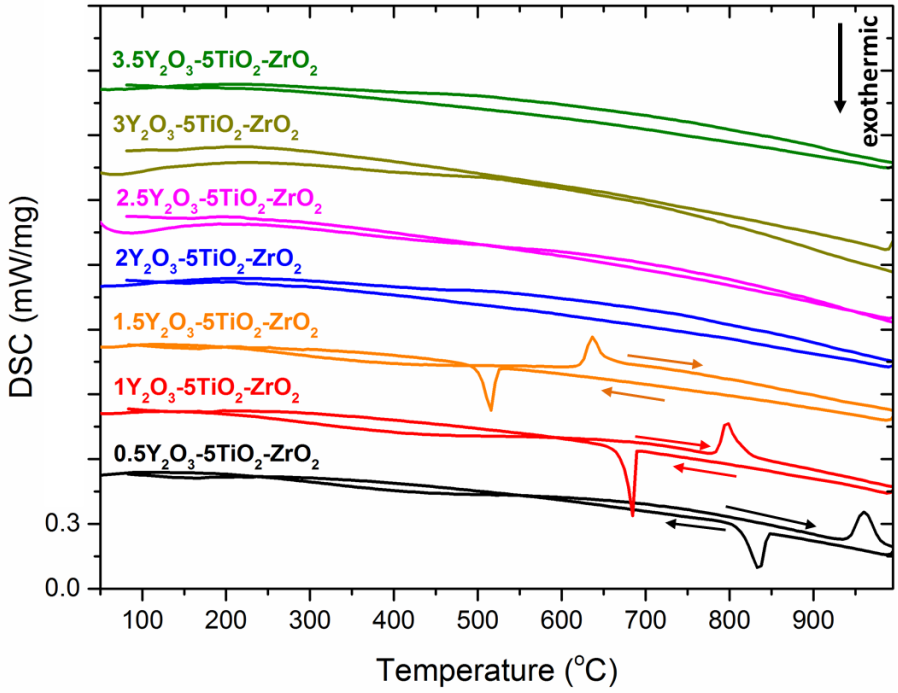

Figure 5.1 DSC curves during heating and cooling of $x$$Y_2O_3-5TiO_2$-$ZrO_2$ ceramics with x varying from 0.5 to 3.5 mol%.

Three ceramics with 0.5, 1 and 1.5 mol% of Y_2O_3 exhibited strong transformation peaks during both heating and cooling. The transformations took place within a temperature range of 80°C, suggesting that the whole bulk ceramics transformed within

~8 minutes. The four characteristic temperatures A_s, A_f, M_s, M_f of all three ceramics are lower than the transformation temperature of pure zirconia (1170°C)[2].

The transformation temperatures were extracted and plotted against the Y_2O_3 doping concentration in Figure 5.2. It is obvious that the transformation temperatures decrease linearly with Y_2O_3 doping in the ceramics, as Y_2O_3 can stabilize the tetragonal phase to lower temperatures. The linear relationship is very useful to extrapolate the A_s, A_f, M_s, M_f of those ceramics with Y_2O_3 higher than 1.5mol%, where no transformation peak was detected in bulk ceramics due to constraint from the matrix, which will be elaborated in section 5.2.1.

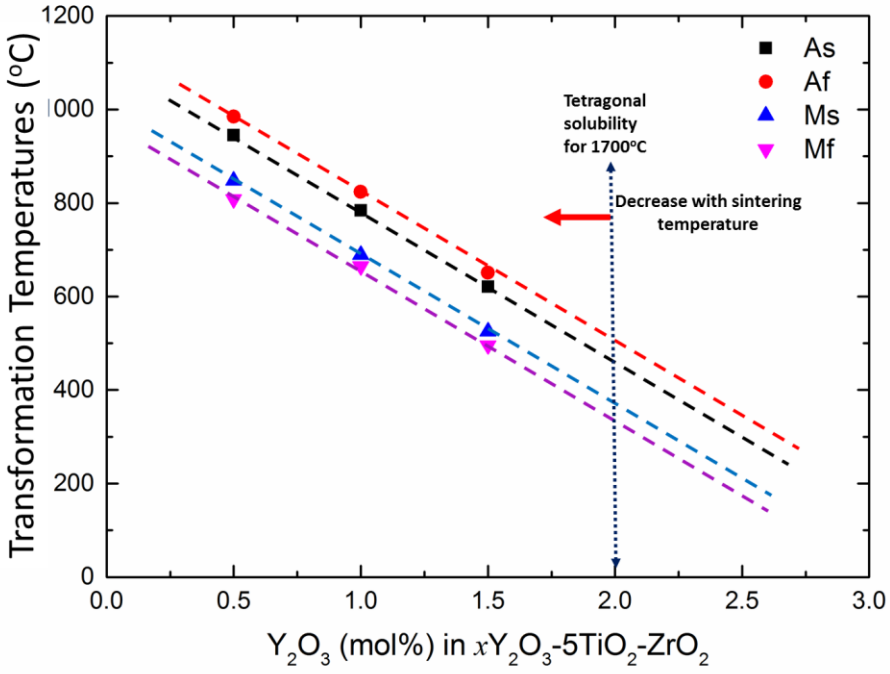

Figure 5.2 The transformation temperatures (A_s, A_f, M_s, M_f) with respect to the Y_2O_3 concentration in xY_2O_3-5TiO_2-ZrO_2 ceramics.

Based on the trend lines (dotted lines in Figure 5.2), the ceramics doped with 3 to 3.5 mol% Y_2O_3 ought to have the transformation close to room temperature (25°C). Hence if the mechanical test is carried out at room temperature, the ceramics doped with 3.5 mol% Y_2O_3 or lower should exhibit shape memory effect, while the ceramics doped by 4 mol% and above should exhibit superelasticity. However, it was discovered by Ohmichi that the solubility of Y_2O_3 in tetragonal zirconia is lower than 3 mol% when sintered at 1400°C and it can further decrease at higher sintering temperature.[3] Such

discovery suggests that the segregation of yttrium discussed in section 4.3.4 is related to the even lower solubility of Y_2O_3 in tetragonal zirconia for both YSZ and YTDZ systems sintered at 1700°C.

The work on DSC, which tells the heat absorption/release and transformation temperature, can be used to calculate the transformation enthalpy. The enthalpy for martensitic transformation is the area within each endothermic peak in Figure 5.1 in the unit of J/g. The enthalpy for unit volume ($\Delta H^{t\rightarrow m}$, kJ/cm^3) can be calculated by multiplying the area with the theoretical density (6.081 g/cm^3, using measured lattice parameters: a = 5.093 Å, c = 5.184 Å) and molar mass (123.1 g/mol) of tetragonal zirconia, and was plotted in Figure 5.3. As the trend follows a linear line, the expected transformation enthalpy for $2Y_2O_3$-$5TiO_2$-ZrO_2 is about 0.1 kJ/cm^3.

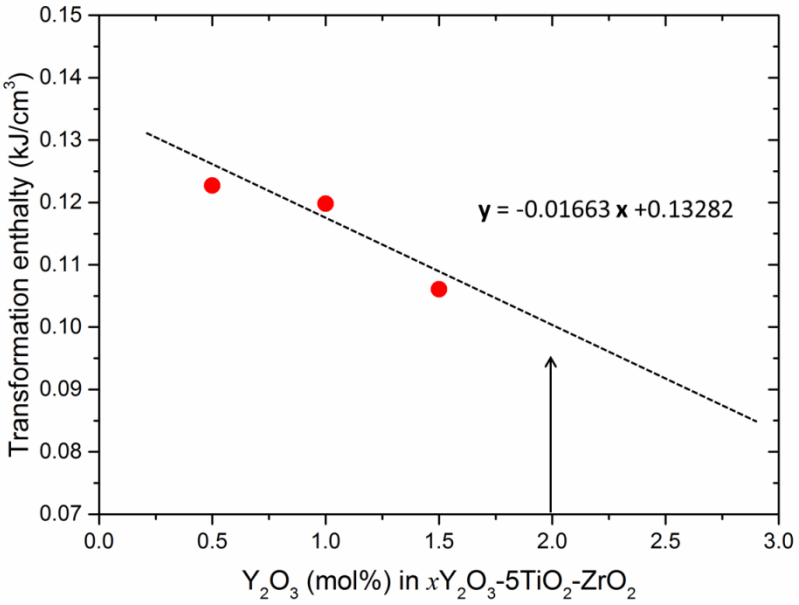

Figure 5.3 The martensitic transformation enthalpy with respect to the Y_2O_3 concentration in $x$$Y_2O_3$-$5TiO_2$-$ZrO_2$ ceramics.

5.2 Martensitic Transformation Temperatures at Grain-scale

As discussed in section 5.1, DSC characterization of the bulk zirconia was unable to determine the thermal-induced phase transformation for zirconia with more than 2 mol% yttria. With the capability to confirm the phase composition at microscale, μXRD can be used for the study of thermally induced phase transformation of particular grains.

5.2.1 Thermal-induced phase transformation

When equipped with a heating block, the ceramics can be *in-situ* heated from 25°C to 550°C while scanning with μXRD. Figure 5.4 illustrates the diffraction patterns of an exemplar grain of $2Y_2O_3$-$5TiO_2$-ZrO_2 ceramics at temperatures of 300°C and 550°C during heating. Each image consists of two sets of patterns, one from the Si substrate (used to mount the grain, the pattern is highlighted by pink circles) and the other from the zirconia (highlighted by green/orange circles). The diffraction patterns of zirconia at the two temperatures are very different, and they can be indexed as tetragonal and monoclinic crystals, respectively. Such observation suggests that the μXRD diffraction pattern can provide direct information on phase transformation during heating and cooling. The phase transformation and its characteristic temperatures of $2Y_2O_3$-$5TiO_2$-ZrO_2 ceramics can therefore be determined.

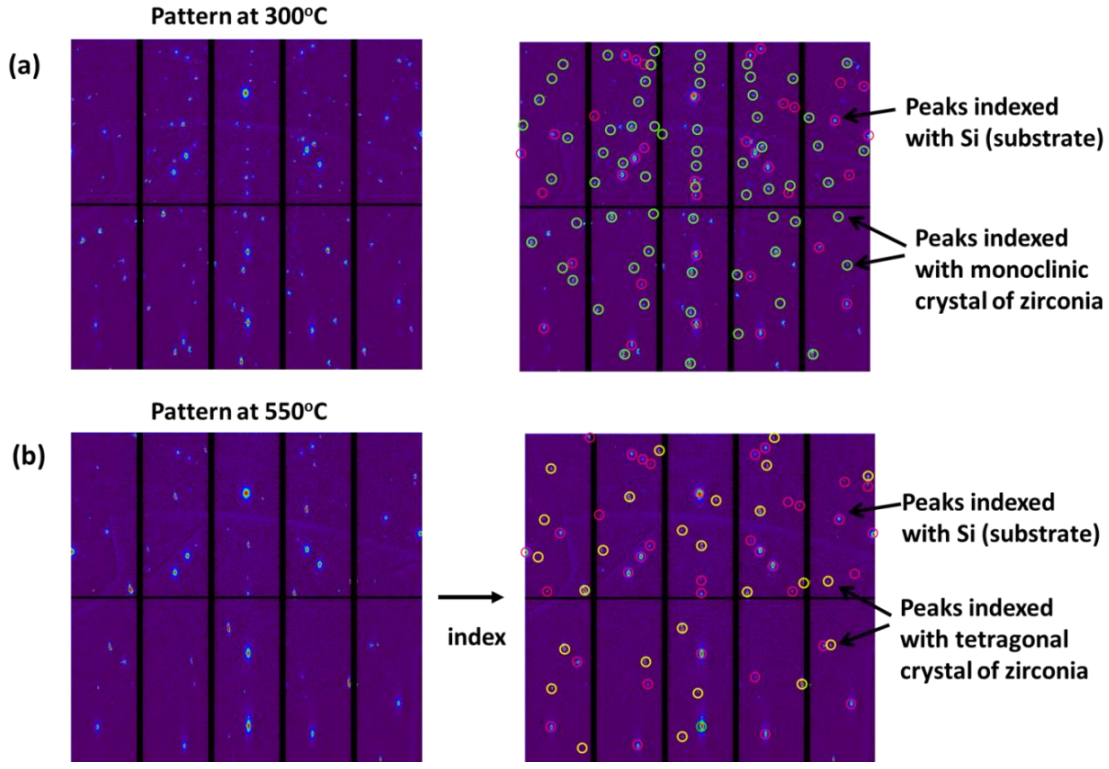

Figure 5.4 Diffraction patterns of single grain of $2Y_2O_3$-$5TiO_2$-ZrO_2 ceramics at temperatures of (a) 300°C and (b) 550°C and the corresponding crystal structures that are successfully indexed.

Figure 5.5 illustrates the phase map of a single-crystal grain evolution at different temperatures, starting from tetragonal phase at room temperature. Each pixel in the map represents a diffraction pattern on different areas of the grain, which is indexed using both tetragonal and monoclinic crystals. The colors represent the number of indexed peaks and a more reddish color means a higher number of indexed peaks. A successful indexing of more than 10 peaks in the pattern is considered valid, which otherwise is denoted as black in the map.

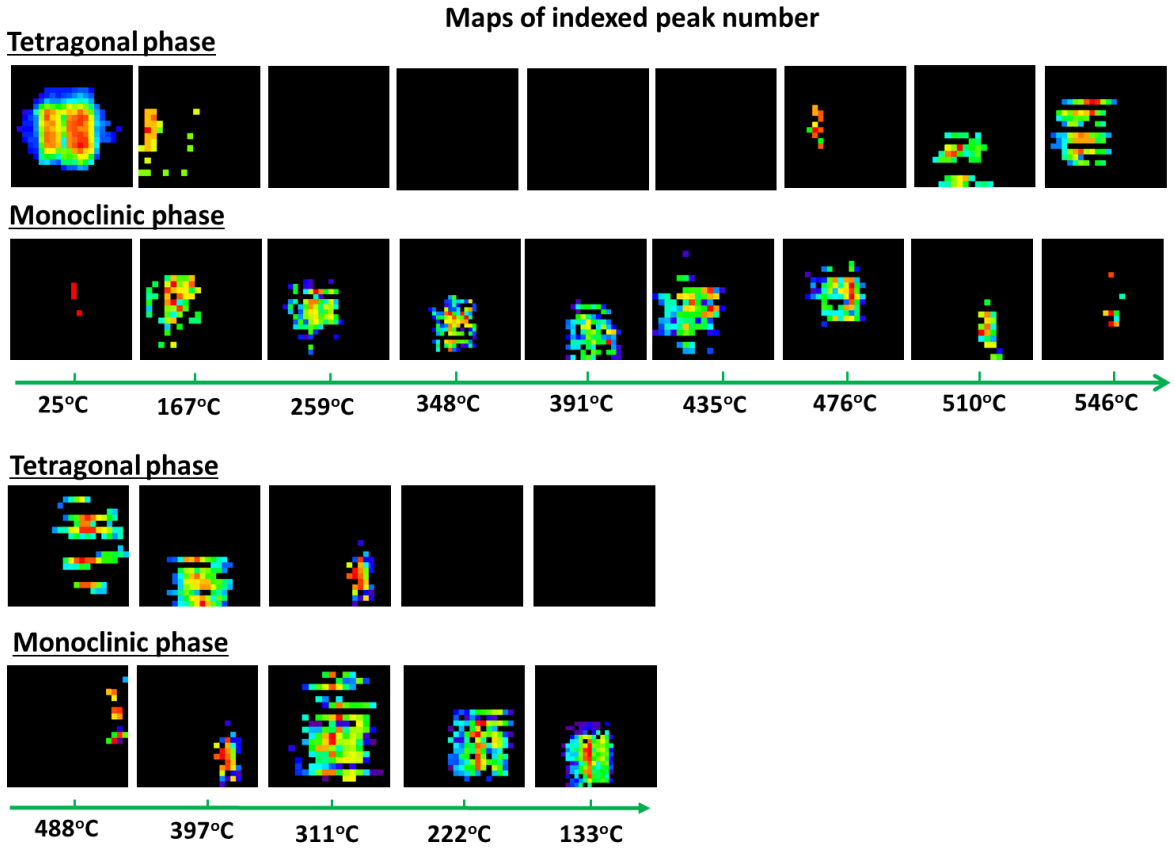

Figure 5.5 Maps of tetragonal and monoclinic crystals for single crystal $2Y_2O_3$-$5TiO_2$-ZrO_2 grain during heating from 25°C to 650°C and the corresponding cooling process.

According to Figure 5.5, majority of the grains were tetragonal phase at room temperature. When temperature went higher, the grain was better indexed as monoclinic phase, with only monoclinic and no tetragonal phase being indexed between 259°C and 435°C. Starting from 476°C, the monoclinic phase transformed to tetragonal phase, with larger and larger areas of the grain better indexed as tetragonal phase. At 546°C, the martensitic transformation was completed and the grain was mostly tetragonal phase

again. During cooling, the transformation was reversed; with the grain transforming back to monoclinic phase from 397°C and retained as monoclinic until room temperature. The grain went through three transformation processes during a cycle of heating and cooling, indicating that the reversible martensitic transformation occurred in this range.

By calculating the colored areas of tetragonal and monoclinic maps, we are able to construct the relationship between phase composition and temperatures, as shown in Figure 5.6. The change in phase composition over the temperature range shows clearly that there are three transformation processes, while the four characteristic martensitic transformation temperatures (A_s, A_f ,M_s ,M_f) can be obtained from the latter two. Therefore, for zirconia with composition of $2Y_2O_3$-$5TiO_2$-ZrO_2, the four temperatures are 476°C for A_s, 546°C for A_f, 397°C for M_s, 311°C for M_f.

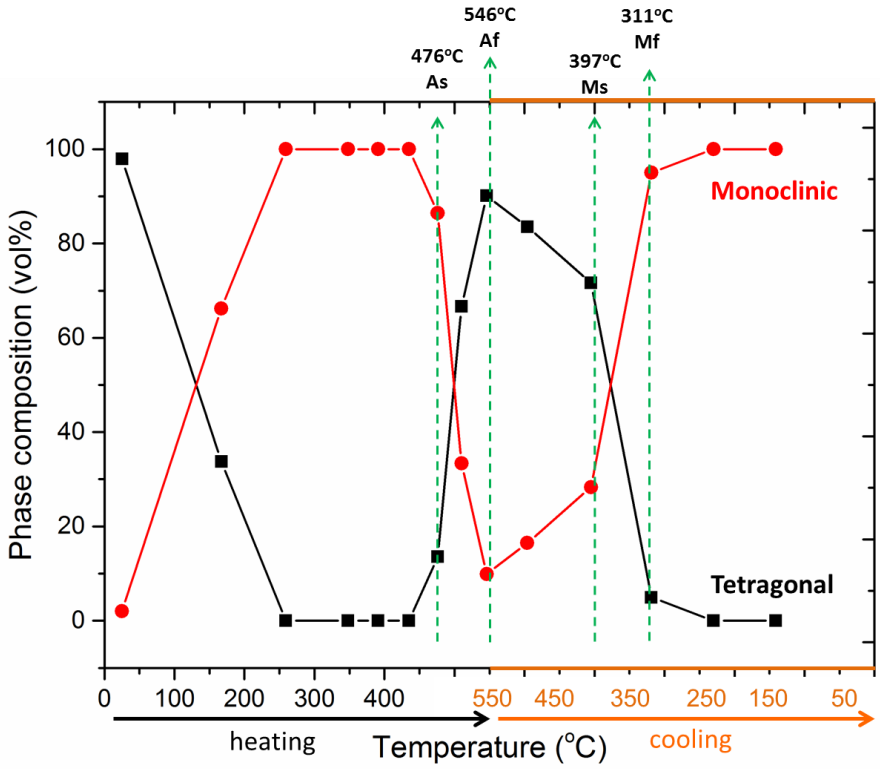

Figure 5.6 The phase compositions of monoclinic and tetragonal phases for single crystal $2Y_2O_3$-$5TiO_2$-ZrO_2 grain during heating from 25°C to 650°C and the corresponding cooling process.

These grains, in the as-produced or pristine condition, were prepared through a high temperature firing and subsequent cooling. At compositions such as studied here, where the martensitic (monoclinic) transformation temperatures are quite low, it is

common to metastably retain the high-temperature austenite phase [4,5], and that is exactly what is observed in Figure 5.5. At room temperature, the samples begin in the tetragonal phase, and revert to the equilibrium martensite phase upon heating to a temperature sufficient to overcome kinetic barriers to the equilibration, in this case, just over 100 ºC or so. The subsequent transformations that were observed are thermodynamic, and characteristics of the expected martensitic transformation.

With the μXRD analysis, Figure 5.2 can be modified to Figure 5.7 and it is clear that the transformation temperatures at 2 mol% of yttria follow the trend predicted by DSC. As for $2Y_2O_3$-$5TiO_2$-ZrO_2, the martensitic transformation from tetragonal to monoclinic phase can be thermal-induced at temperatures between 300°C and 400°C, while at room temperature, an external stress lower than the fracture strength of ceramics should be able to stress induce the transformation and enable the material to exhibit shape memory effect.

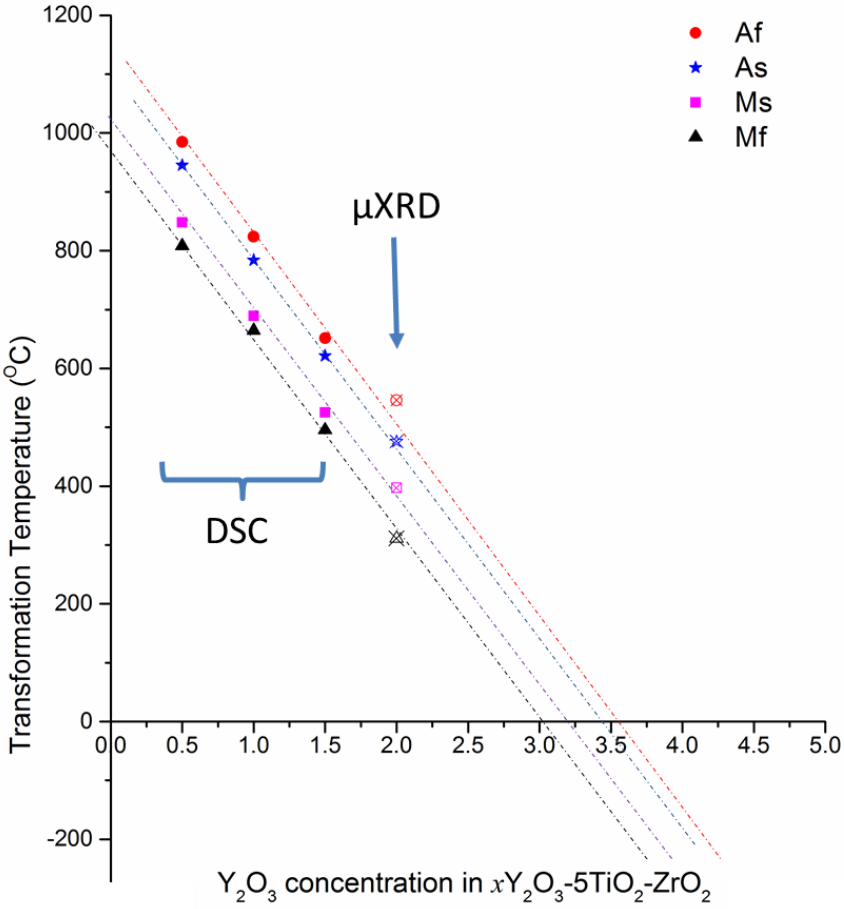

Figure 5.7 The transformation temperatures (A_s, A_f, M_s, M_f) with respect to the Y_2O_3 concentration in xY_2O_3-$5TiO_2$-ZrO_2 ceramics using the DSC data and μXRD analysis.

5.2.2 Crystal orientation relationship during transformation

In addition to the phase composition, μXRD also provides quantitative information on the crystal orientation for both monoclinic and tetragonal phases. The crystal orientation maps were constructed at each temperature during the heating and cooling cycle, as shown in Figure 5.8. The single red color in the tetragonal map at room temperature represents one single crystal tetragonal grain. While the temperature was increased from room temperature to 200^{o}C, the crystal was partially transformed to monoclinic phase, but not as a single crystal, as the blue and yellow regions represent two different crystal orientations. Further heating up suggests that the grain remained as the same monoclinic orientations between 259^{o}C to 435^{o}C. After the reverse martensitic transformation at 476^{o}C, the tetragonal map with red color reappeared, suggesting that the tetragonal orientation remained the same after transforming to monoclinic and back. Similar phenomenon was observed during cooling, with the same monoclinic orientations observed. Such repetition of color suggests that not only the transformation is reversible, but also the crystal orientation is reversible.

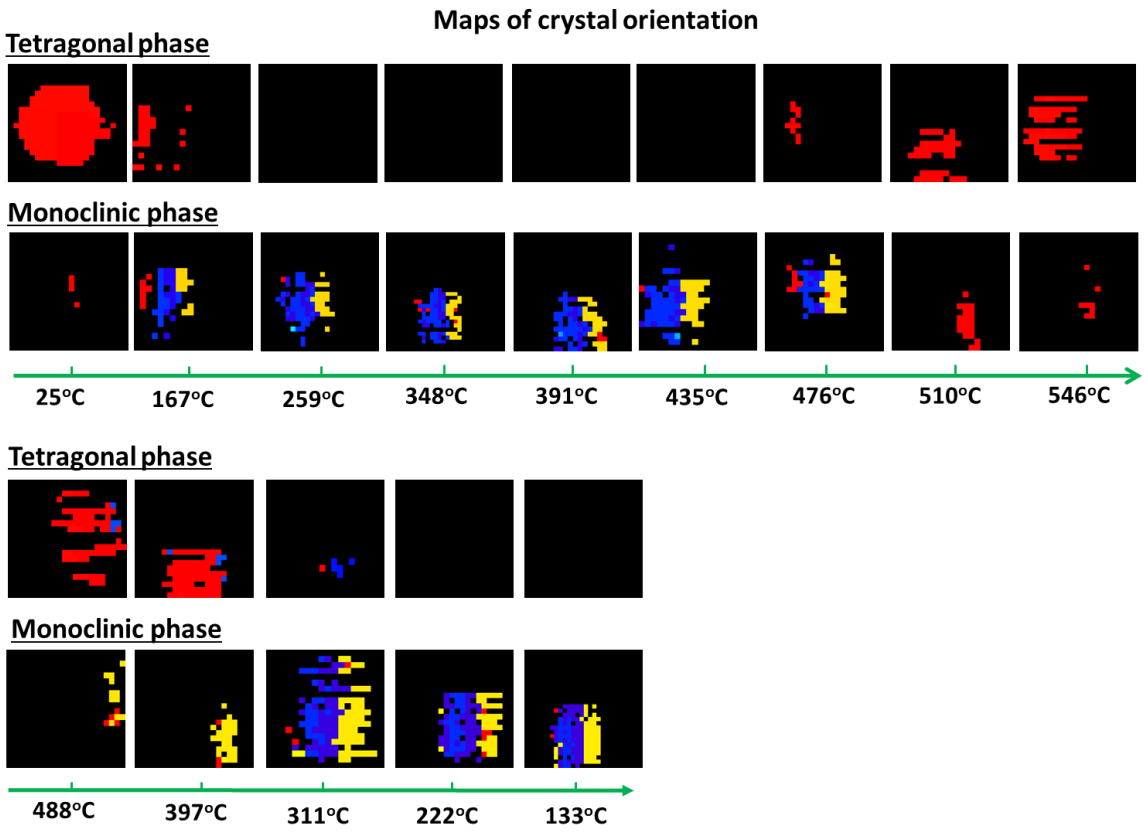

Figure 5.8 Crystal orientation maps of tetragonal and monoclinic phases for single crystal $2Y_2O_3$-$5TiO_2$-ZrO_2 grain during heating from 25°C to 650°C and the corresponding cooling process.

The exact crystal orientations of both tetragonal and monoclinic phases are shown in Figure 5.9. The red tetragonal crystal at 25°C and 546°C had similar orientations of [-1.61 2.08 0.64] and [-1.60 2.10 0.61]. The blue and yellow monoclinic crystals at 435°C and 133°C share similar crystal orientations of [-0.24 0.59 1.73], [1.85 0.59 0.53] and [0.28 -0.57 1.82], [1.85 0.60 0.53]. When projecting from different orientations, their positions in the pole figure changed. It was found that both monoclinic variants fall on the same location at [010] direction and their positions were exchanged at [100] and [001] directions. Therefore the two monoclinic structures were related by 90° rotation around [010]. The positions of tetragonal crystal in [001] and [110] pole figures were the same as the monoclinic crystal in [010] and [100]/[001] pole figures, respectively. Such relationship suggests that the transformation occurred according to correspondence B, i.e. *c*-axis of tetragonal unit cell becomes *b*-axis of monoclinic unit cell. The axis are related

by [010](monoclinic) // [001](tetragonal), [100](monoclinic) or [001](monoclinic) // [110](tetragonal).

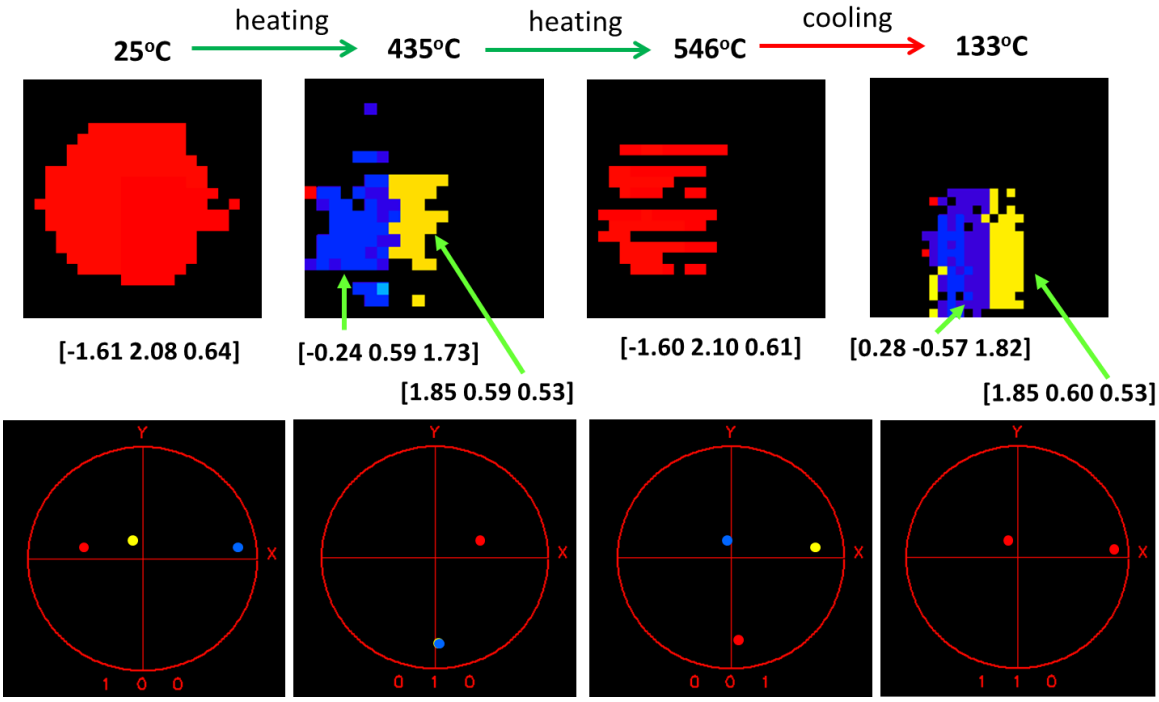

Figure 5.9 Crystal orientation of both tetragonal phase and monoclinic phase at different temperature, and the corresponding pole figures.

5.3 Concluding Remarks

Systematic analysis was conducted on the characteristic martensitic transformation temperatures of YTDZ ceramics. It was discovered that when tetragonal phase is present in the bulk ceramics, DSC is not capable to pick up any useful signals. The μXRD analysis is thus very helpful in conducting detailed study on macroscale grains for both martensitic transformation temperature and crystal orientation evolution. Two conclusions can be drawn as follows:

1) The martensitic transformation temperatures have been established with respect to Y_2O_3 concentration and it provides a valid prediction of composition for shape memory effect in YTDZ ceramics.

2) The thermal induced martensitic transformation is characterized with μXRD, with the crystal orientation found reversible during the transformation, providing the

foundation for the study on the dependence of shape memory effect on crystal orientation dependence in YTDZ ceramics in Chapter 7.

Reference:

[1] H. Tsubakino & N. Matsuura. *J Am Ceram Soc.* **2002**, 85, 2102-2106.
[2] R. C. Garvie & M. F. Goss. *J Mater Sci.* **1986**, 21, 1253-1257.
[3] N. Ohmichi, K. Kamioka, K. Ueda, K. Matsui & M. Ohgai. *J Ceram Soc Jpn.* **1999**, 107, 128-133.
[4] P. F. Becher & M. V. Swain. *J Am Ceram Soc.* **1992**, 75, 493-502.
[5] F. F. Lange. *J Mater Sci.* **1982**, 17, 225-234.

Chapter 6

Shape Memory Effect at Small Volume*

With the systematic studies on the ceramic compositions, microstructure and martensitic transformation temperature in the previous chapters, here we fabricate ceramics at microscale and study the shape memory effect of both YSZ and YTDZ ceramic systems. The deformation behaviour of single crystal YTDZ ceramics will be discussed, as a comparison to the polycrystal YSZ ceramics. It is the first demonstration of shape memory effect with significant crack-free deformation and high transformation stress in YTDZ ceramics to the best of our knowledge. Direct investigation on the phase changes during the shape memory behaviour will also be presented.

*The content of this chapter was published in article:

Xiao Mei Zeng, Alan Lai, Zehui Du, Christopher A Schuh, Chee Lip Gan, Crystal orientation dependence of stress-induced martensitic transformation in shape memory zirconia. Acta Materialia, 116, 124-135, 2016.

6.1 Shape Memory Effect at Small Scale – Proof of Concept

Stress-induced martensitic transformation between tetragonal and monoclinic phase, which is the foundation of potential shape memory effect in zirconia, has been well recognized as reviewed in Chapter 2. However, conventional polycrystal ceramics are brittle and not resilient to the transformation, as cracks generally render them useless as shape memory materials. The cracks normally nucleate at grain boundaries due to the ultrahigh internal stress that accumulate in the constraint matrix when external stress is applied. The shape memory effect is only possible when the internal stress can somehow be relaxed. The first attempt of this project was to reduce the size of the ceramics, so as to significantly enhance the surface-to-volume ratio. Creating free surface can be very effective in removing matrix constraint and releasing internal energy. The hypothesis is that, *by making the ceramics at small volume, the stress that they can sustain is high enough for martensitic transformation to occur without experiencing cracking.* This hypothesis is evaluated by preparing and studying the small volume YSZ ceramics.

6.1.1 Proof of concept

To explore the shape memory effect in small volume YSZ ceramics, cylindrical pillars, which have the simplest geometry for analysis, were milled from the bulk surface using a focus ion beam system. As YSZ ceramics generally have submicron grains, a microscale pillar will always consist of a few grains. Dozens of pillars were milled at random locations on the surface of $3Y_2O_3$-ZrO_2 ceramics and compressed uniaxially with a nanoindenter. The typical load-displacement curves of five pillars with the same size are presented in Figure 6.1. All pillars behaved elastically initially when a compressive load was applied. Some pillars fractured right after elastic deformation (P1 & P2), behaving similarly to bulk ceramics. Others survived much larger deformation without fracture (P3, P4 & P5) and the flat displacement plateau (indicated with grey arrows) are signatures of martensitic transformation. Once the load was released, some pillars managed to recover the deformation fully (P3) or partially (P4), while other did not recover at all (P5).

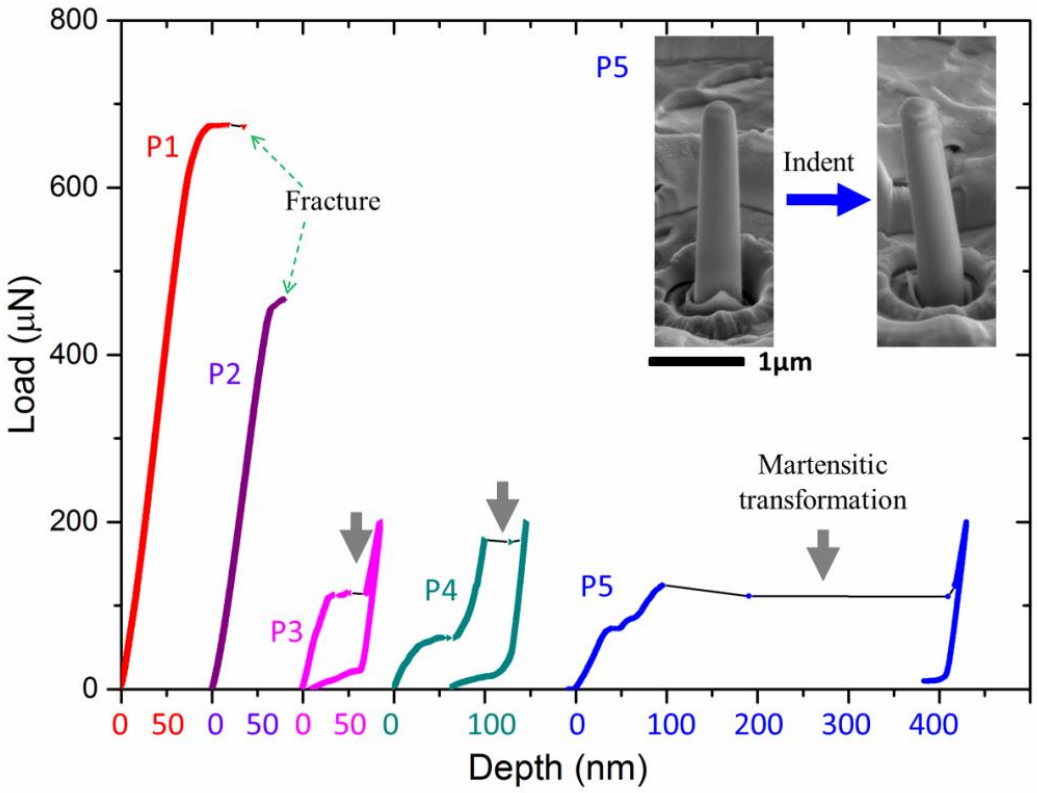

Figure 6.1 The load-displacement curves for various pillars milled from $3Y_2O_3$-ZrO_2 ceramics. The inserted FESEM images are of P5 (size 0.5 μm × 4 μm) before and after indentation test and the bending effect can be observed.

The residual displacement after unloading indicates a permanent shape change. The large residual displacement of P5 enables us to observe the obvious shape change in the SEM images, as seen in Figure 6.1. The significant bending of P5 without fracture was due to the martensitic transformation from tetragonal to monoclinic phase, and such deformation is not possible in bulk YSZ ceramics. This result proves the hypothesis that the reduction of ceramic volume to microscale could potentially enable the occurrence of martensitic transformation and therefore shape deformation in YSZ ceramics.

6.1.2 Challenges of YSZ ceramics

Although signatures of martensitic transformation has been observed in YSZ ceramics, proving the hypothesis that reducing the ceramic volume can aid in the relaxation of internal stress, the behavior of each pillar varies significantly, from fracture

without deformation to large deformation. Such large variation is mainly due to the existence of grain boundaries, where there is still internal stress concentrated. The randomly distributed grain boundaries interact with the applied load, and micro-cracks could still nucleate, just that these micro-cracks would not propagate as fast as that in bulk ceramics. A general observation is that, martensitic transformation takes place at a compressive stress much lower than the fracture strength. As the critical stress for martensitic transformation varies significantly with orientations, only those transformations with critical stresses lower than the fracture strength of the polycrystalline pillar can take place. It is also worth noting that there might still be some permanent damage and even micro-cracks in the pillar even when martensitic transformation occurs, as evidenced by the non-linearly elastic curve of P5. These permanent damages could prohibit the pillars to have complete shape recovery when heat treated and thus lead to degradation of shape memory effect. All these observations suggest that the small volume YSZ ceramic system needs to be modified, to enable repeatable and reliable shape memory effect. The analysis of grain boundaries shed light on the direction of how the YSZ can be modified.

Our proposed solution is to prepare single crystal pillar to remove grain boundaries completely. Thus the fracture strength can be significantly increased to be higher than the martensitic transformation stress, regardless of the crystal orientation of the pillar. Our second hypothesis is: *By developing single crystal YTDZ pillars at microscale, we can have robust shape memory ceramics with reliable shape memory effect that is tunable by crystal orientation, ceramic dimensions, ceramic composition and testing temperature.*

In Chapter 4, we discussed in detail that introduction of TiO_2 into the YSZ ceramics can significantly increase the grain size and enable the fabrication of single crystal micro-pillars. In this chapter, the shape memory effect of the modified YTDZ ceramics were prepared and studied systematically.

6.2 Shape Memory Effect in YTDZ

The preparation of single crystal YTDZ pillars is achieved by milling on the selected tetragonal grain with known crystal orientation, as shown in Figure 3.13(a) and

(b). The desired pillar size is with diameter of 1 μm and height of 3 to 4 μm. As the grain size is larger than the desired pillar size, the possibility of avoiding any grain boundaries during the micromachining process with FIB is thus high. All the YTDZ pillars were carefully milled to ensure a good quality cylinder with very small tapering angle as shown in Figure 3.13(c) and (d). The flat pillar top enables good contact with the conical-spherical indenter tip, to allow good mutual alignment during the compression tests. As discussed in Chapter 4, for studies of martensitic transformation at room temperature, the composition must be tuned to bring the tetragonal/monoclinic transformation temperatures into the range of ambient conditions, and the ability to retain the austenitic tetragonal phase at room temperature is specifically desired. According to the results from EPMA and DSC, the suitable local composition for the study of shape memory effect in pillars is $2Y_2O_3$-$5TiO_2$-ZrO_2.

After the compression test, the pillars were heat treated to recovery the shape deformation. The load-displacement curve of a typical YTDZ pillar is shown in Figure 6.2, together with one pillar from a binary $3Y_2O_3$-ZrO_2 ceramic for comparison. The behavior of YTDZ and YSZ pillars are very different, although both are tetragonal phase and capable of stress-induced martensitic transformation. The YTDZ pillar shows large apparent deformation, sustaining ~ 800 nm of displacement without failure. The rapid burst of large displacement is a signature of the martensitic transformation. For the two pillars of the same size, the YTDZ pillar could transform at a stress higher than the fracture strength of YSZ pillar. This observation suggests that the fracture strength is also enhanced by avoiding the grain boundaries, just as expected. The linear elastic behavior of YTDZ pillar is a result of being a perfect single crystal.

The substantial residual displacement after release of load is consistent with the bending of the as-deformed pillar as observed in the SEM image. To examine whether the pillar can recover the deformation, it was heated to 500^{o}C for 30 min. The SEM image after heat treatment shows that the pillar has almost fully recovered its shape. Such significant deformation and full recovery behavior of the pillar proves the hypothesis that small volume YTDZ ceramics have robust shape memory effect.

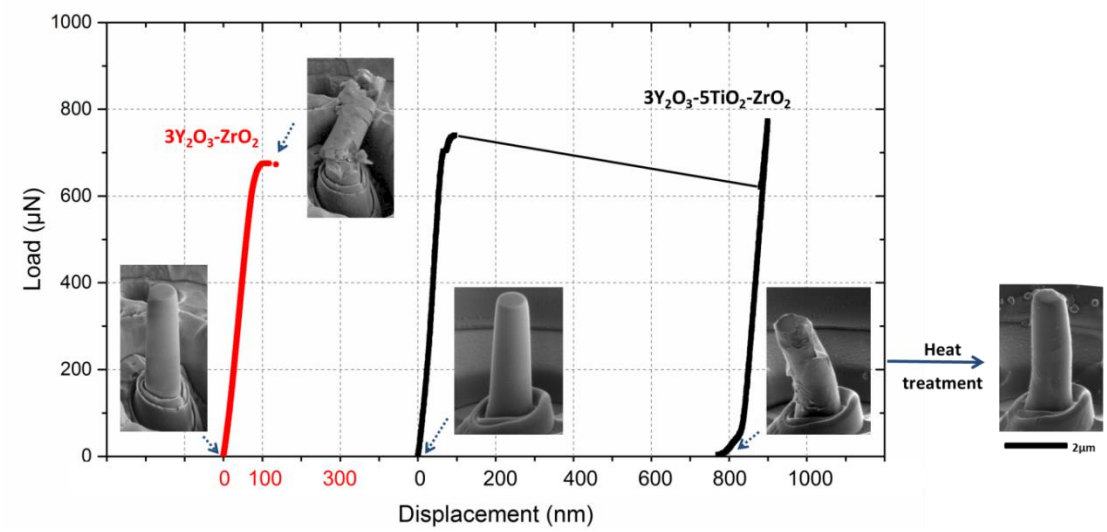

Figure 6.2 Load-displacement curves of $3Y_2O_3$-ZrO_2 and $3Y_2O_3$-$5TiO_2$-ZrO_2 pillars, and the corresponding SEM images before and after micro-compression, and after heating at 500°C.

6.3 Stress-Strain Behavior of YTDZ pillars

Next, to enable quantitative analysis of the shape memory behavior in the single crystal YTDZ system, the two characteristic properties of transformation stress and transformation strain are defined.

To account for tapering effect in each pillar, the critical stress for martensitic transformation (σ_c) was calculated based on the effective pillar diameter (d_e) and can be expressed as:

$$\sigma_c = \frac{4F}{\pi(d_e)^2} \qquad \text{Equation 6}$$

$$d_e = \left(\frac{d_t^2 + d_t d_b + d_b^2}{3}\right)^{\frac{1}{2}} \qquad \text{Equation 7}$$

where F is the critical compressive load; d_t and d_b are the measured diameters at top and bottom of the pillar, respectively. The effective diameter is used so that the actual volume of the tapered pillar is equated with an ideal cylindrical pillar with the same height. Therefore, the area within the stress-strain curve equals to the area under the load-displacement curve divided by the actual pillar volume.

The deformation strain can be expressed in terms of uniaxial strain (ε_u) that corresponds to the change of height, and shear strain (ε_s) that corresponds to the lateral deformation of the pillar. The strains are calculated as:

$$\varepsilon_u = \frac{h_{dis}}{H_0} \quad \text{Equation 8}$$

$$\varepsilon_s = \frac{l_{dis}}{H_0} \quad \text{Equation 9}$$

where H_0 is the initial height of the pillar; h_{dis} is the compressed uniaxial displacement from the load-displacement curve; l_{dis} is the measured lateral displacement from the SEM images.

Here we report two representative pillars with different transformation behavior and transformation stress.

6.3.1 Single-burst transformation in YTDZ pillars

As shown in Figure 6.3(a), Pillar 1 with top surface orientation of (120) was compressed uniaxially to a maximum load of 3000 μN and the resultant load-displacement curve is plotted in Figure 6.3(e). After the elastic compression, Pillar 1 went through a large single-step displacement plateau, which corresponds to the martensitic transformation from tetragonal to monoclinic phase as shown in Figure 6.3(e). The corresponding stress-strain curve was calculated according to Equations 6 and 8, and is indicated in Figure 6.3(e). Pillar 1 attained a maximum uniaxial strain of 5.2%, of which around 2.8% can be attributed to the plateau which formed within 0.015 s at a critical stress of 2.3 GPa.

The as-deformed morphology of Pillar 1 is shown in Figure 6.3(b) and a large shear distortion away from the compression axis is found. However, the top portion of the pillar where the tip was in contact remained flat and perpendicular to the compression axis; the shape change seen in this pillar is not due to bending from off-axial loading, but rather is a result of the mandatory transformation shear associated with the martensitic transformation. The transformation appears to have occurred monolithically across all of its unconstrained volume in a single martensite domain which is consistent with the observation of a single displacement burst in Figure 6.3(e).

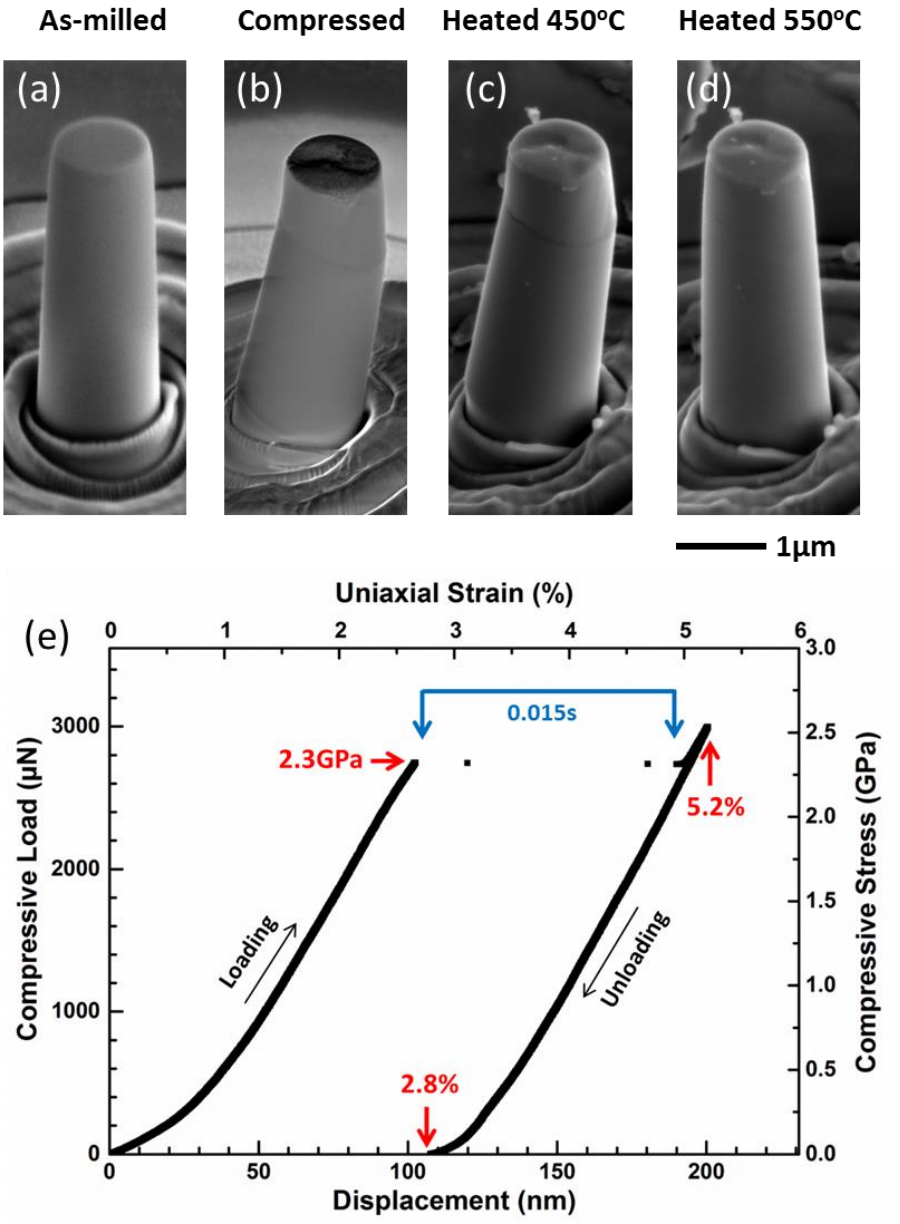

Figure 6.3 SEM images of Pillar 1 when (a) freshly milled, (b) after compression, (c) after heating at 450°C and (d) after heating at 550°C. The viewing angle is 52°. (e) The load-displacement and stress-strain curve of Pillar 1 during compression and unloading.

Martensitic transformations are reversible upon heating to a temperature higher than the austenite finish temperature. The thermally induced shape recovery of Pillar 1 was examined by first heating to 450°C, where no recovery was observed (Figure 6.3(c)). With subsequent heating to 550°C, the pillar became erect again and the single martensite

domain completely disappeared in a single step reverse transformation effecting shape recovery (Figure 6.3(d)). The austenite reversion temperature is between 450^{o}C and 550^{o}C.

6.3.2 Multi-burst transformation in YTDZ pillars

Most of the pillars tested behaved similarly to Pillar 1, whereas a few behaved quite differently. Pillar 2, with similar size but a different surface orientation of (203) was milled as shown in Figure 6.4(a). A similar uniaxial compression cycle was applied with a maximum load of 1200 μN and the resultant load-displacement curve is plotted in Figure 6.4(e). The displacement response of Pillar 2 was a sequential multi-step displacement plateau, which is markedly different from the single-step response of Pillar 1. After linear elastic deformation, the clear sequence of multi-step displacement bursts was observed beginning at a stress of ~0.65 GPa, resulting in a maximum uniaxial strain of 4.2%, of which 2.5% was unrecovered after unloading.

Examination of the as-deformed pillar geometry in Figure 6.4(b) shows that shearing had occurred as multiple inclined transformation domains, a behavior that is quite different than that observed in Pillar 1. The dozen or so stripes observed on the lateral surface of the compressed pillar indicate the presence of multiple layers of variant, as has been observed in metallic SMA pillars during stress-induced martensitic transformation.[1,2] It is envisioned that each of the variant pairs is produced sequentially in response to the stress, and each might be responsible for a single displacement burst or serration in the load-displacement curve in Figure 6.4(e); the number of discernible bursts seems to reasonably match the number of discernible variant pairs on the surface of the deformed pillar.

Pillar 2 was first heated at 400^{o}C, after which a number of the martensite variants in the top portion of the pillar disappeared, presumably reverted to austenite phase (Figure 6.4(c)). One variant near the top and those located at the bottom of the pillar remained, but subsequently disappeared upon further heating to 550°C (Figure 6.4(d)). The disappearance of the striped pattern on the pillar indicates a shape recovery by multi-step reverse martensitic transformation.

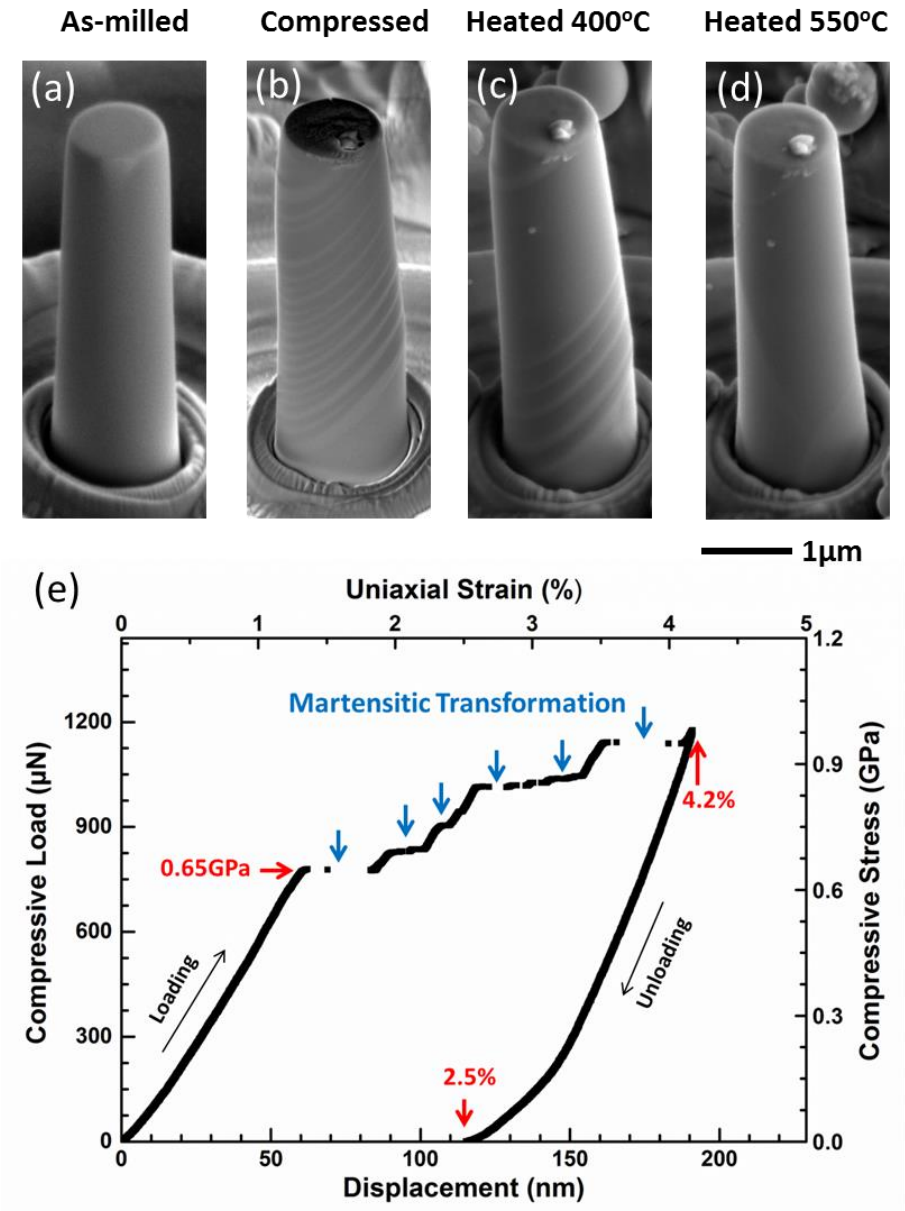

Figure 6.4 SEM images of Pillar 2 when (a) freshly milled, (b) after uniaxial compression, (c) after heating at 400°C and (d) after heating at 550°C. The viewing angle is 52°. (e) The load-displacement and stress-strain curve of Pillar 2 during compression and unloading.

6.3.3 Patterns of martensitic transformation in pillars

As shown in Figure 6.3 and Figure 6.4, compression and heat treatment led to significant shape change and recovery in both pillars, demonstrating shape memory in single crystal YTDZ ceramics. However, the results in a broad sense mirror those of our

group's prior work on other zirconia based ceramics[3], and hence we believe that the small sample size and the single crystal structure contribute to the ability of these samples to accommodate the transformation strains without cracking. It is interesting to note that the YSZ is known for exhibiting especially rapid, autocatalytic bursts of martensitic transformation as compared with, e.g. Ce-doped zirconia[4], so it is encouraging to see the shape change successfully accommodated in YTDZ, which is a modified YSZ.

The reduction of YSZ dimension not only results in the elimination of cracks, but also affects the martensitic transformation behavior. Looking at the cylindrical surfaces of both pillars, the strips signify the habit plane[5], which is the interface between the transformed variant and the parent tetragonal crystal. Figure 6.5 schematically illustrates the habit planes with respect to the pillar geometries of the as-deformed Pillar 1 and Pillar 2. Despite the fact that Pillar 1 involves a single variant/single domain transformation while Pillar 2 exhibits multiple discrete transformation bursts, they both formed plate-type martensite with parallel habit planes at both ends. Unlike the pyramid-type martensite that is commonly observed in bulk zirconia and involves self-accommodation, the formation of plate-type martensite is preferred at places of less matrix constraint like sample edges.[6] The resultant difference in habit plane between pyramid-type and plate-type martensite[6] suggests that the martensitic transformation behaviour is related to the matrix constraint. For defect-free single crystals, the transformation tends to nucleate at the free surfaces;[7] whereas in polycrystalline zirconia, the grain boundaries and triple-junctions have been widely recognized as martensite nucleation sites, due to the highly concentrated stress.[8] Therefore, the resulting orientation dependence of transformation behavior for the small volume pillar should be different from that of bulk zirconia. A systematic study of the orientation dependence of small volume shape memory zirconia will be discussed in Chapter 7.

Though the exact mechanism for the multi-burst transformation in Pillar 2 remains unclear to us, the physical constraints could offer a reasonable explanation. Unlike the thermally induced transformation that normally involves self-accommodation to adjust to matrix constraint, it is less preferred for stress-induced transformation at surface to form twinned variants[6], especially for pillars with large surface-to-volume ratio. In addition to the fact that the transformation takes place in a sequential manner, we propose that the

self-accommodation by spontaneous twining is not likely the mechanism for the behaviour of pillar 2. During the martensitic transformation, the pillar tends to shear in directions perpendicular to the compression axis, while the friction from the pillar top constrained it from shearing freely. The competing mechanism should account for the different responses recorded for Pillar 1 and 2, which are otherwise quite comparable in terms of geometry and composition. For Pillar 1, majority of the body can shear during one transformation without exceeding the physical constraint; whereas for Pillar 2, only a small portion of the body can transform each time. Looking at Pillar 2 after the stress-free heat treatment at 400^{o}C in Figure 6.4(c), the free top surface allows the pillar to shear as it should be during the transformation and some chevron pattern disappeared

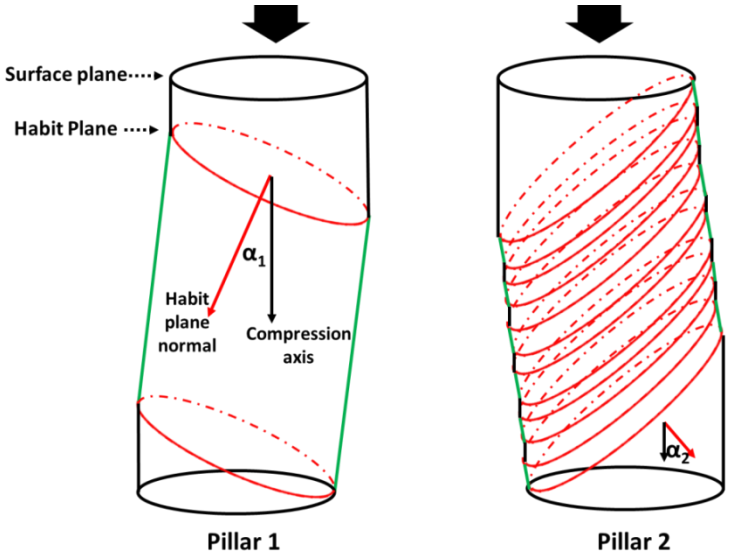

Figure 6.5 Schematic illustration of habit plane with respect to the pillar geometry and compression axis.

6.3.4 Partial transformation of pillars

Another interesting observation from Figure 6.3 and 6.4 is that only a portion of each single crystal pillar is transformed. As the pillars are not completely constraint-free ceramics, we believe the physical constraints at the top and bottom of the pillar could contribute to the shape deformation behavior. The partial transformation becomes important when calculating the transformation strain. The measured strain over the plateau was calculated with respect to the whole pillar in Figure 6.3(e) and thus needs to

be adjusted by dividing the actual plateau length with the actual transformed body. The true transformation strain of Pillar 1 is 3.46%, higher than the estimated 2.8% in Figure 6.3(e). The sequential transformation pattern of Pillar 2 further complicates the calculation for the strain along compression axis. Taking each step of plateau in Figure 6.3(e) as one single transformation, the cumulative plateau displacement is 81.80 nm, much smaller than the residual displacement of 115.33 nm. The partially transformation also suggests that the elastic behavior during unloading should reflect a mixed property of tetragonal and monoclinic phases.

6.3.5 Transformation stress of YTDZ pillars

One major difference between Pillar 1 and 2 is the large variation in critical stress for transformation. The critical stress of 2.3 GPa for Pillar 2 is four times higher compared to that in Pillar 1, suggesting that [203] is a soft direction for the martensitic transformation as compared to [120]. The martensitic transformation from the tetragonal phase to the monoclinic phase occurs along the habit plane, by shearing the tetragonal face into one of the 3 correspondences A, B and C[9]. According to the Clausius-Clapeyron relationship[10], the magnitude of the transformation stress along the habit plane is inversely related to the shape strain. As the shape strain for correspondence B and C is a constant of 0.1640, whereas correspondence A is unlikely in yttria stabilized zirconia[4], the magnitude of transformation stress can be assumed to be constant for both correspondence B and C. The difference in the critical stress along the compression axis can be explained by its alignment with the habit plane. To mechanically induce the transformation, the applied stress along the compression axis should reach the critical point where its resolved component along the habit plane exceeds the transformation stress[2]. Therefore, the externally required critical stress should be inversely related to $\sin\alpha$, where α is the angle between the normal of the inclined habit plane and the compression axis. This complies with the observation in Figure 6.5, that Pillar 1 with high critical stress has a small $\alpha_1(24.5^o)$; whereas Pillar 2 with a smaller critical stress has a larger $\alpha_2(40.5^o)$. A systematic study on the orientation effect on transformation stress will be elaborated in Chapter 7.

6.4 Martensitic Transformation in YTDZ pillars

In the previous discussion, we diagnosed the displacement plateau as the signature of martensitic transformation, as there is no other competing mechanism that can generate such a large strain burst. There has been no evidence supporting the theory that the shape recovery was due to the reverse martensitic transformation. However, the single crystal structure of the pillar allows a direct proof of such transformation behavior with transmission electron microscopy (TEM) and selected area electron diffraction (SEAD) characterizations.

One pillar (Pillar 3) was therefore prepared to investigate the crystallographic changes that accompany the martensitic transformation using TEM. Pillar 3 was machined on the same YTDZ ceramics with the same method as Pillar 1 and Pillar 2 (Figure 6.6(a)). It was subjected to a uniaxial compression with same configuration as Pillar 1 and Pillar 2. It behaved very similarly to Pillar 1 (Figure 6.6(b)), with a large one-step displacement plateau and significant body shearing was observed. The compressed Pillar 3 was then cut into lamellae and imaged by TEM. Electron diffraction was performed across the whole area of the lamellae and two sets of SAED pattern were obtained. The pattern in the center was best indexed as monoclinic phase with a zone axis of $[101]_m$, whereas the pattern at the bottom was indexed as tetragonal phase with a zone axis of $[111]_t$. The index suggests that Pillar 3 went through a partial transformation; with the bottom section remained as tetragonal phase. Considering the 45 degree rotation between monoclinic and tetragonal unit cell as shown in Figure 6.7, direction $[111]_t$ is parallel with $[101]_{m.}$ That is, the $_c$-axis of tetragonal unit remains to be $_c$-axis in monoclinic unit cell. Such lattice analysis suggests that the two zone axes are aligned in direction, meaning the transformation occurs in correspondence C.

The imaged lamellae was then heat treated at 550^oC (same heating conditions as Pillar 1 and Pillar 2) and imaged by TEM again. The film was found straightened after heat treatment (Figure 6.6(c)) and the diffraction pattern was best indexed as tetragonal phase with a zone axis of $[11\bar{2}]$.

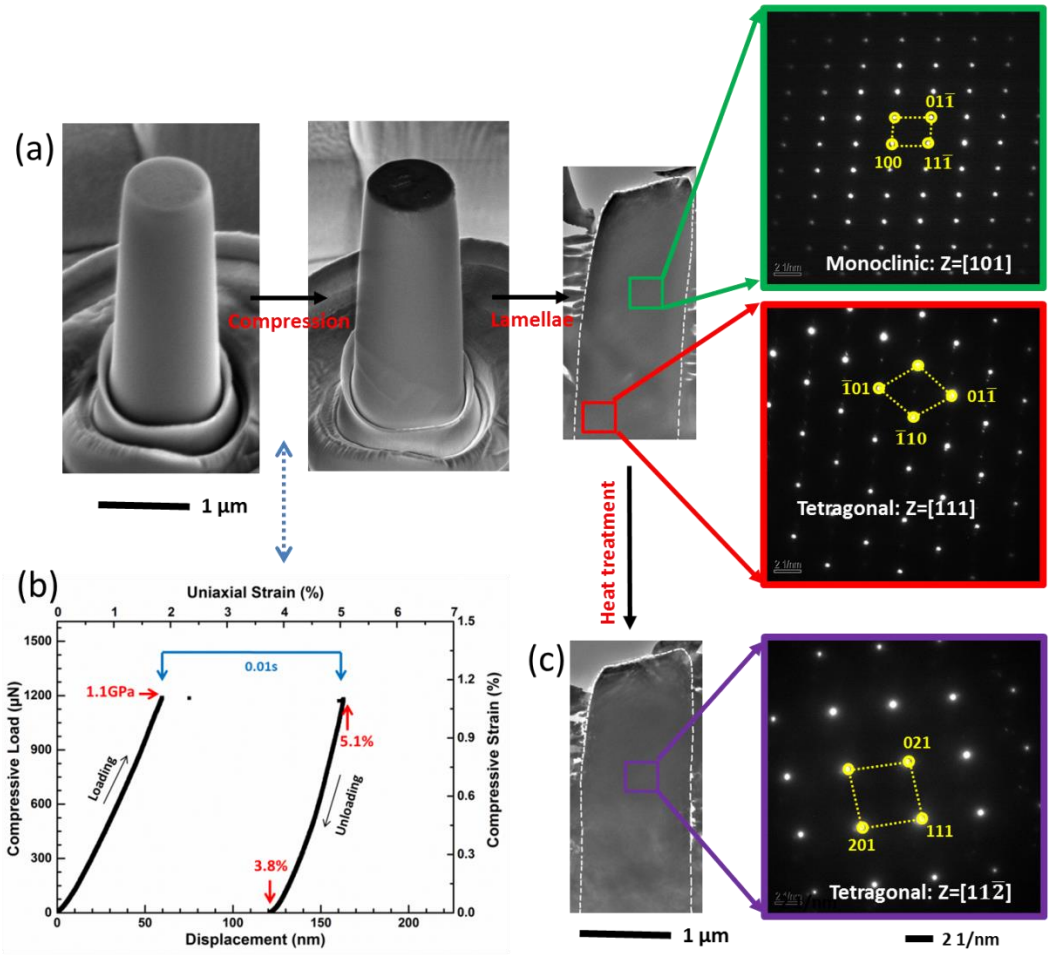

Figure 6.6 (a) Pillar 3 before and after compression, together with a cross-section view of Pillar 3 after cutting into lamellae and the corresponding SAED patterns at two positions. (b) Load-displacement (stress-strain) curve of Pillar 3 during compression. (c) Cross-section view of Pillar 3 lamellae after heat treatment with the corresponding SAED pattern.

The observance of monoclinic phase in the compressed pillar suggests that the tetragonal zirconia went through martensitic transformation during compression. It directly proves our hypothesis that the strain plateaus in the aforementioned stress-strain curves and the shape change of the pillars are induced by martensitic transformation. The identification of tetragonal phase after heat treatment in the same pillar provides straightforward evidence that the recovery of the pillar shape is induced by reverse martensitic transformation. Thus the TEM characterization provides a clear and accurate understanding of the stress-induced martensitic transformation and heat-induced reverse

martensitic transformation associated with shape deformation and recovery in shape memory ceramics.

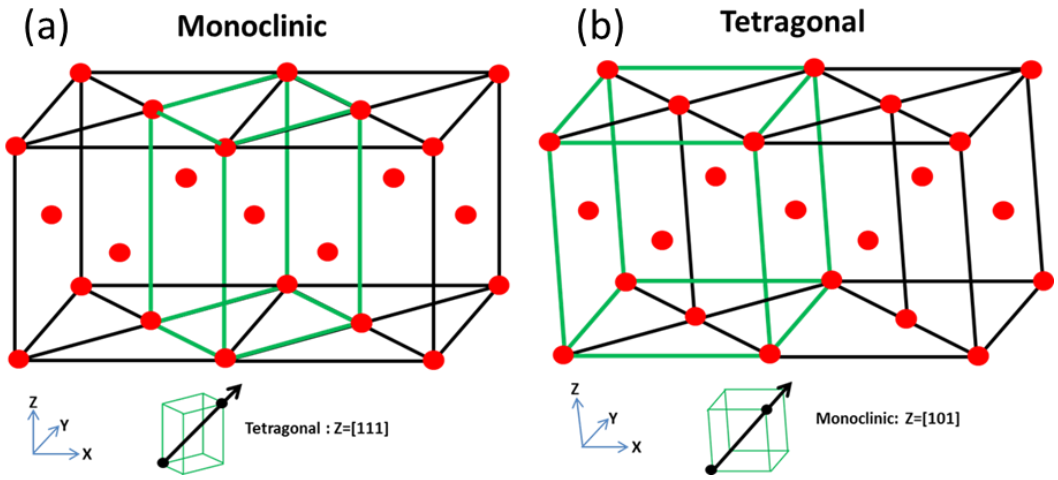

Figure 6.7 Unit cells of (a) monoclinic phase and (b) tetragonal phase, and the zone axis corresponding to the SAED pattern in the center and bottom of the indented Pillar 3.

6.5 Comparison with Shape Memory Alloys

With the above observations, the shape memory behaviors of single crystal YSZ ceramics can be very diverse. The critical stress for initiating martensitic transformations varied in a large range of 0.65 - 2.3 GPa whereas deformation strain of 6-11% was achieved. The critical stress and strain of both pillars are plotted in Figure 6.8, together with the data from many well-recognized shape memory alloys such as the Ni-Ti alloy, Cu-Al-based alloy and Fe-Ni based alloys and bulk shape memory ceramics[1,3,11-19]. Shape memory alloys can have transformation strain of 1% to 13.5%, whereas the transformation stress is limited to less than 0.8 GPa. On the other hand, bulk zirconia ceramics such as Ce-TZP, Mg-TZP and YSZ have demonstrated a significantly higher critical stress, varying in the range of 1 - 3.2 GPa. However, the brittleness of such bulk ceramics limited their strain to be less than 1%. The single crystal YSZ micro pillars we presented here combine the outstanding properties of both the shape memory ceramics and alloys, such as ultrahigh critical stress and large recoverable strain, thereby representing a different class of shape memory materials with potential large output energy.

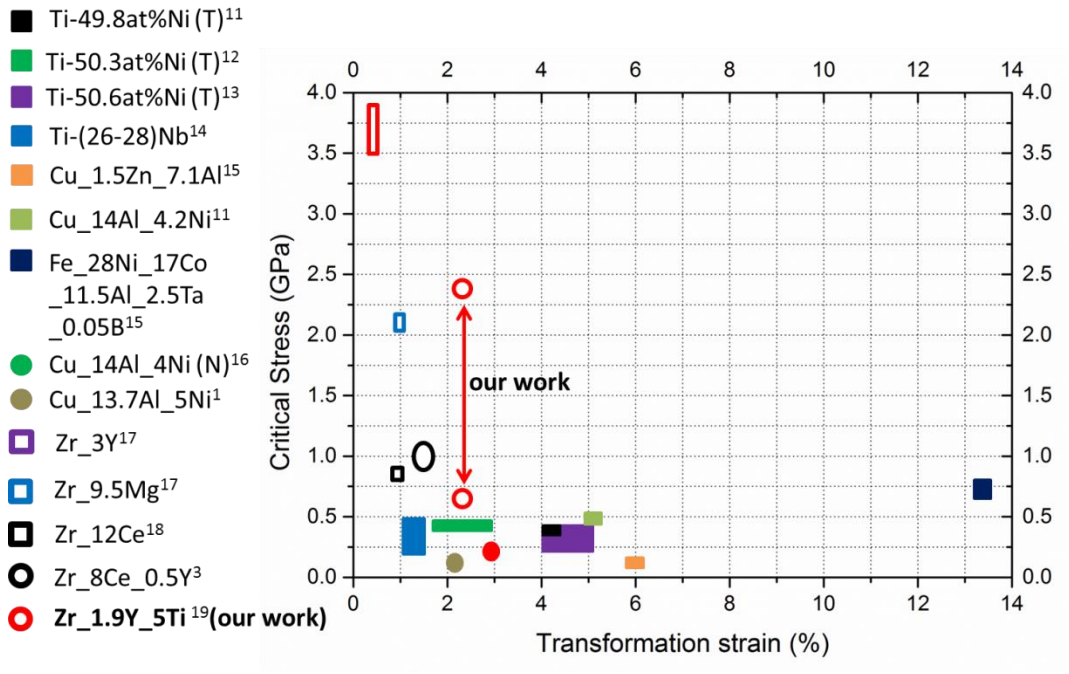

Figure 6.8 The transformation stress and strain of our YSZ ceramic as compared to various shape memory alloys and ceramics at room temperature[1,3,11-19]. (□: Bulk materials. ○: samples in submicron scales. Solid shape: shape memory alloys, hollow shape: shape memory ceramics).

6.6 Concluding Remarks

In conclusion, our studies have demonstrated that YSZ ceramics can exhibit robust shape memory behavior by having a large surface area to volume ratio structure. By fabricating single crystal micro-pillars, they could be significantly deformed without fracture during compression, demonstrating the characteristic shape memory effect with large recoverable shear strains (up to 11%) and extremely high transformation stresses (up to 2.3 GPa). TEM characterization verified the underlying phase transformations, including reversible martensitic transformation between tetragonal and monoclinic phases. The critical stress measured depends very sensitively upon the orientation difference between the crystal and the habit plane, which will be further evaluated in Chapter 7. Compression axis that is more parallel to habit plane normal shows a higher critical stress that those less aligned. In either case, though, shape recovery was achieved within a narrow range of temperature between 400-550^{o}C.

Reference:

[1] J. San Juan, M. L. No & C. A. Schuh. *Adv Mater.* **2008**, 20, 272-+.
[2] M. Mamivand, M. A. Zaeem, H. El Kadiri & L. Q. Chen. *Acta Mater.* **2013**, 61, 5223-5235.
[3] A. Lai, Z. H. Du, C. L. Gan & C. A. Schuh. *Science.* **2013**, 341, 1505-1508.
[4] P. M. Kelly & L. R. F. Rose. *Prog Mater Sci.* **2002**, 47, 463-557.
[5] J. Chevalier, L. Gremillard, A. V. Virkar & D. R. Clarke. *J Am Ceram Soc.* **2009**, 92, 1901-1920.
[6] T. Onda, S. Iwagaki, S. Morito & M. Hayakawa. *Mater Trans.* **2010**, 51, 899-905.
[7] Easterli.Ke & P. R. Swann. *Acta Metallurgica.* **1971**, 19, 117-&.
[8] S. M. Ueland & C. A. Schuh. *J Appl Phys.* **2013**, 114.
[9] N. K. Simha. *J Mech Phys Solids.* **1997**, 45, 261-&.
[10] A. Isalgue, V. Torra, A. Yawny & F. C. Lovey. *J Therm Anal Calorim.* **2008**, 91, 991-998.
[11] S. Miyazaki & K. Otsuka. *Isij Int.* **1989**, 29, 353-377.
[12] S. Miyazaki & A. Ishida. *Mat Sci Eng a-Struct.* **1999**, 273, 106-133.
[13] K. Otsuka & X. B. Ren. *Intermetallics.* **1999**, 7, 511-528.
[14] H. Y. Kim, Y. Ikehara, J. I. Kim, H. Hosoda & S. Miyazaki. *Acta Mater.* **2006**, 54, 2419-2429.
[15] Y. Tanaka, Y. Himuro, R. Kainuma, Y. Sutou, T. Omori & K. Ishida. *Science.* **2010**, 327, 1488-1490.
[16] J. San Juan, M. L. No & C. A. Schuh. *Nat Nanotechnol.* **2009**, 4, 415-419.
[17] G. Subhash & S. Nematnasser. *J Am Ceram Soc.* **1993**, 76, 153-165.
[18] P. E. Reyesmorel, J. S. Cherng & I. W. Chen. *J Am Ceram Soc.* **1988**, 71, 648-657.
[19] M. I & H. Xu. *Acta Metall Mater.* **1991**, 39, 263-271.

Chapter 7

Thermodynamics of Shape Memory Effect*

In shape memory ceramics, understanding of the control parameters for the characteristic shape memory properties is based on their underlying mechanism of stress-induced martensitic transformation. The occurrence of martensitic transformation is determined by the Gibbs energy change during transformation, which includes change in the chemical energy, surface energy, strain energy and externally applied energy. Therefore, the deformation behaviour of the YTDZ ceramics should be directly linked to these energies, which are controlled by the crystal orientation, ceramic composition, matrix constraint, ceramic dimensions and testing temperature. In this chapter, we will systematically explore the effects of these parameters on the characteristic shape memory properties for YTDZ ceramics, with the aim to establish the relationship between property and structure for shape memory ceramics.

*The content of this chapter was published in article:

Xiao Mei Zeng, Alan Lai, Zehui Du, Christopher A Schuh, Chee Lip Gan, Crystal orientation dependence of stress-induced martensitic transformation in shape memory zirconia. Acta Materialia, 116, 124-135, 2016

7.1 Free Energy for Martensitic Transformation

The martensitic transformation from tetragonal to monoclinic phase occurs by shearing one of the tetragonal faces along one of the four directions, resulting in 12 possible variants. According to Becher[1], the free energy change ($\Delta G_{t\to m}$) of stress-induced martensitic transformation is composed of changes in chemical free energy ΔG^c, strain energy ΔU_e, surface energy ΔU_s and externally applied energy ΔU_{ex}, and is described as[1]:

$$\Delta G_{t\to m} = -\Delta G^c + \Delta U_e + \Delta U_s - \Delta U_{ex} \qquad \text{Equation 10}$$

The chemical free energy ΔG^c is dependent on the temperature and composition as:

$$\Delta G^c = \Delta S^{t\to m}(T_o - T) = \frac{\Delta H^{t\to m}(T_o - T)}{T_0} \qquad \text{Equation 11}$$

where $\Delta S^{t\to m}$ and $\Delta H^{t\to m}$ are the change in transformation entropy and enthalpy per unit volume, respectively, which are determined by the material composition, T is the testing temperature, and T_0 is the equilibrium transformation temperature for tetragonal zirconia. The strain energy change ΔU_e represents the elastic energy that is stored in the bulk region, in and around the transformed zone. The surface energy change ΔU_s is the change in energy associated with the surface during transformation. The externally applied energy for the stress-induced transformation is

$$\Delta U_{ex} = \tau_{trans}\Delta\varepsilon \qquad \text{Equation 12}$$

whereas τ_{trans} is the transformation shear stress and $\Delta\varepsilon$ is the volumetric transformation strain. For transformation to occur, the following equation should be satisfied:

$$\Delta G_{t\to m} = -\frac{\Delta H^{t\to m}(T_o - T)}{T_0} + \Delta U_e + \Delta U_s - \tau_{trans}\Delta\varepsilon \le 0 \qquad \text{Equation13}$$

Therefore, for stress-induced martensitic transformation in zirconia, the transformation shear stress τ_{trans} is dependent on ceramic composition, matrix constraint, surface energy change and volumetric transformation strain, which can be expressed as:

$$\sigma_{trans} \ge \frac{-\Delta H^{t\to m}(T_o - T) + \Delta U_e + \Delta U_s}{\Delta\varepsilon \cdot T_o} \qquad \text{Equation 14}$$

The martensitic transformation shear stress is defined along the shear plane during the transformation. However, depending on how the applied compressive stress is

resolved onto the transformation shear planes, the critical transformation stress in the compression axis could vary significantly. The relationship can be explained using the analysis of Schmid factor (SF)[2], which is highly crystal orientation dependent. The transformation from tetragonal to monoclinic zirconia occurs by shearing one of the tetragonal faces in the direction of one of the tetragonal basis vectors and this combination of shear plane and shear direction can be used to calculate the Schmid factor for all of the 12 possible monoclinic variants. The required transformation stress to be applied in the compression axis (σ_{comp}) is related to the transformation shear stress (τ_{trans}) through Schmid factor[2]:

$$\sigma_{comp} = \frac{\tau_{trans}}{Schmid\ Factor} = \frac{\tau_{trans}}{cos\chi \cdot cos\lambda} = \frac{-\Delta H^{t\to m}(T_o - T) + \Delta U_e + \Delta U_s}{cos\chi \cdot cos\lambda \cdot \Delta\varepsilon \cdot T_o} \quad \text{Equation 15}$$

where χ is the angle between the shear plane and the compression axis and λ is the angle between the shear direction and the compression axis; $SF = cos\chi \cdot cos\lambda$ is the Schmid factor. The relationship can be directly derived from Figure 7.1. $cos\lambda$ represents the magnitude of resolved unit force vector in the shear direction, whereas $cos\chi$ accounts for the change in area to calculate the stress from resolved force vector.

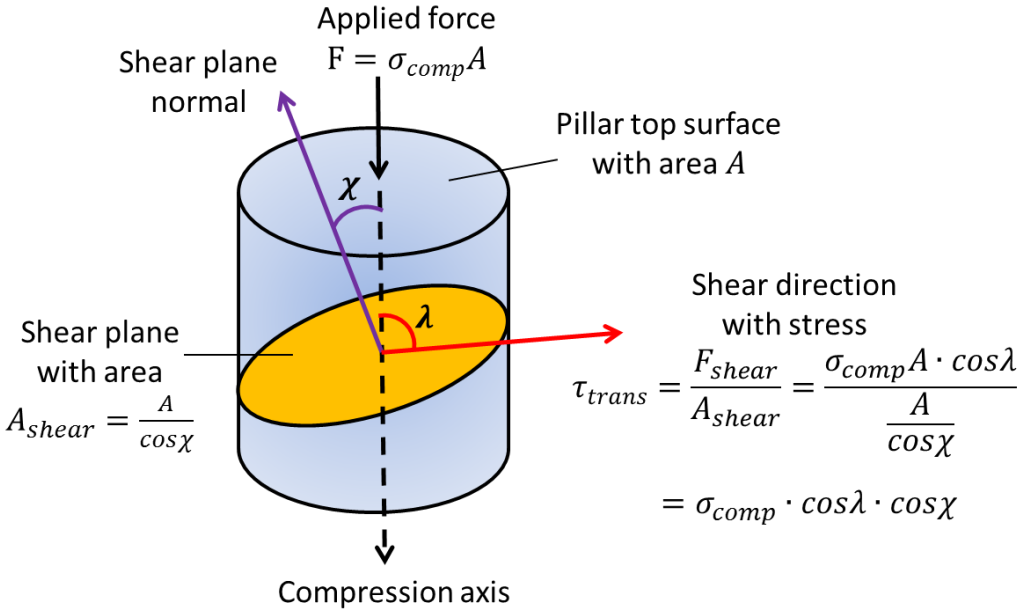

Figure 7.1 Schematic illustration of relationship between applied stress in compression axis (σ_{comp}), the transformation shear stress ((τ_{trans}) and Schmid factor ($cos\chi \cdot cos\lambda$) during compression of a pillar.

For microscale YTDZ pillars, ΔU_e is expected to be very small since there is limited bulk material to store elastic energy and mismatch strains are accommodated at free surfaces. The value for volumetric transformation strain ($\Delta\varepsilon$) can be determined from the crystallography of the transformation. In yttria stabilized zirconia, $\Delta\varepsilon$ has been reported as 4%, by Becher[1]. Therefore, Equation 15 can be rephrased as:

$$\sigma_{comp} = \frac{-\Delta H^{t\to m}(T_o - T) + \Delta U_e + \Delta U_s}{SF \cdot \Delta\varepsilon \cdot T_o} \qquad \text{Equation 16}$$

The critical stress for transformation in compression axis is therefore dependent on the crystalline orientation (SF), composition ($\Delta H^{t\to m}$, T_o), test temperature (T) and pillar size (ΔU_s). The effect of the four parameters will be discussed one by one in this chapter.

For zirconia with composition of $2Y_2O_3$-$5TiO_2$-ZrO_2, which will be studied in this chapter, the transformation enthalpy ($\Delta H^{t\to m}$) has been calculated to be 0.1 kJ/cm^3 in section 5.1, and the transformation temperature (T_o) is around 700K as discussed in section 6.3.2. The transformation strain ($\Delta\varepsilon$) is a constant of 16.4% as reported by Chevalier *et. al*[3]. These values will be used to calculate the transformation stress in the following sections. The remaining three variables of ΔU_s, SF, T will be determined experimentally to calculate the transformation stress.

7.2 Crystal Orientation Dependence of Shape Memory Effect

In order to explore the orientation dependence of martensitic transformation, dozens of pillars with same elemental composition ($2Y_2O_3$-$5TiO_2$-ZrO_2), same phase (tetragonal), similar size (1 μm×3~4 μm) but different crystalline orientations were prepared. The pillar dimensions and orientation are listed in Table 7.1.

Table 7.1 Dimensions and orientations of all the pillars in this work.

Pillar Number	Pillar Dimensions		Orientation (hkl)			Orientation (Euler Angles)		
	Diameter (μm)	Height (μm)	h	k	l	E1	E2	E3
1	1.24	4.58	0.56	0.04	0.82	284.7	44.6	319.0
2	1.23	3.85	0.47	0.88	0.07	177.1	92.2	17.5
3	1.18	3.51	0.43	0.07	0.90	3.1	145.8	305.8

5	1.18	3.25	0.58	0.10	0.81	194.3	46.4	234.6
6	1.17	3.54	0.46	0.14	0.87	83.8	141.5	118.4
8	1.19	3.38	0.16	0.13	0.98	183.0	161.9	172.0
18	1.17	3.35	0.72	0.21	0.66	53.1	121.5	298.8
20	1.17	3.32	0.79	0.20	0.59	75.0	116.6	300.9
21	1.17	3.19	0.14	0.40	0.91	249.6	33.9	205.5
23	1.17	3.22	0.75	0.17	0.64	257.9	60.2	147.4
26	1.17	3.81	0.19	0.37	0.91	245.1	32.8	197.4
30	1.18	3.32	0.67	0.53	0.52	135.4	113.4	0.3
34	1.17	3.35	0.60	0.45	0.66	300.0	59.3	352.2
35	1.17	3.45	0.65	0.48	0.59	99.2	117.1	351.2
38	1.18	3.62	0.39	0.71	0.58	264.8	63.3	16.4
39	1.18	3.38	0.52	0.51	0.68	261.9	45.0	179.0
40	1.17	3.70	0.79	0.15	0.60	97.3	117.5	359.2
41	1.17	3.60	0.93	0.17	0.33	67.5	103.8	304.9
42	1.18	3.75	0.11	0.72	0.68	186.7	57.0	234.1
4	1.17	3.62	0.18	0.06	0.98	232.5	15.4	296.3
12	1.16	2.66	0.73	0.64	0.26	72.5	100.6	356.7
17	1.19	3.60	0.12	0.90	0.42	243.0	72.1	52.6
22	1.17	3.63	0.34	0.92	0.19	105.2	97.5	384.5
24	1.14	3.62	0.07	0.08	0.99	157.4	8.8	184.6
25	1.12	3.46	0.14	0.16	0.98	184.8	16.8	183.7
37	1.19	3.65	0.41	0.40	0.82	91.4	103.7	353.4

The corresponding micro-compression data was gathered from the pillars with different crystal orientations. Among all the indented pillars, Figure 7.2 shows the pillars with signatures of martensitic transformation. Their orientations are plotted on the 001 tetragonal reduced inverse pole figure together with the associated load-displacement curves. Each position on the inverse pole figure represents a different orientation of the tetragonal crystal. A diverse deformation response is observed; with the magnitude of displacement and the critical load for transformation varying with orientations. The critical load for transformation varies from 0.7 to 3 mN, while the plateau displacement ranges from 50 to 200 nm.

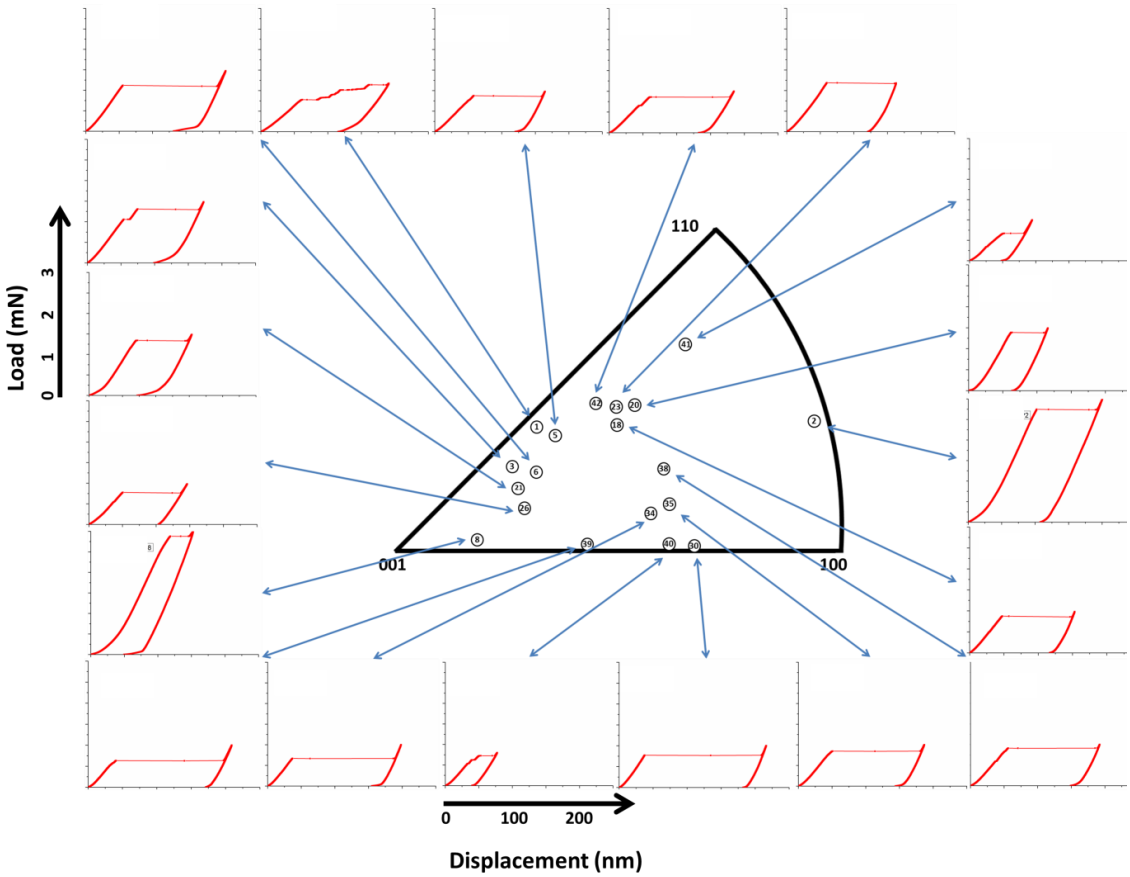

Figure 7.2 Load-displacement curves of YTDZ pillars that went through martensitic transformation, and their crystal orientations on the 001 tetragonal reduced inverse pole figure.

In contrast to pillars that transformed, some pillars do not show any displacement plateau before they fractured, and the corresponding load-displacement curves are also plotted on the 001 tetragonal reduced inverse pole figure in Figure 7.3. Besides those pillars that directly fractured, some pillars went through a displacement plateau before fracture, but the critical load for plateau is very close to the fracture load. As in these cases, it is difficult to exam the surface morphology of the fractured pillars, thus we cannot be sure whether the plateau is due to the martensitic transformation or permanent plastic deformation. Therefore, they are not included in subsequent analysis for transformation stress and transformation strain. The pillars that fractured tend to locate close to the (001) and (100) plane. A symmetric theory explaining the phenomenon based on the difference in the crystal orientation is presented in subsequent sections.

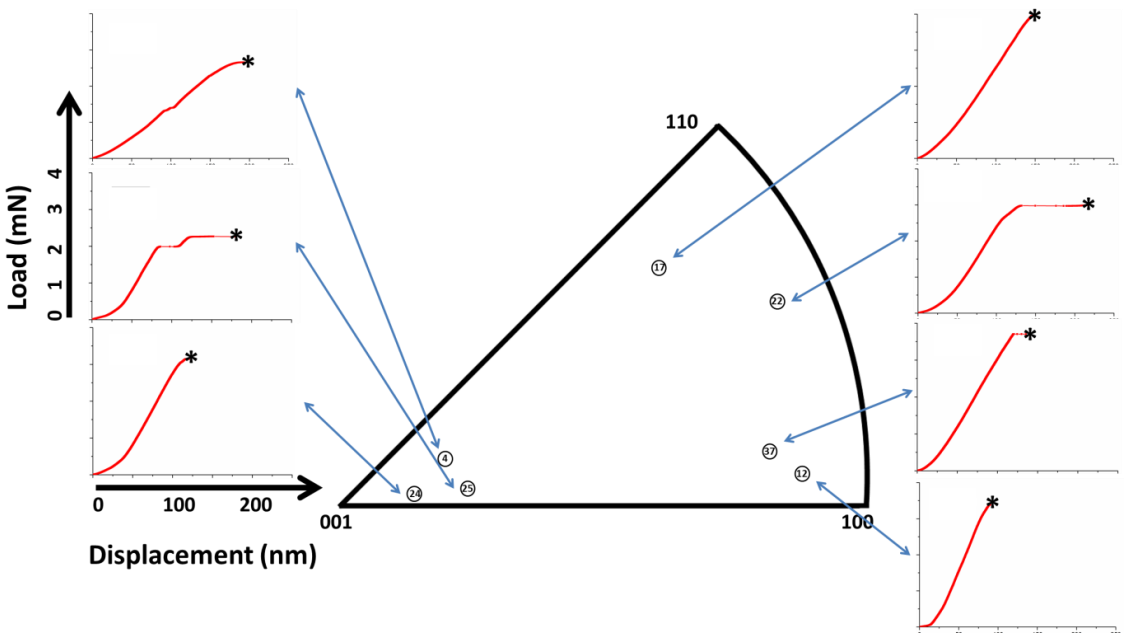

Figure 7.3 Load-displacement curves of YTDZ pillars that fractured, and their crystal orientations on the 001 tetragonal reduced inverse pole figure.

The experimentally measured loading modulus, transformations stresses and transformation strain of the micro-pillars varied substantially across all orientations, which are summarized in Table 7.2.

Table 7.2 Table of transformation percentage, critical transformation stress, transformation strain, loading modulus and dissipated energy of dozens of pillars of various crystal orientations obtained from the load-displacement curves.

Pillar Number	Transformation Percentage (f_{trans})	Loading Modulus (GPa) Experiment	Theory	Transformation Stress (GPa)	Transformation Strain (%)	Dissipated Energy (MJ/m^3)
1	87	58.9	168.5	0.65	2.99	18.35
2	69	136.8	286.6	2.32	3.34	63.31
3	75	70.0	176.5	1.20	3.60	37.47
5	65	52.3	169.0	0.81	3.93	33.12
6	100	77.4	172.2	1.04	4.25	33.27
8	47	102.7	211.6	2.60	1.53	72.63
18	68	67.3	164.7	0.81	4.25	29.99
20	49	87.9	193.3	1.30	3.02	34.66
21	51	76.1	174.8	1.24	4.60	49.17
23	86	69.1	188.4	1.11	3.68	33.93
26	50	66.7	175.8	0.71	4.59	26.88
30	84	78.7	171.8	0.71	6.21	34.13
34	76	72.5	169.8	0.62	6.48	29.40
35	76	69.3	197.9	0.78	5.47	32.35
38	74	68.5	201.9	0.83	5.46	33.95
39	79	60.6	170.5	0.58	6.30	27.30
40	28	70.3	198.2	0.67	2.22	17.54
41	49	55.6	214.2	0.62	1.81	11.98
42	71	80.0	184.73	0.78	4.79	29.45
4	Fractured	75.4	218.9	2.46	/	/
12	Fractured	145.4	235.0	3.18	/	/
17	Fractured	78.1	195.8	3.57	/	/
22	Fractured	129.5	249.1	2.76	/	/
24	Fractured	156.2	236.1	3.10	/	/
25	Fractured	124.5	215.3	2.29	/	/
37	Fractured	132.0	254.0	3.61	/	/

7.2.1 Crystal orientation dependence of elastic modulus

The experimentally measured Young's modulus of tetragonal pillar is obtained from the slope of elastic region of loading cycle on the load-displacement curve in Figure 7.2, as well as based on the pillar dimensions in Table 7.1.

According to Sneddon[4], the diamond tip and the zirconia substrate can be considered as elastic half space during the nanoindentation of cylinder pillars. The measured indentation depth Δh includes all the elastic deformation from the tip, pillar and substrate, and is calculated based on the following equation[5]:

$$\Delta h = \Delta h_{pillar} + \Delta h_{tip} + \Delta h_{substrate} \quad \text{Equation 17}$$

where Δh_{pillar} is the actual deformation of the pillar; Δh_{tip} and $\Delta h_{substrate}$ are the elastic deformation of diamond tip and zirconia substrate, respectively. The compliance of half space elastic tip (S_{tip}) and substrate ($S_{substrate}$) are calculated as:

$$S_{tip} = \frac{(1-\nu_{tip}{}^2)\sqrt{\pi}}{2E_{tip}\sqrt{A_{contact}}} = \frac{(1-\nu_{tip}{}^2)\sqrt{\pi}}{2E_{tip}\sqrt{\frac{\pi d_{top}{}^2}{4}}} = \frac{(1-\nu_{tip}{}^2)}{E_{tip}d_{top}} \qquad \text{Equation 18}$$

and similarly $S_{substrate} = \frac{(1-\nu_{substrate}{}^2)}{E_{substrate}d_{bottom}}$; Equation 19

where ν_{tip} and $\nu_{substrate}$ are the Poisson's ratio of tip (diamond) and substrate; E_{tip} and $E_{substrate}$ are the Young's modulus of tip and polycrystalline zirconia substrate; $A_{contact}$ is the contact area between tip-pillar or pillar-substrate in Equation 18 and 19, respectively; d_{top} and d_{bottom} are the diameter of pillar at the top and bottom, respectively. Therefore, Δh_{tip} and $\Delta h_{substrate}$ are calculated to be:

$$\Delta h_{tip} = S_{tip}F = \frac{(1-\nu_{tip}{}^2)F}{E_{tip}d_{top}} \qquad \text{Equation 20}$$

and similarly $\Delta h_{substrate} = \frac{(1-\nu^2)F}{E_{substrate}d_{bottom}}$; Equation 21

where F is the applied compressive load. Therefore the actual pillar displacement is:

$$\Delta h_{pillar} = \Delta h - \frac{(1-\nu^2)F}{E_{tip}d_{top}} - \frac{(1-\nu_{substrate}{}^2)F}{E_{substrate}d_{bottom}} \qquad \text{Equation 22}$$

The Young's modulus of tetragonal pillar (E_{pillar}) is thus given by the following relationship[5]:

$$E_{pillar} = \frac{\sigma_{pillar}}{\varepsilon_{pillar}} = \frac{4FH_{pillar}}{\pi\Delta h_{pillar}(\frac{d_{top}{}^2+d_{top}d_{bottom}+d_{bottom}{}^2}{3})} \qquad \text{Equation 23}$$

The theoretically expected Young's modulus of a single crystal can be found from the compliance tensor using the elastic constants of the material.

For the theoretical prediction, the x, y, z are denoted by 1, 2, 3, and the unprimed symbols are used to differentiate the pillar crystal axis system from the laboratory axis system. According to Nye[6], both the stress and strain are second-rank tensors and they are related as:

$$\varepsilon'_{33} = s'_{3333}\sigma'_{33} \qquad \text{Equation 24}$$

where σ'_{33} is the applied stress in z-axis, ε'_{33} is the measured strain in z-axis, and s'_{3333} is the corresponding compliance. Finding the compliance of a given orientation is done by rotating the standard compliance tensor into the specified crystal frame using the full Einstein tensor notation, where the a_{ij} terms represent the components of a rotation matrix. The compliance is related to the single crystal elastic compliances s_{mnop} according to the transformation law of [6]:

$$s'_{3333} = a_{3m}a_{3n}a_{3o}a_{3p}s_{mnop} \quad (m,n,o,p = 1,2,3) \qquad \text{Equation 25}$$

By taking abbreviation and applying the tetragonal crystal symmetry, s'_{3333} can be expressed as:

$$s'_{3333} = \frac{1}{E_{33}} = (a_{31}{}^4 + a_{32}{}^4)s_{11} + \left(2a_{31}{}^2a_{32}{}^2\right)s_{12} + \left(2a_{31}{}^2a_{33}{}^2 + 2a_{32}{}^2a_{33}{}^2\right)s_{13} + (a_{33}{}^4)s_{33} + (a_{32}{}^2a_{33}{}^2 + a_{31}{}^2a_{33}{}^2)s_{44} + (a_{31}{}^2a_{32}{}^2)s_{66} \qquad \text{Equation 26}$$

where a_{ij} can be calculated according to the Euler angle $(\phi\theta\psi)$:

$$a_{ij} = \begin{bmatrix} a_{11} & a_{12} & a_{13} \\ a_{21} & a_{22} & a_{23} \\ a_{31} & a_{32} & a_{33} \end{bmatrix} = \begin{bmatrix} c\psi & s\psi & 0 \\ -s\psi & c\psi & 0 \\ 0 & 0 & 1 \end{bmatrix}\begin{bmatrix} 1 & 0 & 0 \\ 0 & c\theta & s\theta \\ 0 & -s\theta & c\theta \end{bmatrix}\begin{bmatrix} c\phi & s\phi & 0 \\ -s\phi & c\phi & 0 \\ 0 & 0 & 1 \end{bmatrix} = \begin{bmatrix} c\psi c\phi - s\psi c\theta s\phi & c\psi s\phi + s\psi c\theta c\phi & s\psi s\theta \\ -s\psi c\phi - c\psi c\theta s\phi & -s\psi s\phi + c\psi c\theta c\phi & c\psi s\theta \\ s\theta s\phi & -s\theta c\phi & c\theta \end{bmatrix} \qquad \text{Equation 27}$$

Therefore, the Young's modulus of tetragonal zirconia E_{33} can be calculated for various orientations (ϕθψ), taking the compliances $s_{11}, s_{33}, s_{44}, s_{66}, s_{12}, s_{13}$ according to Kisi[7].

Both the experimental and theoretical moduli of tetragonal zirconia are plotted in Figure 7.4. The dashed blue line represents the ideal case of equality between experimental and theoretical values, whereas the dashed black line is a rough linear estimation on the experimental value.

The theoretical prediction varies from 164.7 to 286.6 GPa, with an average of 200.6 GPa. The average modulus is very close to the Young's modulus of polycrystalline tetragonal zirconia of 192 GPa reported in literature[7], The experimentally measured modulus has an average of 90.1 GPa and ranges from 67.3 to 136.8 GPa. The measured modulus seems to follow a similar ascending trend as the theoretical prediction, but with a significantly lower magnitude and some noise. While the measured modulus is reasonably correlated with the theoretical value, there is better quantitative agreement at

higher moduli. We attribute the experimental variation to several aspects of the micro-compression testing such as substrate and tip compliance, minor misalignments, indentation compliance at the point of contact of the tip; these are all known deficiencies of microcompression testing and the present apparently high compliance is in line with results from the field on other materials[7].

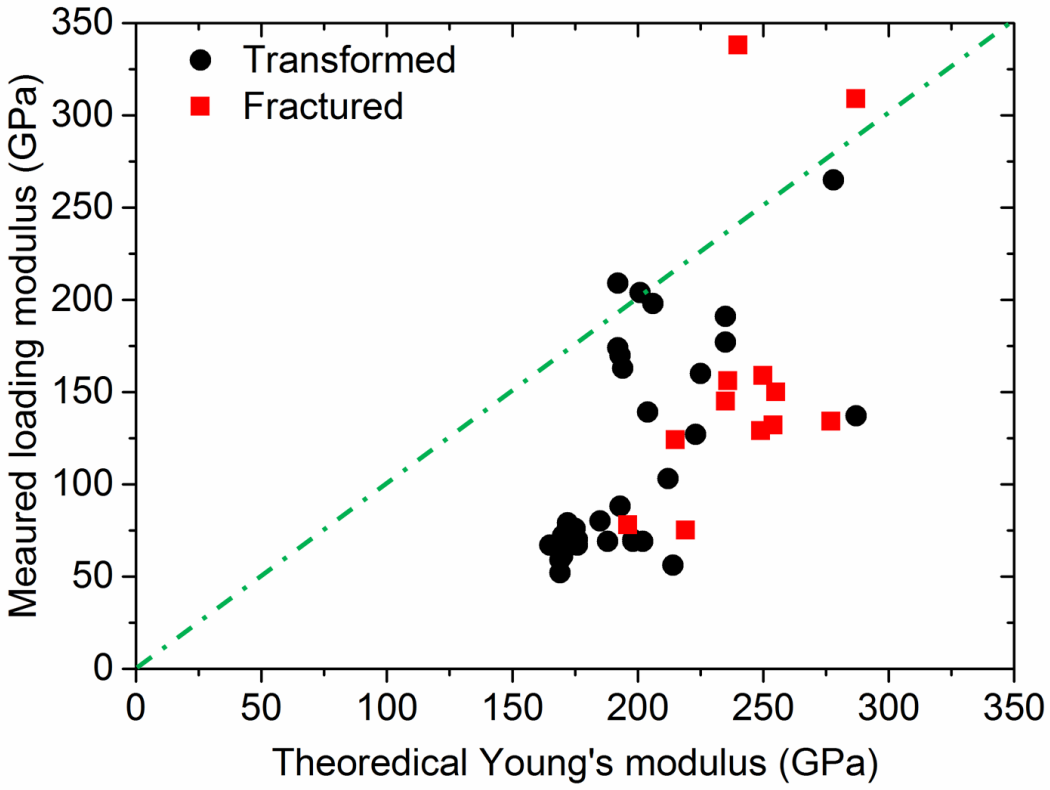

Figure 7.4 The correlation between theoretical and measured Young's modulus of tetragonal zirconia for all the pillars.

The experimentally obtained Young's modulus of tetragonal pillars was plotted in the tetragonal 001 inverse pole figure, as shown in Figure 7.5. As expected, the loading modulus is highly anisotropic. Pillars with orientations close to (111) and (101) have much lower moduli of between 50 to 90 GPa, as compared to pillars close to (001) and (100) which have much higher moduli, for both transformation and fractured pillars.

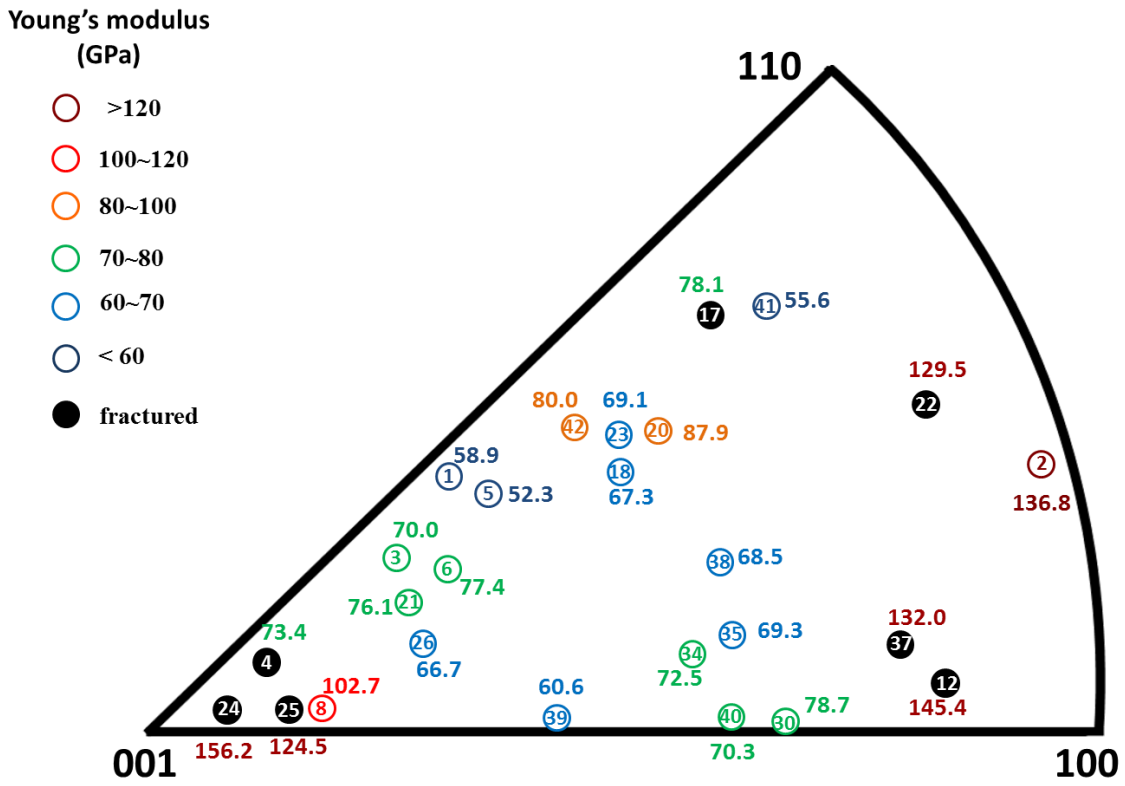

Figure 7.5 The measured Young's modulus of tetragonal pillars in the tetragonal 001 inverse pole figure. The open circles indicate pillars that transformed without breaking, black solid dots indicate pillars that did not transform or broke without transforming.

It is to be noted that for all the tested pillars, the unloading modulus is higher than the loading modulus, which seems contradictory to the literature that Young's modulus of monoclinic zirconia is smaller than that of tetragonal phase for polycrystal zirconia[8]. In the case of single crystal pillars shown here, the comparison between the loading modulus and unloading modulus cannot be solely based on the difference between the modulus of the tetragonal and monoclinic phase. After the compression, the single crystal pillar experienced a partial transformation (which will be discussed in detail in section 7.2.2), resulting in a pillar consisting a mixture of tetragonal and monoclinic crystals under maximum loading. Therefore, the unloading modulus reflects the elastic behavior of a mixed crystal consisting both monoclinic and tetragonal phase, rather than just the monoclinic phase. The author believes that it is possible that the unloading modulus is higher than the loading modulus due to the pinning effect of structure defects such as

interface and dislocations formed in the pillars after compression. Such finding has been recently reported by Du. et al.[9].

7.2.2 Crystal orientation dependence of transformation stress

Since the compression tests were all carried out at room temperature on pillars with same chemical composition and similar size, $\Delta S^{t\to m}$, T_0, ΔU_e, ΔU_s and T in Equation 16 can be assumed to be constant, though the exact value of $\Delta S^{t\to m}$,ΔU_e, ΔU_s, T_0 are difficult to determine for micro-pillars as it involves the surface energy of pillars. Therefore, $\sigma comp = \frac{-\Delta H^{t\to m}(T_o - T)+\Delta U_e+\Delta U_s}{SF\cdot\Delta\varepsilon\cdot T_o}$ Equation 16 can be rewritten as

$$\sigma_{comp} = \frac{-\Delta S^{t\to m}(T_o - T)+\Delta U_e+\Delta U_s}{cos\chi * cos\lambda * \Delta\varepsilon} = \frac{A}{cos\chi * cos\lambda} = \frac{A}{SF} \quad \text{Equation 28}$$

where $A = \frac{-\Delta S^{t\to m}(T_o - T)+\Delta U_e+\Delta U_s}{\Delta\varepsilon} = \frac{0.1\cdot(700-298)+\Delta U_e+\Delta U_s}{0.164\cdot 700} = 0.35 + \frac{\Delta U_e+\Delta U_s}{114.8}$.

The measured transformation stress ($\sigma_{comp,meas}$) in actual compression test should be the lowest possible σ_{comp}, meaning that the variant with the largest Schmid Factor (SF_{max}) is always preferred. The measured transformation stress of certain orientation can be expressed as,

$$\sigma_{comp,meas} \geq \left(\sigma_{comp}\right)_{min} = A \cdot \frac{1}{(cos\chi * cos\lambda)_{max}} = A \cdot \frac{1}{SF_{max}} \quad \text{Equation 29}$$

This equation suggests that, in theory, the measured transformation stress should be linearly related to $SF_{max}{}^{-1}$, and its orientation dependence can be studied indirectly with Schmid Factor.

The theoretical calculation of maximum inverse of Schmid factor ($SF_{max}{}^{-1}$) is done in collaboration with Mr. Alan Lai from MIT* and will not be discussed here. The discussion has been published in a paper accepted for publication in Acta Materialia.

Figure 7.6 graphically presents the measured critical transformation stress ($\sigma_{comp,meas}$) for pillars with various orientations in the tetragonal 001 inverse pole figure,

* Alan Lai is a collaborator for the work of orientation dependence on shape memory effect in YTDZ pillars.

together with the measured fracture stress for pillars that fractured. It is clear that the transformation stress is highly orientation dependent. Those pillars that transformed at stress lower than 1 GPa tend to be located in orientations close to (101). The critical stress increases when their orientation get closer to (110) and (111) planes. The fractured pillars are most likely to be observed for orientations near (001) and (100).

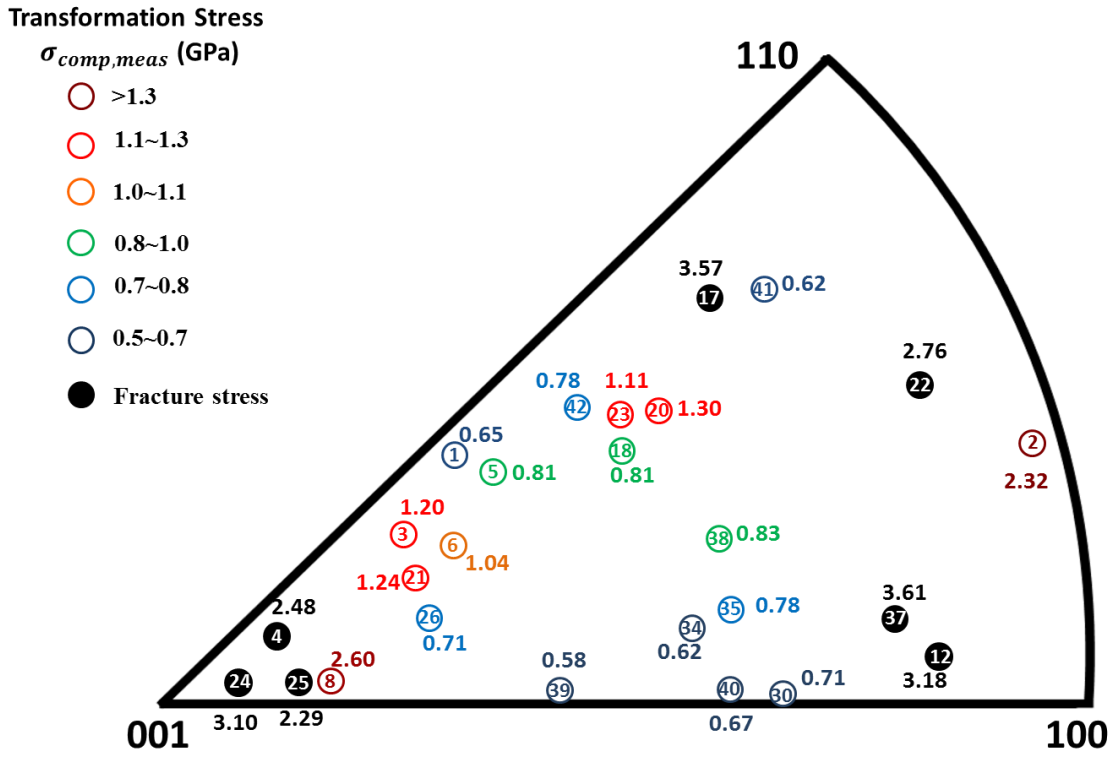

Figure 7.6 The experimentally measured transformation stress ($\sigma_{comp,meas}$) of pillars in the tetragonal 001 inverse pole figure. The open circles indicate pillars that transformed without breaking, black solid dots indicate pillars that did not transform or broke without transforming.

7.2.3 Crystal orientation dependence of transformation strain

A defining feature of the mechanical response of a shape memory material is the strain plateau caused by the rapid phase transformation, and such plateaus are observed in many of the specimens tested in this work. However, observations of the as-compressed single crystal pillars suggested that they are usually partially transformed, and this must be accounted for when carrying out strain calculations as shown in Figure 7.7.

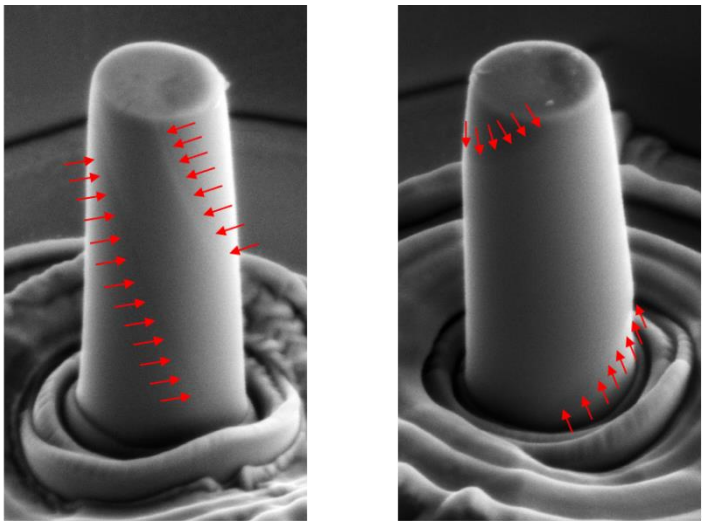

Figure 7.7 Illustration of calculated transformation fraction (f_{trans}) of YTDZ pillars.

Instead of applying the standard strain calculation that uses the original pillar height and assumes full transformation, the transformation strain ($\Delta\varepsilon_{comp,meas}$) is calculated based only on the transformed fraction (f_{trans}) of the as-deformed pillars according to the scanning electron microscopy analysis,

$$\Delta\varepsilon_{trans,meas} = \frac{\Delta h_{plateau,meas}}{f_{trans} \cdot H_{pillar,}} \qquad \text{Equation 30}$$

where $\Delta h_{plateau,meas}$ is the displacement measured in the plateau region.

The experimentally obtained transformation strain is presented in the tetragonal 001 inverse pole figure, as seen in Figure 7.8. There is a large extent of possible strains ranging from 0.58% to 5.17% and the strain is clearly orientation dependent. Most of the pillars have strain in the range of 3% to 4%, which is comparable to shape memory alloys.[10] The transformation strains are found to have quite an opposite trend to the transformation stress. Those pillars that transformed at larger strain tend to be located in orientations close to (101) and (111). The theory of transformation strain can be calculated based on the shape strain or lattice deformation matrix[2]. As been discussed in section 7.1, transformation strain ($\Delta\varepsilon$) in shear direction is a constant of 16.4% as reported by Chevalier *et. al*[3]. The transformation strain in the compressive axis is the

magnitude of resolved transformation strain vector ($\Delta\varepsilon$) in shear direction. The theoretical strain for each pillar is calculated based on the same monoclinic variant as used in transformation stress calculation, both having the maximum inverse of Schmid factor (SF_{max}^{-1}). The detailed theoretical calculation was done in collaboration with Alan Lai from MIT, so the details will not be elaborated here.

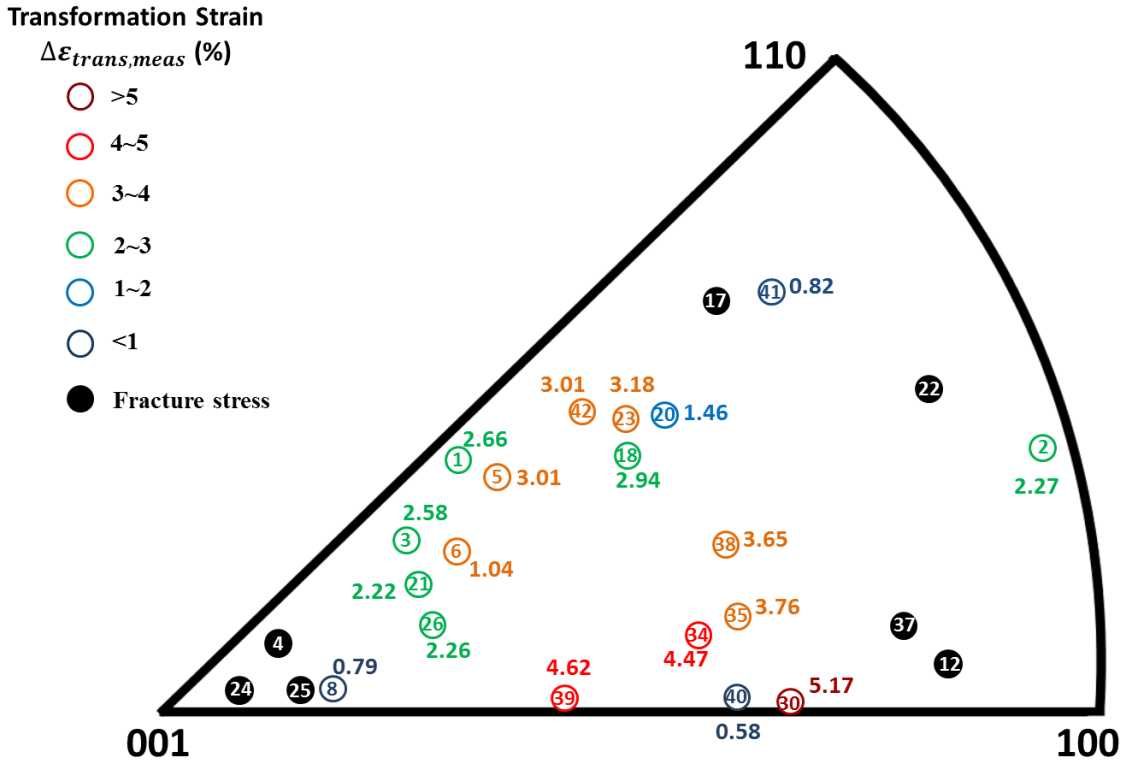

Figure 7.8 The experimentally measured transformation strain ($\Delta\varepsilon_{trans,meas}$) of pillars in the tetragonal 001 inverse pole figure. The open circles indicate pillars that transformed without breaking, black solid dots indicate pillars that did not transform or broke without transforming.

7.2.4 Crystal orientation dependence of energy dissipation

Besides the transformation stress and strain, the capability of the pillars to dissipated energy during compressive loading is another critical property for shape memory ceramics. Experimentally, we estimate the energy dissipation by calculating the area under the load-displacement curves, giving the total energy absorbed during compression. To normalize this value and provide a better comparison across all the

pillars, the total energy was divided by the transformed volume of each pillar to give the energy dissipated per transformed volume. The data, plotted in Figure 7.9 on the 001 inverse pole figure, shows a wide range of energy absorption from 12 - 73 MJ/m^3. The averaged dissipated energy is around 30 MJ/m^3, clustered in the center while the largest values tend to be closer to the edges. The larger dissipated energy reflects a good combination of higher transformation stress and larger transformation strain close to the edges, which can be reflected by Figure 7.6 and 7.8. This could indicate that for certain orientations, additional energy is required to either nucleate the transformation on their surfaces or to pass through those surfaces, potentially making such orientations ideal for energy dissipation applications.

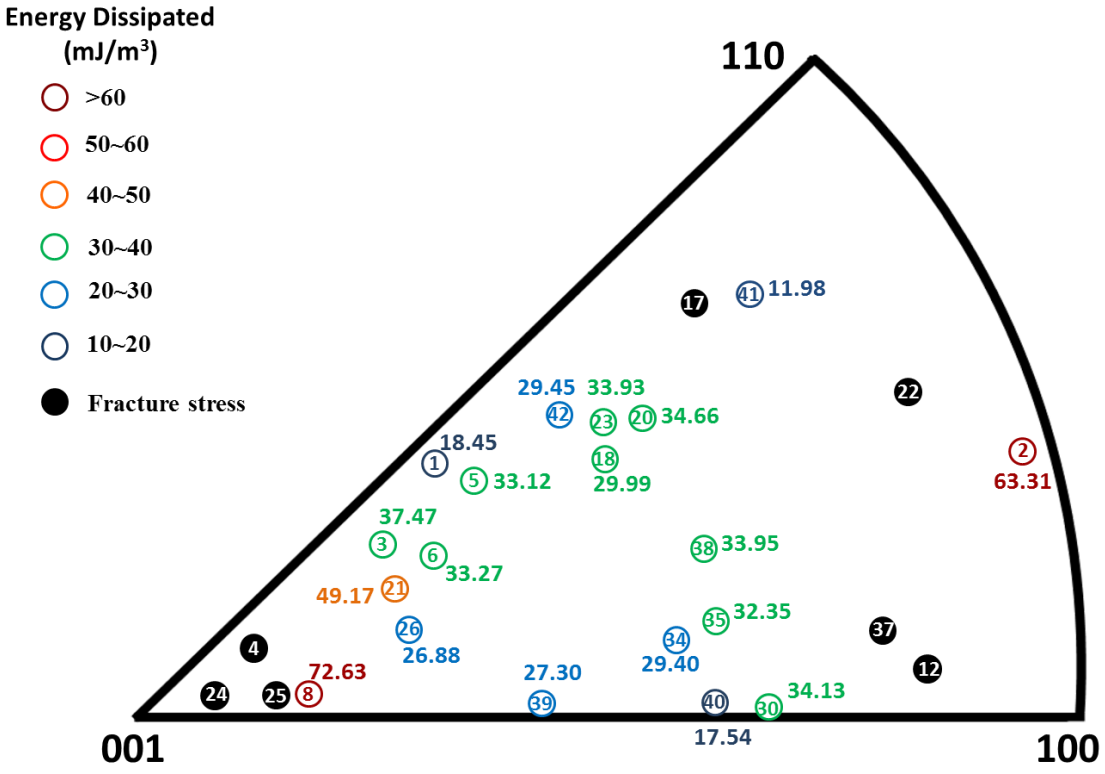

Figure 7.9 The energy dissipated of pillars during compression in the tetragonal 001 inverse pole figure. The open circles indicate pillars that transformed without breaking, black solid dots indicate pillars that did not transform or broke without transforming.

7.3 Temperature Dependence of Shape Memory Effect

According to Equation 14, the martensitic transformation behavior is related to the testing temperature T. Their relationship can be explored by compressing the same pillar at different temperatures, thus the parameters of composition ($\Delta S^{t\to m}$, T_o), pillar size (ΔU_s) and crystalline orientation ($\cos\chi * \cos\lambda$) can be considered as constants, and Equation 16 can be rewritten as:

$$\sigma_{comp} = \frac{-\Delta S^{t\to m}(T_o - T) + \Delta U_e + \Delta U_s}{\cos\chi * \cos\lambda * \Delta\varepsilon} = B \cdot T + C \qquad \text{Equation 31}$$

where constant $B = \frac{\Delta S^{t\to m} \cdot SF_{max}^{-1}}{\Delta\varepsilon} = 8.711 \cdot 10^{-4} \cdot SF_{max}^{-1}$, and constant $C = \frac{-\Delta S^{t\to m} T_o + \Delta U_e + \Delta U_s}{\Delta\varepsilon} \cdot SF_{max}^{-1} = (6.1\Delta U_s + 6.1\,\Delta U_e - 0.61) \cdot SF_{max}^{-1}$. The calculation is based on the values discussed in the last paragraph in section 7.1.

As the slope for transformation stress versus temperature equation is directly controlled by SF_{max}^{-1}, the stress map constructed in section 7.3.3 and Figure 7.6 can be considered as an indication of the slope map for temperature effect, that is how sensitive the stress to temperature it is for various crystal orientations.

In order to justify the relationship predicted by Equation 29, a few pillars with composition of $2Y_2O_3$-$5TiO_2$-ZrO_2 were tested with nanoindenter, to study the martensitic transformation behavior at different temperatures and two pillars (Pillar 13 and Pillar 19) with typical behaviors are reported here. The pillars were compressed at room temperature (25°C) until signatures of martensitic transformation was observed. The indented pillar was imaged to confirm shape deformation, followed by heat treatment at 500°C for 2 hours to enable inverse martensitic transformation and shape recovery, as shown in Figure 7.10(a) and Figure 7.11(a). Once it was confirmed with SEM that the shape was recovered, the pillar was heated up to a higher temperature of 100°C. Similar compressive load was applied again at 100°C to induce another cycle of martensitic transformation. Figure 7.10(b) shows the load-displacement curves of pillar P13 compressed at 25°C and 100°C. The pillar exhibited shape memory effect at 25°C with a transformation load of 0.74 mN and displacement plateau of 760 nm. Significant bending without fracture was observed after the compression. The heat treatment recovered most of the bending. When the pillar was heated and compressed again at 100°C, no transformation plateau was observed until it fractured at 2.05 mN. Such behavior

suggests that the transformation stress for Pillar 13 at 100°C is higher than its fracture strength, and therefore is higher than its transformation stress at 25°C. This observation complies with the analysis of Equation 31, as constant B should be positive and transformation stress should increase with testing temperature.

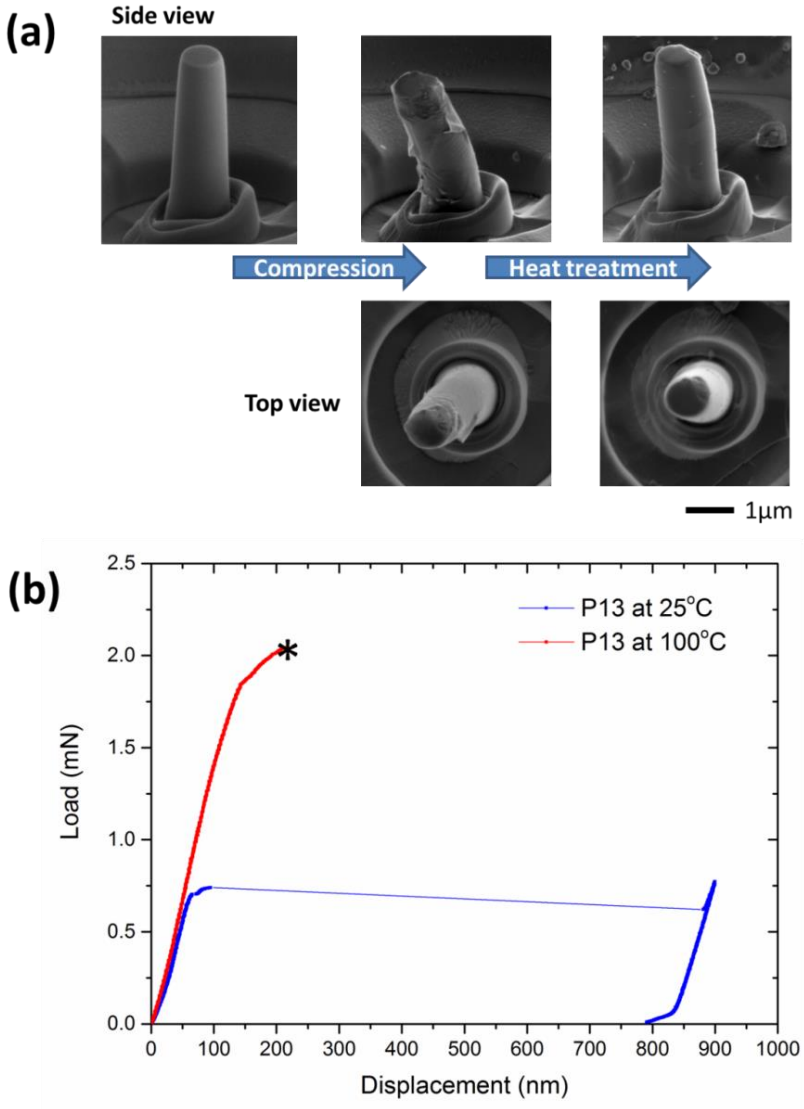

Figure 7.10 (a) FESEM images of P13 ([66.3, 119.3, 266.2]) taken before and after each indentation and heat treatment. (b) The load-displacement behavior of P13 at 25°C and 100°C.

Pillar 19, as shown in Figure 7.11, was tested with similar procedure to Pillar 13. However, this pillar demonstrated similar load-displacement behavior at both 25°C and 100°C, as shown in Figure 7.11(b). The critical load for martensitic transformation at 100°C is 1.1 mN, significantly higher than 0.58 mN at 25°C. The transformation strain

plateau is about 40 nm in displacement for both loading cycles. From the FESEM images taken before and after each micro-compression (Figure 7.11(a)), it is clear that the pillar was not bent or damaged during loading/heating cycles.

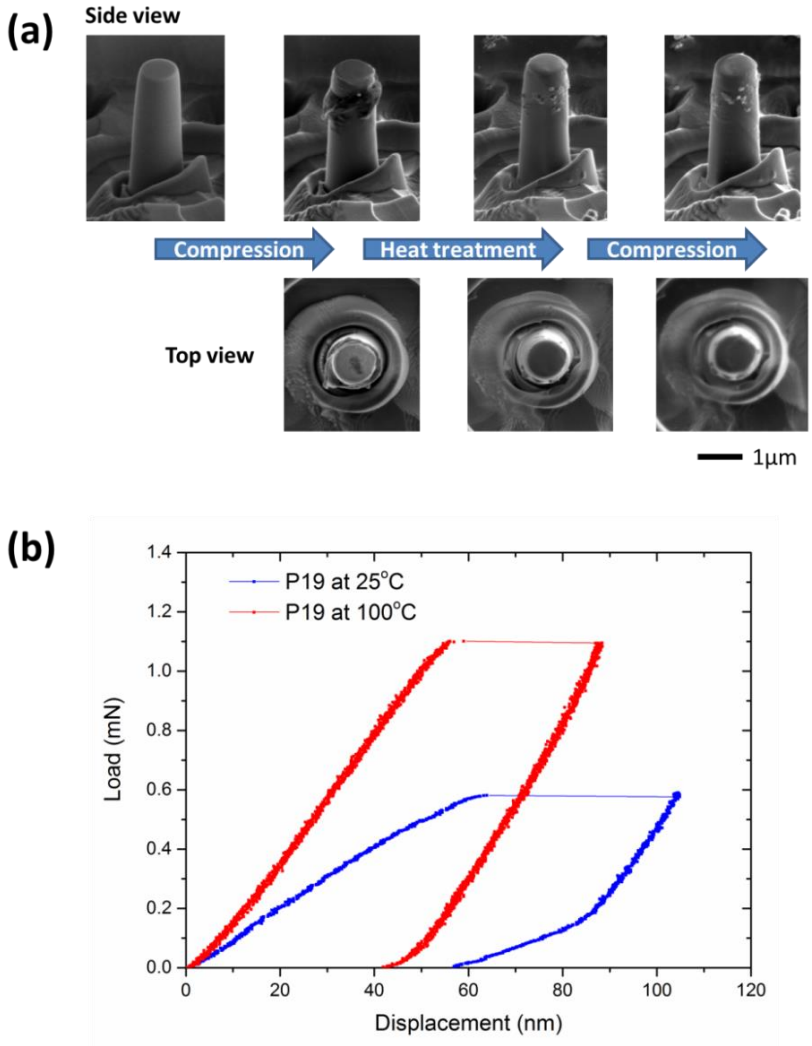

Figure 7.11 (a) FESEM images of P19 ([246.5, 288.8, 290.6]) taken before and after each indentation and heat treatment. (b) The load-displacement behavior of P19 at 25°C and 100°C.

By calculating the critical stress of the P13 and P19 pillars, the stress-temperature relationship is plotted in Figure 7.12. The data follows the rule that the critical stress is larger at higher temperatures. As the $SF_{max}{}^{-1}$ for P13 and P19 are 2.653 and 2.601, respectively, the stress for P13 is expected to be more sensitive to temperature than P19. This complies with the observation that the slope for P13 is higher than P19, which led to fracture of P13 but transformation of P19 at room temperature. It is to be noted that the

actual slope of transformation stress for P13 should be higher than the slope in Figure 7.12 plotted based on fracture stress.

By extracting the plot to intersect with *x* axis, it can be estimated that M_s (martensite starting temperature) is around -75°C. As the XRD pattern has confirmed that the ceramics are fully tetragonal at room temperature, it is in agreement with the estimated M_s temperature. As the fracture stress of pillars could be smaller than 2 GPa, the probability of pillar fracture before reaching the critical transformation stress significantly increases when temperature is higher than 100°C. Pillars with crystal orientations of lower SF_{max}^{-1} are expected to survive higher temperature than those of higher SF_{max}^{-1}.

The two Schmid factors (0.377 and 0.384), which differ by less than 2%, alone does not explain the large difference in the slope in Figure 7.12, some other factors might as well contribute to the difference in behavior of P13 and P19. Clearly P13 experienced bending instead of pure compression, which could affect the martensitic transformation stress and therefore the slope in Figure 7.12. Nevertheless, the behaviors of P13 and P19 both demonstrate that temperature is a critical parameter in controlling the behavior of shape memory ceramics.

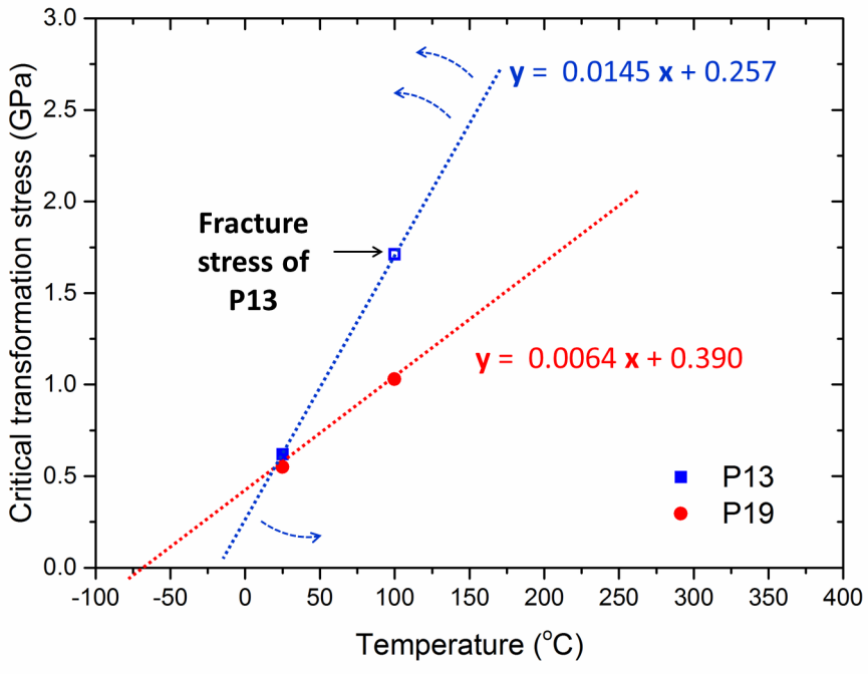

Figure 7.12 The transformation stress as a function of temperatures for YTDZ pillars.

Different from P13 and P19, a few pillars were tested with *in-situ* nanoindenter PI87, where real-time monitoring of shape deformation and recovery was achieved during one heating cycle. For the pillar to transform at higher temperatures, P7 with much smaller SF_{max}^{-1} (2.185), and diameter of 2 μm was heated to 400°C before compression was conducted, as shown in Figure 7.13(a). Large displacement plateau was observed when the pillar was compressed at 400°C (Figure 7.13(b)), with clear stripes seen in the FESEM images. Such stripes disappeared with subsequent heating to 650°C, confirming that martensitic transformation was stress-induced at 400°C and inverse martensitic transformation was thermal-induced between 400°C and 650°C. With *in-situ* nanoindentation, for the first time we directly observed the shape deformation and recovery for pillars with composition of $2Y_2O_3$-$5TiO_2$-ZrO_2.

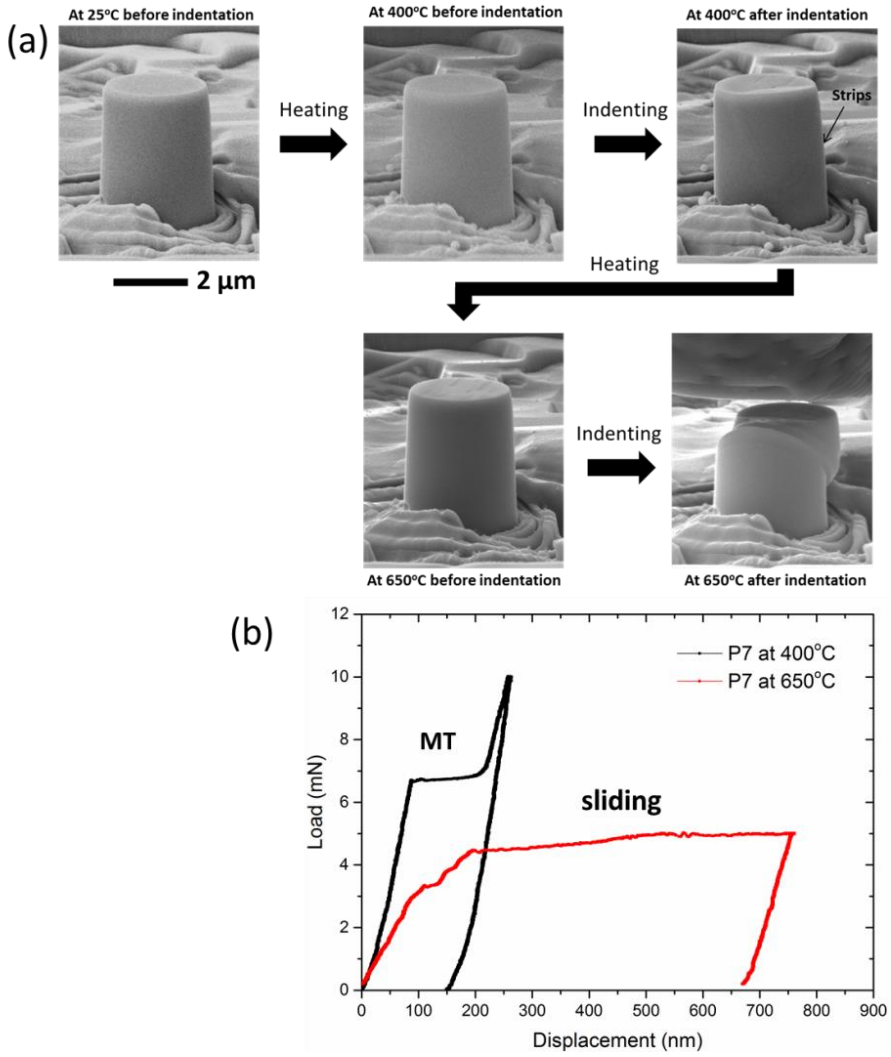

Figure 7.13 (a) FESEM images of P7 ([231.5, 47.4, 23.3]) taken at different temperatures before and after *in-situ* nanoindentation. (b) The load-displacement behavior of P7 at 400^{o}C and 650^{o}C.

Another cycle of nano-compression was conducted on P7 at 650^{o}C, and it is clear from the SEM image that crystal plane slip had occurred, with large plastic deformation observed from the load-displacement curve. It seems that up to 400^{o}C, martensitic transformation is preferred; while at 650^{o}C, plastic slip is preferred.

Similar crystal slip behavior was observed when compressed at 650^{o}C for another pillar (P4) as shown in Figure 7.14. It is very clear from the SEM image that the slip of crystal occurred at an angle of 45^{o}. This observation complies with the Schmid Law that the resolved stress along the plane 45^{o} with respect to the compression axis is the maximum, and it serves as the primary slip plane where the crystal began to plastically deform. Large residual displacements of higher than 700 nm were obtained for both pillars, suggesting that plastic slip can be obtained in traditional brittle ceramic materials at high temperature.

It is to be noted here that, in spite of the fact that the plastic slips within the crystal contribute significantly to the large plastic deformation in single crystal pillars, it should not be confused with the superplasticity property that has been extensively discussed in polycrystalline zirconia. As reported by Wakai et al.[11] and Nieh et al.[12], the superplasticity refers to large plastic deformation that is mainly due to the plastic flow of ultra-fine grains in the polycrystalline fine-grained ceramics. Though both the plastic slip inside single crystal and plastic flow between fine grains could result in large plastic deformation, their origin and working mechanism are very different.

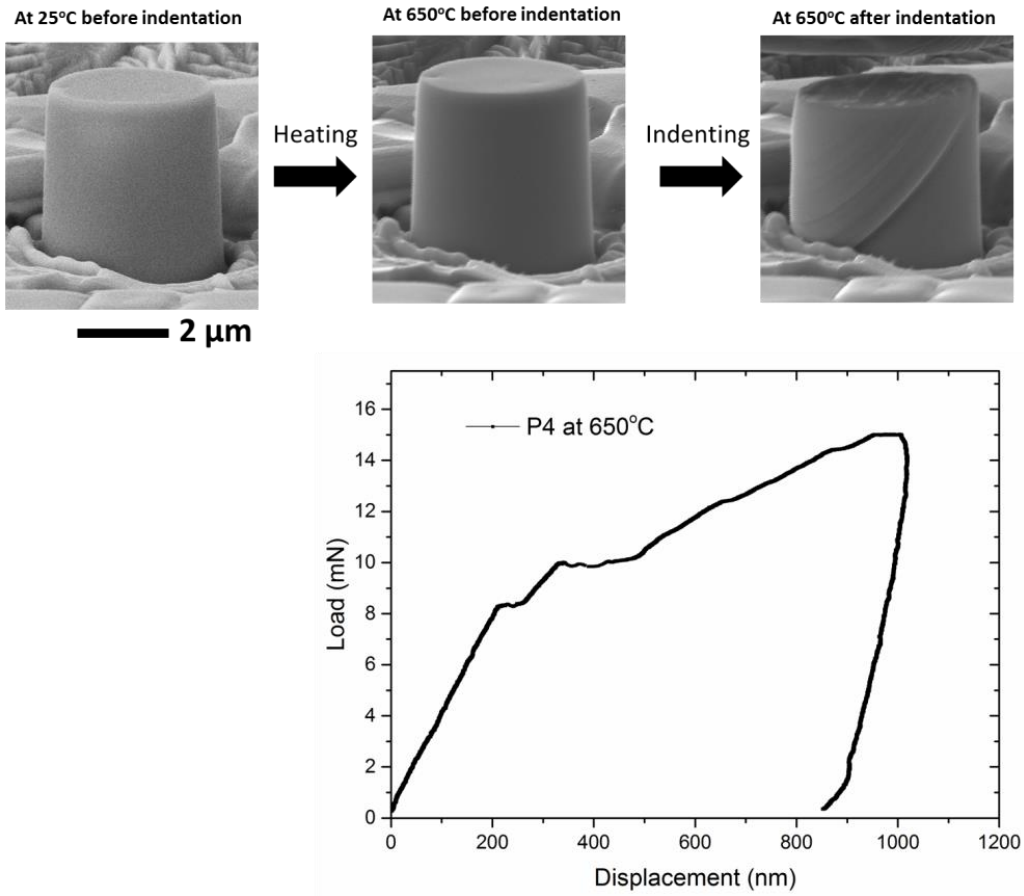

Figure 7.14 FESEM images of P4 taken at different temperatures before and after *in-situ* nanoindentation, and the load-displacement behavior at 650°C.

The *in-situ* study of pillar behaviors at high temperatures can help us identify the upper temperature limit for zirconia ceramics as shape memory materials. The competition between martensitic transformation, crystal slip and fracture during compression determines whether shape memory effect, plastic slip or fracture can be expected. It is clear that temperature plays a key role in determining the crystal behavior under stress, not only in terms of the critical stress for transformation, but also whether the crystal can transform before slip strength or fracture strength is reached.

7.4 Size Dependence of Shape Memory Effect

The size dependence of shape memory effect from bulk zirconia to microscale pillars has been discussed in Chapter 5, where grain boundaries play a significant role in

determining the shape memory behavior. Here we focus on the size dependence of transformation behavior for single crystal pillars at microscale.

To justify that, three groups of pillars with same composition ($2Y_2O_3$-$5TiO_2$-ZrO_2), three sets of crystal orientations and different dimensions were prepared and indented, and the stress-strain curves are shown in Figure 7.15(a), (b) and (c). The pillar diameters range from 0.8 μm to 2.5 μm, so as to ensure single crystal structure. All the pillars experienced one clean transformation plateau, with no clear steps observed. It is clear that the transformation is highly affected by the diameter of pillars, with larger diameter requiring higher stress to transform.

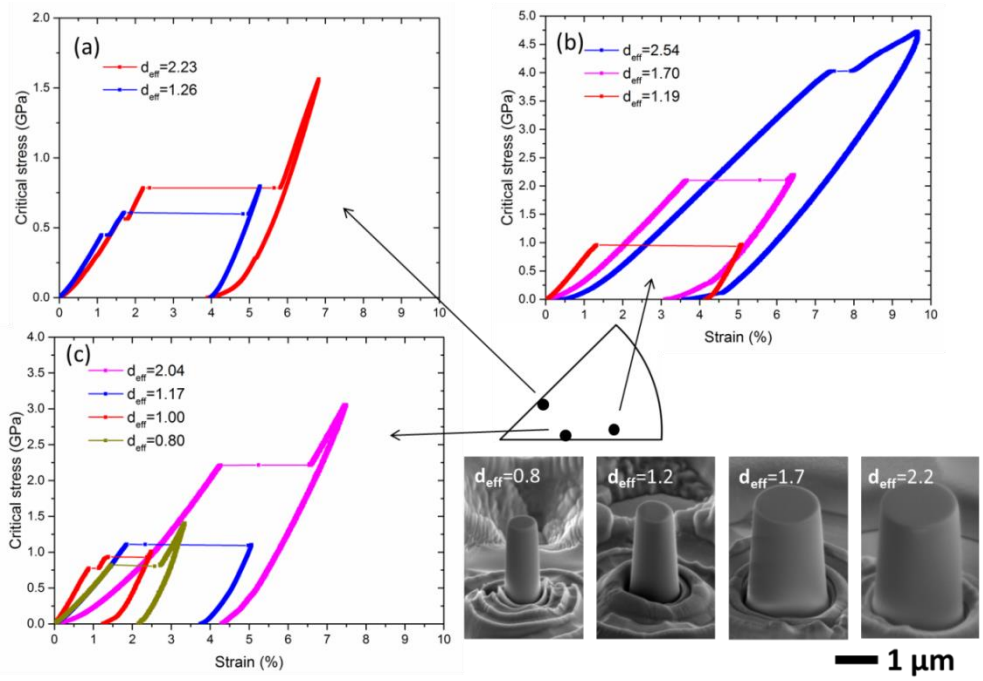

Figure 7.15 The stress-strain behaviours of pillars with diameters ranging from 0.8 μm to 2.5 μm and crystal orientations of (a) [258.8, 42.7, 334.4], (b) [266.4, 18.9, 198], (c) [257.9, 60.2, 147.4].

This observation agrees with the results reported in our earlier work[13], that transformation stress increases with pillar size for zirconia pillars without orientation control. However, this is of opposite trend to those in shape memory metals[14,15]. The difference in the trend is attributed to the elastic energy (ΔU_e) in Equation 15. The Young's modulus of zirconia (~ 200 GPa) is much higher as compared to Cu-Ni-Al shape memory alloy[16]. Chen and Schuh[14] showed that for Cu-Ni-Al shape memory alloys with Young's modulus of 26 GPa, the critical stress could increase by ~20 MPa as the pillar

diameter increased to a "bulk" response. With an order of magnitude higher modulus, it is reasonable to expect hundreds of MPa increase in transformation stress of zirconia ceramics at bulk size scales. This issue will require further study, but it does point to unique possible size effects in shape memory ceramics as a class.

According to Equation 15, the martensitic transformation behavior of single crystal material is directly related to the change of elastic strain energy ΔU_e, which can be expressed as[17]:

$$\Delta U_e = V \cdot SE$$

where V is the volume of the transformed monoclinic variant, SE is the strain energy per unit volume which is dependent on the shear modulus, Poisson's ratio, elastic constant, transformation strain and monoclinic variant shape[17]. Though it is rather complicated to determine the absolute value for SE, it can be considered as a constant for micro-pillars.

The size dependence of shape memory effect therefore can be explored by compressing pillars with same crystal orientation ($\cos\chi * \cos\lambda$), same composition ($\Delta S^{t\to m}$, T_o), but different size and Equation 16 can be rewritten as:

$$\sigma_{comp} = \frac{-\Delta S^{t\to m}(T_o - T) + V \cdot SE + \Delta U_s}{\cos\chi * \cos\lambda * \Delta\varepsilon} = B \cdot V + C \qquad \text{Equation 32}$$

where constant $B = \frac{SE}{\cos\chi * \cos\lambda * \Delta\varepsilon} = \frac{SE}{0.16} \cdot {SF_{max}}^{-1}$ and constant $C = \frac{-\Delta S^{t\to m}(T_o - T) + \Delta U_s}{\cos\chi * \cos\lambda * \Delta\varepsilon} = -(0.35 + \frac{\Delta U_s}{0.16}) \cdot {SF_{max}}^{-1}$.

Since SE is a positive constant, both the slope and intersect of Equation 32 is linearly controlled by ${SF_{max}}^{-1}$. Similar to what has been observed in section 7.3 for temperature effect, the crystal orientation map of stress (Figure 7.6) in section 7.2.2 can be used for the slope map and intersect map in the relationship between transformation stress and size.

By plotting the transformation stress with respect to pillar diameter, a clear linear relationship is observed, though the slope of the lines appears to be different for different crystal orientations, as shown in Figure 7.16. Pillars with a higher ${SF_{max}}^{-1}$ have a higher slope but lower intersect (red line), as compared to pillars with lower ${SF_{max}}^{-1}$. This observation complies nicely with Equation 32, that the slope should be positively related

to SF_{max}^{-1} whereas the intersect should be negatively related to SF_{max}^{-1}. A more detailed trend of the slope and intersect stress-size relationship should be referred to the orientation map in section 7.2.3, which is directly related to SF_{max}^{-1}.

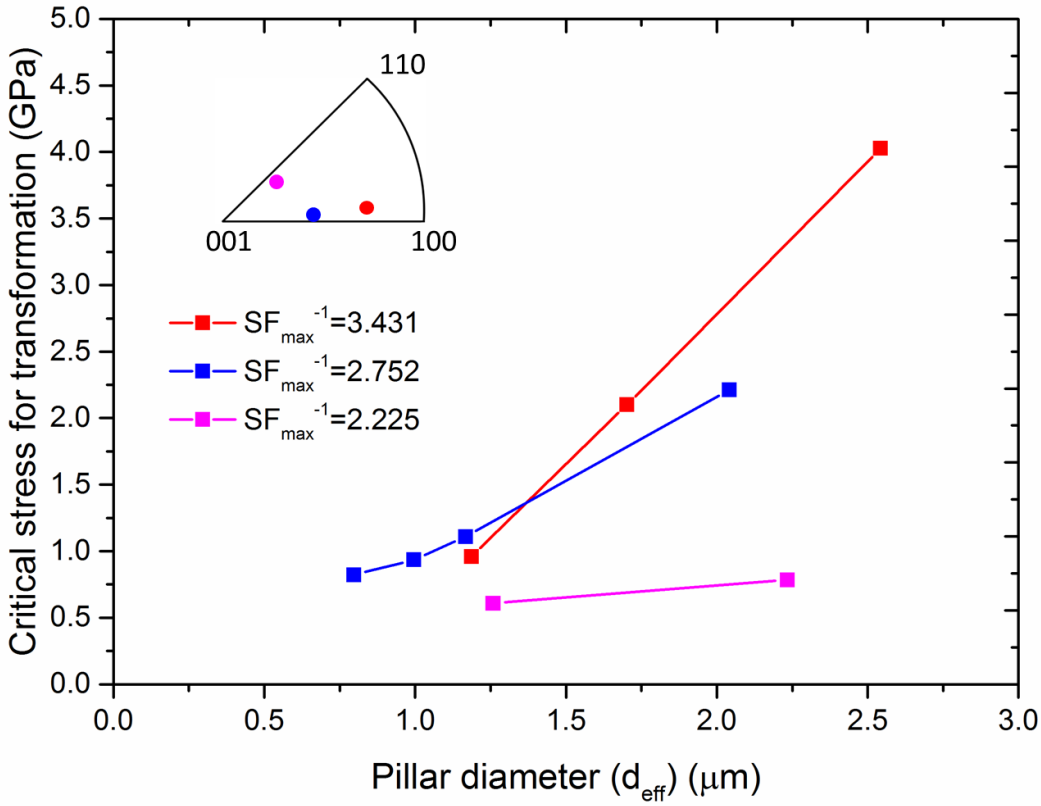

Figure 7.16 The critical transformation stress as a function of pillar diameter for pillars with three different crystal orientations.

It is to be noted that the surface energy (ΔU_s) in Equation 32 are known to be influenced by the interaction of martensite with sample surfaces, it seems possible that by extension surface energy might also affect by the size of pillar. We are not aware of significant discussion of this issue for shape memory ceramics, and clearly more work is needed in the future.

7.5 Composition Dependence of Shape Memory Effect

The change in ceramics composition will affect the martensitic transformation through the change of enthalpy $\Delta H^{t\rightarrow m}$. It has been discussed clearly in Chapter 4 that for

YTDZ ceramics, the tetragonal grains always have composition of $2Y_2O_3$-$5TiO_2$-ZrO_2, while the excess yttrium falls into cubic grains with composition of $5Y_2O_3$-$5TiO_2$-ZrO_2. As the cubic to tetragonal transformation does not involve significant shape strain, the deformation is not significant enough to cause shape memory effect, and therefore of less interest for this project. As the interest is on the composition dependence of shape memory effect for tetragonal pillars, we explored another zirconia system doped with ceria, for which a variety of ceria doping concentration can result in tetragonal pillars.

Zirconia with composition of $x$$CeO_2$-$0.5Y_2O_3$-$ZrO_2$ was prepared with x varying from 7.5mol% to 9.5mol%. Fives pillars with same dimensions, same crystal orientation but different composition were fabricated and tested at room temperature, to decouple the composition effect from other critical parameters according to Equation 15.

Figure 7.17 shows the load-displacement curves of the five pillars with (011) orientation. Most of the pillars have the load-displacement curves with the characteristic of martensitic transformation of large strain plateau. The transformation load tends to increase with doping concentration. It should be noted that when the Ce% is about 9.0 mol% or higher, it is hard to observe the strain plateau induced by martensitic transformation. When the load was further increased to 2000 μm or higher, the pillars tend to be broken. This indicates that the critical stress for martensitic transformation becomes higher than the fracture strength of the pillars. This phenomenon is not only observed in the (011) oriented pillars, but also for other oriented pillars which are not reported here.

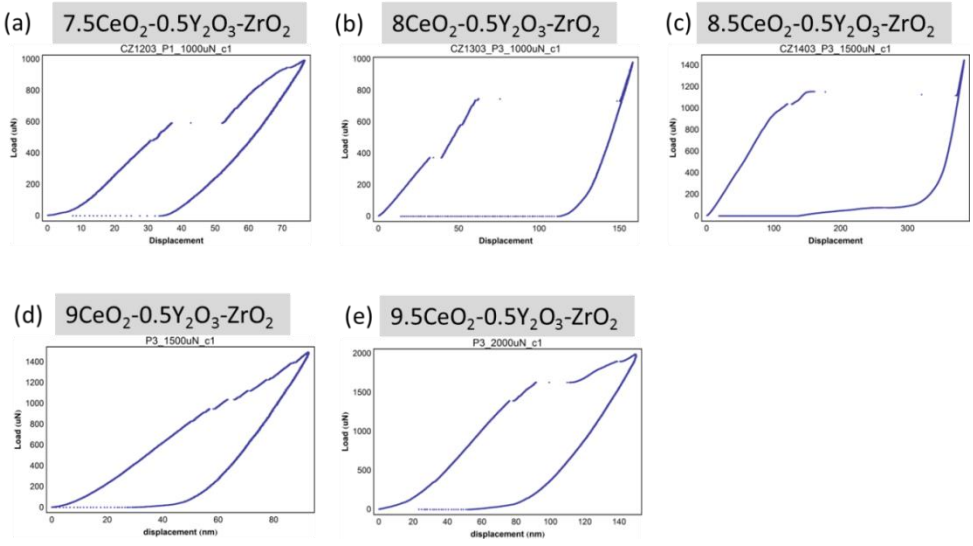

Figure 7.17 The load-displacement curves of (011) oriented pillars with different CeO_2%.

The calculated critical stress as a function of ceria concentration has been plotted in Figure 7.18. There is a clear trend that the critical stresses increases from 0.5 GPa to ~1.6 GPa with ceria concentration increasing from 7.5 mol% to ~9.0 mol%. This observation complies with the theory that higher energy is required for martensitic transformation when tetragonal zirconia is more stabilized by doping with more ceria.

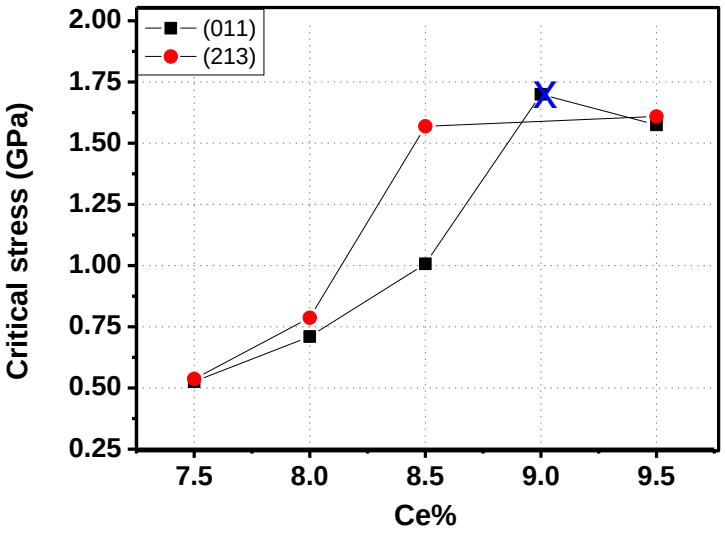

Figure 7.18 Critical stress of martensitic transformation for the CeO_2-Y_2O_3-ZrO_2 ceramics with different concentration of CeO_2. (*x*: indicate the pillar is broken)

7.6 Concluding Remarks

By controlling the pillar properties and testing environment, we have managed to decouple the parameters of crystal orientation, test temperature, ceramic composition and ceramic size, on the effect of shape memory behavior for zirconia-based ceramics. A systematically study was conducted to explore the effect of each parameter one by one, with the focus on the dependence of crystal orientation. A few conclusions can be down as follows:

(1) The shape memory effect of single crystal YTDZ pillars is highly dependent on the crystal orientation of pillar with respect to the compression axis.

(2) The Schmid factor is directly related to the martensitic transformation stresses. Pillars with orientations close to (110) and (101) planes are the easiest for transformation

with lowest stress required. Pillars with orientations close to (100) and (001) planes tend to fracture before reaching the theoretical transformation stress.

(3) The orientation map of stress not only predicts the orientation dependence of zirconia behavior, but indirectly indicates the sensitivity of zirconia to temperature and size.

(4) The transformation strain and Young's modulus of tetragonal pillars are both orientation dependent, though the dependence behavior is quite complicated.

(5) The martensitic transformation stress increases significantly with testing temperature, caution is required for high temperature applications so as not to exceed the fracture strength of around 3 GPa.

(6) The ceramic size at small scale could also affect the transformation behavior, while pillars with higher surface-to-volume ratio tend to transform at slightly lower stress.

(7) The composition could affect the transformation stress, but such effect is not obvious in YTDZ system. Higher doping concentration of stabilizer CeO_2 results in higher transformation stress.

The study of martensitic transformation suggests that the transformation behavior is dependent on the crystal orientation, test temperature, ceramic composition and ceramic dimensions, just as predicted by Equation 13. The crystal orientation and test temperature are found to be the two most critical parameters in determining the martensitic transformation stress.

Reference

[1] P. F. Becher & M. V. Swain. *J Am Ceram Soc.* **1992**, 75, 493-502.
[2] H. Horikawa, S. Ichinose, K. Morii, S. Miyazaki & K. Otsuka. *Metall Trans A.* **1988**, 19, 915-923.
[3] J. Chevalier, L. Gremillard, A. V. Virkar & D. R. Clarke. *J Am Ceram Soc.* **2009**, 92, 1901-1920.
[4] I. N. Sneddon. *Int. J. Engng Sci.* **1965**, 3, 47-57.
[5] H. Y. Fei, A. Abraham, N. Chawla & H. Q. Jiang. *J Appl Mech-T Asme.* **2012**, 79.
[6] J. F. Nye. Physical properties of crystals, their representation by tensors and matrices. (*Clarendon Press*, 1957).
[7] E. H. Kisi & C. J. Howard. *J Am Ceram Soc.* **1998**, 81, 1682-1684.
[8] X. S. Zhao, S. L. Shang, Z. K. Liu & J. Y. Shen. *J Nucl Mater.* **2011**, 415, 13-17.
[9] Z. Du, X. M. Zeng, C. Liu, C. A. Schuh & C. L. CGan. *Acta Mater.* **2017**, 123, 255-263.

[10] X. Y. Zhang, L. C. Brinson & Q. P. Sun. *Smart Mater Struct.* **2000**, 9, 571-581.
[11] F. Wakai & T. Nagono. *J Mater Sci Lett.* **1988**, 7, 607-609.
[12] T. G. Nieh, C. M. Mcnally & J. Wadsworth. *Scripta Metallurgica.* **1988**, 22, 1297-1300.
[13] Z. H. Du, X. M. Zeng, Q. Liu, A. Lai, S. Amini, A. Miserez, C. A. Schuh & C. L. Gan. *Scripta Mater.* **2015**, 101, 40-43.
[14] Y. Chen & C. A. Schuh. *Acta Mater.* **2011**, 59, 537-553.
[15] B. G. Clark, D. S. Gianola, O. Kraft & C. P. Frick. *Adv Eng Mater.* **2010**, 12, 808-815.
[16] P. Sedlak, H. Seiner, M. Landa, V. Novak, P. Sittner & L. Manosa. *Acta Mater.* **2005**, 53, 3643-3661.
[17] P. M. Kelly & L. R. F. Rose. *Prog Mater Sci.* **2002**, 47, 463-557.

Chapter 8

Impact & Future Work

This chapter discusses the implication of the research on small volume shape memory ceramics. It draws together the threads of the thesis work by proving the hypothesis of size effect and crystal structure effect. It also includes some reconnaissance studies of material selection for shape memory ceramics. The future work regarding the exploration of superelasticity in YTDZ ceramics and shape memory effect in particles are discussed.

8.1 Summary and Implications

In summary, the work presented in this thesis has demonstrated that microscale yttria stabilized zirconia (YSZ) is a very promising shape memory ceramic material. Compared to bulk ceramics, remarkable property enhancement has been achieved in terms of substantially larger recoverable strain at high transformation stress as a result of martensitic transformation. The YSZ pillars deform at a critical stress much higher than shape memory alloys, enabling much larger damping capacity for potential applications.

Through the thoughtful study of the bulk ceramics presented in Chapter 4, we developed a deep scientific understanding of the dopant material and its concentration that have a deterministic effect on the morphology, phase composition and grain size distribution of the ceramics. Zirconia ceramics can be stabilized into tetragonal phase at room temperature by yttria, while the grain size can be significantly increased by introducing grain promoter titania. It is shown that yttrium atoms are not uniformly distributed in bulk zirconia ceramics and there is a significant elemental partition in the areas consisting of tetragonal phase and cubic phase. The elemental segregation urges the study of localized phase and composition at grain-scale of the yttria-titania doped zirconia (YTDZ) .The methodology discussed in Chapter 3 enables fabrication of polycrystal YSZ pillars and single crystal YTDZ pillars.

The shape memory effect with large transformation stress and strain has been discovered for both YSZ and YTDZ pillars. However, the reliability of shape memory effect of single crystal YTDZ pillars is much better than that of YSZ pillars. The large deformation was found to be directly induced by the reversible martensitic transformation.

The effect of crystal orientation on the shape memory effect of YTDZ pillars has been investigated, together with the effect of testing temperatures, ceramic compositions and ceramic dimensions. A critical assessment of shape memory properties has been conducted in terms of Young’s modulus, critical stress and transformation strain. The property maps have been constructed to provide guidance for applications. In addition, the test temperature, ceramic composition and dimension were all found to affect the transformation stress of shape memory YTDZ pillars.

8.1.1 Proven of hypothesis

With the aim to develop robust shape memory zirconia ceramics that is conventionally brittle, the thesis includes the understanding and proof of two hypothesizes. The first step is to increase the fracture strength of the ceramics, so that the stress-induced martensitic transformation, which is the underlying mechanism for shape memory effect, can occur before fracture. Based on literature work, the first hypothesis is proposed to be: *by making the ceramics at small volume, the stress they can sustain is high enough that martensitic transformation could occur without experiencing crack.* This hypothesis is evaluated by studying the conventional brittle YSZ ceramics at small volume. The results of mechanical tests show that at small scale, YSZ ceramics can undergo martensitic transformation without producing cracks, suggesting that the fracture strength is higher than transformation stress. These studies prove that the size effect is critical for the fracture strength of YSZ ceramics and thus the first hypothesis is successfully demonstrated by experiments. They lay the foundation for further exploration of shape memory effect in small volume zirconia.

However, the occurrence of martensitic transformation in YSZ ceramics does not guarantee its shape memory effect. The grain boundaries and the resultant crystal mismatch in the small volume YSZ ceramics introduce uncertainty to the mechanical behaviors, prohibiting repeatable and reliable stress-induced martensitic transformation. In the attempt to address the problems caused by grain boundaries, we explored a few dopant candidates that can increase the grain size to fabricate single crystal ceramics at small volume. This work is motivated by the second hypothesis: *By developing single crystal YTDZ pillars at microscale, we can achieve robust shape memory ceramics with reliable shape memory effect that is tunable by crystal orientation, ceramic dimensions, ceramic compositions and testing temperatures.* In the exploration of dopant candidates, titania was found to be the most suitable dopant in YSZ ceramics, as it can significantly increase the grain size without altering other properties of the ceramics. The modified YTDZ ceramics (with two dopants of yttria and titania in zirconia) are more complicated systems as compared to YSZ ceramics. Therefore, a systematic study was carried out to investigate the effect of both dopants and their relationship with each other. It was found

that zirconia with 2mol% yttria and 5 mol% titania has the desired tetragonal phase with sufficiently large grain size for the fabrication of single crystal ceramics. The relationship between material composition and crystal phase are of critical importance to determine the suitable composition for zirconia to function as shape memory materials.

In addition to the properties at room temperature, the YTDZ ceramics were studied at higher temperatures for its martensitic transformation. By correlating the martensitic transformation temperatures with the testing temperature, we are able to establish the transformation temperature-composition relationship for YTDZ systems. Such relationship could predict the behavior of zirconia at different temperatures and guide the selection of suitable compositions for various application temperatures. The small volume single crystal ceramics were fabricated and mechanically compressed to study the stress-induced martensitic transformations. It was found that the ceramics could sustain significant deformation without cracking, and such deformation could be recovered through inverse martensitic transformation. These results show that the single crystal YTDZ ceramics could successfully exhibit shape memory effect, supporting the second hypothesis.

8.1.2 Scientific significance

The single crystal ceramics allow the decoupling of different controlling parameters that determine the shape memory effect of YTDZ and aids us to explore the underling mechanism one by one. We have established a scientific understanding of the key parameters for shape memory YTDZ materials, including crystal orientation, material composition, ceramics size and testing temperature.

Firstly, a detailed study was conducted to investigate the crystal orientation dependence of YTDZ ceramics on the shape memory effect. It was discovered that there is a significant orientation dependence in terms of Young's modulus of tetragonal zirconia, critical stress, transformation strain and energy dissipation. The magnitude of Young's modulus of tetragonal zirconia varies with orientation from 50 GPa to 250 GPa. The highly tunable stiffness means that the single crystal YTDZ could be as soft as many metals or as rigid as many ceramics, depending on the orientation of mechanical

deformation. Both the magnitude of critical transformation stress and recoverable strain vary significantly with crystal orientation, covering stress of 0.6 ~ 4 GPa and strain of 1.5% ~ 6.5%. As long as the ceramic transforms, the energy damping capacity is much higher than that of shape memory alloys. The extremely high tunability of shape memory properties makes the ceramics widely open for various applications with different desired properties. It was also discovered that the ceramics could be completely brittle like traditional ceramics in some orientations, but in such cases, the fracture stress could go up to 8 GPa and be much higher than traditional bulk ceramics. Therefore, the study of orientation dependence of shape memory properties is of critical significance for knowing the material performance in practical applications.

In terms of ceramic composition dependence of shape memory properties, we discovered that higher doping concentration generally makes it harder to transform, leading to higher critical transformation stress. It was also found that a change in testing temperature may not only affect the characteristic shape memory properties, but also results in completely different behavior of fracture without transformation. The ceramic composition and test temperature are two correlated parameters that both change the chemical energy of the ceramics. Shape memory behavior can only be obtained at a suitable combination of ceramic composition and test temperature. Therefore, for future applications, the suitable composition for shape memory properties has to be designed with the intended working temperature.

8.2 Future Work

As we have established the structure-property relationship for shape memory effect in YTDZ ceramics, such relationship could be extended towards another important property of shape memory ceramics, superelasticity. Similar approaches can be employed in the future to explore the superelasticity in single crystal YTDZ ceramics, so as to develop compositions suitable for repeatable energy dissipation. In addition to the single crystal pillars, other structural forms of SMCs such as particles could demonstrate similar shape memory effect and are more suitable for large quantity fabrications for potential

applications. The fabrication and mechanical properties of single crystal powders with YTDZ ceramics could be explored in the future.

8.2.1 Superelasticity in YTDZ ceramics

According to the thermodynamics of martensitic transformation, materials that demonstrate shape memory effect at a low temperature may become superelastic (pseudoelastic) at higher temperature,[1] as shown in Figure 8.1. Superelasticity is different from shape memory effect in that the SMCs are able to automatically recover the shape after unloading without the need for heat treatment. The superelasticity can be achieved by conducting high temperature testing or adjusting the stabilizer concentration[2].

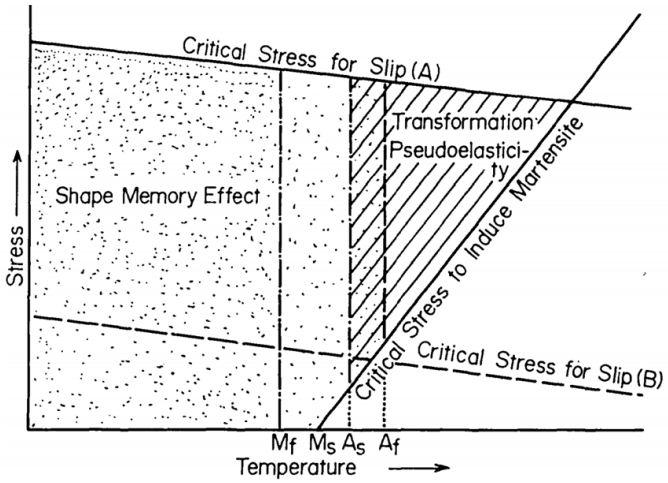

Figure 8.1 Schematic diagram representing regions of shape memory effect and transformation pseudoelasticity in temperature-stress coordinates; (A) represents critical stress for slip for a case of high critical stress and (B) represents critical stress for slip for a case of low critical stress.[1]

During our studies on shape memory effect of YTDZ ceramics, we observed a few pillars demonstrating superelasticity. Figure 8.2(a) illustrates the load-displacement behavior of a pillar with compostion of $4Y_2O_3$-$5TiO_2$-ZrO_2. The pillar exhibited excellent superelastic behavior. After 125 cycles of compression at 200 μN and load releasing, it still survived without fracture. From the representative load-displacement curves in Figure 8.2(a), it is clear that the curves look relatively similar to each other, meaning that the transformation behavior is highly repeatable. The critical load for martensitic transformation is in the range of 120-180 μN and the maximum displacement ranges

from 250 nm to 370 nm. The FESEM images confirmed that the pillar survived 125 compression cycles without failure, as shown in Figure 8.2(b). This result suggests that both shape memory effect and superelasticity are possible in YTDZ ceramics.

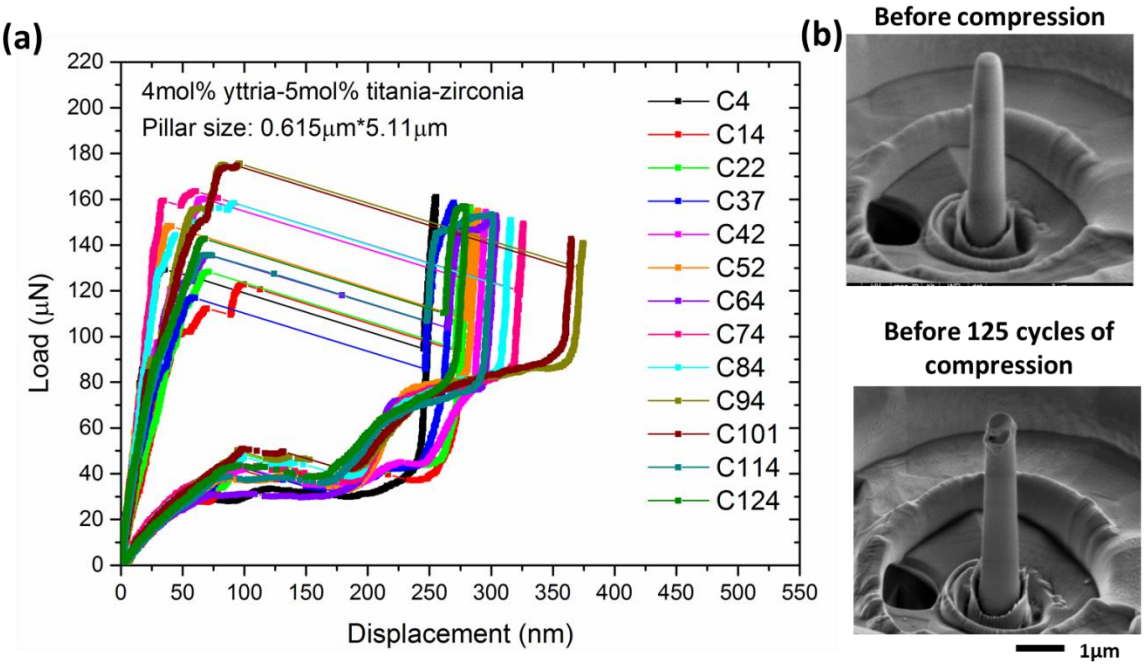

Figure 8.2 The representative load-displacement curves of a pillar that went through 125 loading/unloading cycles at 200μN.

Therefore, one direction for future work can be to explore the superelasticity of YTDZ pillars by slightly adjusting the current fabrication protocol. The superelasticity allows cyclic test, which enables repeat use of shape memory ceramics for various applications.

8.2.2 Shape memory ceramics in particles

The systematic assessment of the controlling parameters of shape memory effect in YTDZ pillars provides the foundation for various applications. However, the small volume pillars are not suitable for fabrication in large quantity. As it has been suggested that the exact shape of ceramics is not a critical factor for good shape memory behavior in YTDZ system, one direction for future work is to explore single crystal ceramics with alternative shapes suitable for large quantity fabrication.

Hydrothermal method is an easy and fast approach to develop single crystal ceramics at low temperature. It involves nucleation and crystallization of particles in aqueous solution at high temperature and vapor pressure. The high pressure reduces the crystallization temperature of zirconia from >1000^{o}C to ~200^{o}C, enabling direct production of crystalline particles without any high temperature sintering process.[3] It is an ideal technique to synthesize large quantity of single crystal ceramics with high purity, controlled stoichiometry, narrow particle size distribution, controlled morphology and high crystallinity. Figure 8.3 presents some preliminary results of YTDZ powders with hydrothermal method. It can be seen that a large quantity of nanoscale particles with rice shape can be obtained. Such observation suggests that mechanical test can be conducted on these particles and their shape memory effect at macroscale can be further explored.

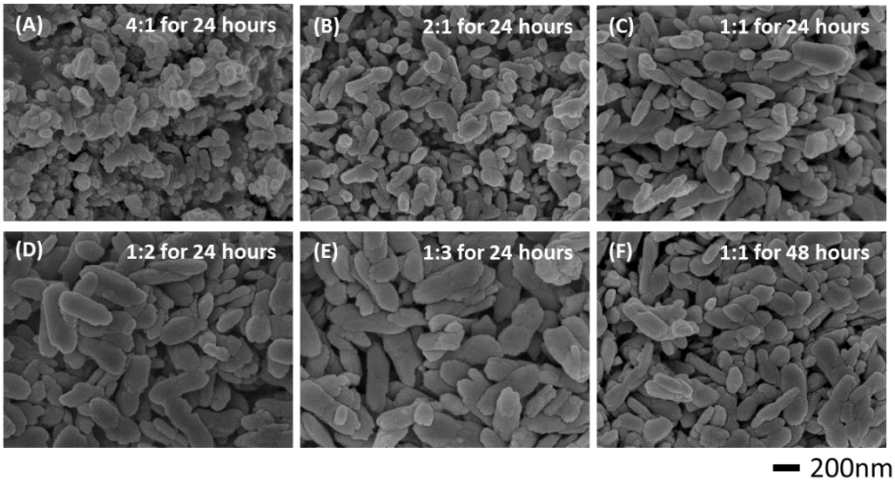

Figure 8.3 FESEM images of zirconia particles prepared by hydrothermal method using the molar ratio of $ZrO(NO_3)_2.xH_2O$ / NaOH of (A) 4:1 for 24 hours, (B) 2:1 for 24 hours, (C) 1:1 for 24 hours, (D) 1:2 for 24 hours, (E) 1:3 for 24 hours, (F) 1:1 for 48 hours.

8.2.3 Shape memory ceramics in other structures

As study of single crystal zirconia at small volume has proven that surface area-to-volume ratio is critical, we can also explore shape memory zirconia in other structures having high surface area-to-volume ratio like foams, thin films and fibers. According to the well-developed processing methods for these structures, as reviewed in section 2.4, it is very promising to develop shape memory ceramics as foams, thin films and fibers.

Together with the outstanding properties of zirconia with high resistance to corrosion and excellent biocompatibility, shape memory zirconia in these structures are highly potential to work in medical application, as actuators or as energy damping materials.

Reference

[1] K. O. a. K.Shimizu. *International Metals Reviews.* **1986**, 31, 93-114.
[2] Z. G. Wei, R. Sandstrom & S. Miyazaki. *J Mater Sci.* **1998**, 33, 3743-3762.
[3] T. Tsukada, S. Venigalla, A. A. Morrone & J. H. Adair. *J Am Ceram Soc.* **1999**, 82, 1169-1174.

Chapter 9
Appendix

9.1 Reconnaissance Studies - Effect of Magnesia on YSZ Ceramics

On the exploration of suitable dopant to develop coarse grained YSZ ceramics, magnesia was studied as one of the candidates besides titania. It was discovered that by doping a small amount of magnesia into the $3Y_2O_3$-ZrO_2 ceramics, the grain size could be significant increased, as shown in Figure 9.1. 0.5mol% of magnenia could increase the grains to a size comparable to the effect of 5 mol% of titania. However, as shown in the FESEM images, a lot of pores are observed on the surface and some micro cracks along are found along the grain boundaries, suggesting that magnesia evaporation could have happened during the sintering process, lowing the toughness of the ceramics.

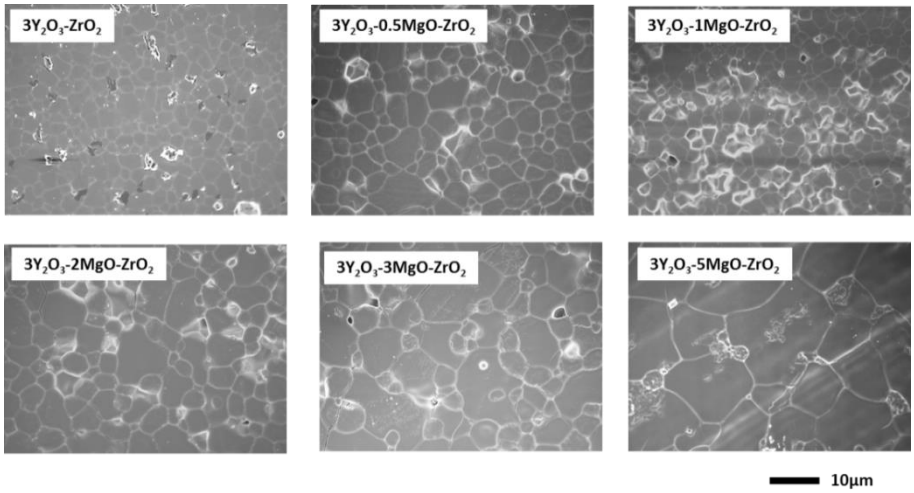

Figure 9.1 The FESEM images of zirconia with 3 mol% yttria and various amount magnesia.

Besides the microstructure, the phase composition is critical for the shape memory ceramics and XRD was conducted on the ceramics doped with magnesia, as shown in Figure 9.2. It was found that the introduction of magnesia has a significant effect on the phase composition of the ceramics. For $3Y_2O_3$-ZrO_2 ceramics, 100% of desired tetragonal phase was achieved, while for ceramics with 0.5 mol% magnesia, significant amount of monoclinic phase was discovered. With more magnesia introduced, the monoclinic phase disappeared and the ceramics was composed of 100% cubic at 5 mol%

of magnesia. The results suggest that magnesia prompt the formation of monoclinic and cubic phase instead of the tetragonal phases, making the system not suitable for shape memory effect.

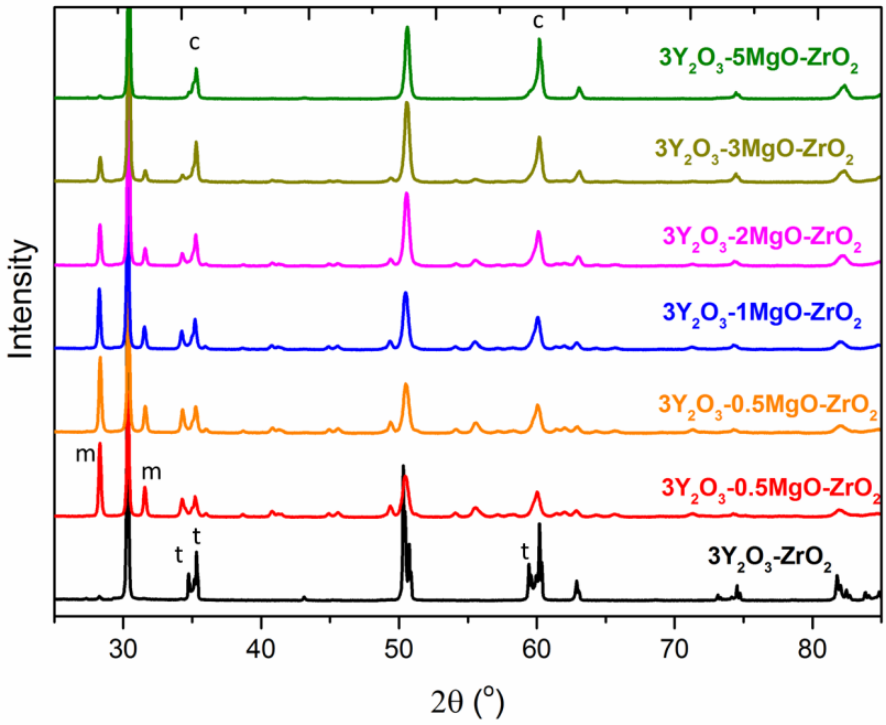

Figure 9.2 The XRD patterns of zirconia with 3 mol% yttria and various amount of magnesia.

9.2 Publication List

- Xiao Mei Zeng, Alan Lai, Zehui Du, Christopher A Schuh, Chee Lip Gan, Crystal orientation dependence of stress-induced martensitic transformation in shape memory zirconia. Acta Materialia, 116,124-135, 2016
- Xiao Mei Zeng, Zehui Du, Christopher A Schuh, Nobumichi Tamura, Chee Lip Gan, Microstructure, Crystallization and Shape Memory Behaviour of Titania and Yttria doped Zirconia. Journal of European Ceramic Society, 36, I5, 1277–1283, 2016
- Zehui Du, Xiao Mei Zeng, Qing Liu, Christopher A Schuh, Chee Lip Gan, Superelasticity in micro-scale shape memory ceramic particles, Acta Materialia, 123, 255-263, 2017

- Zehui Du, Xiao Mei Zeng, Qing Liu, Alan Lai, Shahrouz Amini, Ali Miserez, Christopher A. Schuh, and Chee Lip Gan, Size effects and shape memory properties in ZrO_2 ceramic micro- and nano-pillars. Scripta Materialia 101, 40–43, 2015
- Xiaomei Zeng, Xiaofeng Xu, Prathamesh M Shenai, Eugene Kovalev, Charles Baudot, Nripan Mathews, and Yang Zhao, Characteristics of the Electrical Percolation in Carbon Nanotubes/polymer Nanocomposites, Journal of Physical Chemistry C 115, 21685 (2011)
- Oral Presentation with title "Investigation of intragrain martensitic transformation in yttria stabilized zirconia ceramics by synchrotron X-ray micro-diffraction" at conference "Materials Science & Technology 2015" in October 2015
- Oral Presentation with title "Direct observation of shape memory effect in zirconia ceramics by in-situ nanoindentation" at conference "2014 MRS Fall Meeting " organized by Materials Research Society in December 2014
- Poster presentation with title "Superelasticity in Small Volume Yttria Stabilized Zirconia" at conference "International Conference on Materials for Advanced Technologies" organized by The Materials Research Society Singapore in July 2013
- Oral Presentation with title "Colorimetric detection of ultratrace cholesterol by free standing inverse opal hydrogel films" at conference "Image and Applied Optics" organized by Optical Society of America in June 2012
- Oral Presentation with title "Colorimetric detection of ultratrace cholesterol by free standing photonic hydrogel films" at conference "International Conference of Young Researchers on Advanced materials" organized by Materials Research Society of Singapore in July 2012